



UNIVERSITÀ
DEGLI STUDI
DELL'AQUILA

Dipartimento di Scienze Fisiche e Chimiche
Dottorato di Ricerca in Scienze Fisiche e Chimiche

Ph.D. Thesis

**Search for upward-going showers with
the Fluorescence Detector of the Pierre
Auger Observatory**

Supervisor:
Prof. Francesco Salamida

Ph.D. candidate:
Massimo Mastrodicasa

XXXIII Cycle - A. Y. 2017/2021

Abstract

Upward-going air showers are a possible interpretation of the recent events reported by the ANITA Collaboration, but the energies and the elevation angles of these events appear to be in tension with the predictions of the standard model of particle physics. Given its operation time and wide field of view, the Fluorescence Detector (FD) of the Pierre Auger Observatory is sufficiently sensitive to upward-going showers when used in monocular mode and thus can be exploited to test this interpretation. For this reason, the Pierre Auger Collaboration has performed a generic search for upward-going showers with the FD. The sensitivity of the FD to upward-going showers has been studied with dedicated simulations of upward-going events. To set up these simulations from a geometrical point of view, a Monte Carlo simulation for upward-going showers based on simple assumptions has been preliminarily developed. The background for this search, which consists of downward-going showers with specific geometric configurations erroneously reconstructed as upward-going events in a monocular reconstruction, has been estimated with extensive simulations. Also laser shots, which are continuously fired to monitor the quality of the atmosphere and are genuine upward-going events, can produce background when they are not properly labelled. In order to reject laser events, a set of cuts has been developed by using a sample of 10% of the available FD data from 14 years of operation. Furthermore, a set of quality selection criteria has been defined to reduce the mis-identification of downward-going and upward-going events. After having set all the selection criteria, the detection efficiency of the FD to upward-going showers has been studied and the exposure has been calculated. A number of candidate events consistent with the number of events expected from background has been found after the unblinding of the full data set. An upper limit on the flux of upward-going showers has been then derived. To make the results of this analysis suitable to be applied to different physical scenarios, differential tables of exposure have been finally provided.

*Utsukushi ya
Shōji no ana no
Ama-no-gawa.*

*How beautiful,
Through a hole
[in the paper door,
The Milky Way.*

—Kobayashi Issa

Contents

Introduction	1
1 The cosmic rays	3
1.1 The discovery of the cosmic rays	3
1.2 The energy spectrum of the cosmic rays	4
1.3 Acceleration, sources and propagation of the cosmic rays	7
1.3.1 The Fermi acceleration	7
1.3.2 The diffusive shock acceleration	9
1.3.3 The sources of the cosmic rays	11
1.3.4 The propagation of the cosmic rays and the GZK cutoff	12
1.4 Interaction of the cosmic rays with the atmosphere	16
1.4.1 Electromagnetic showers	17
1.4.2 Hadronic showers	18
2 The Pierre Auger Observatory	23
2.1 The surface detector	23
2.1.1 The electronics of the SD	25
2.1.2 The calibration of the SD	25
2.1.3 The local trigger of the SD	27
2.1.4 The SD event reconstruction	27
2.2 The fluorescence detector	30
2.2.1 The electronics of the FD	31
2.2.2 The trigger of the FD	32
2.2.3 The calibration of the FD	32
2.2.4 The FD event reconstruction	34
2.2.5 The atmospheric monitoring	37
2.3 The enhancements to the Pierre Auger Observatory	39
2.3.1 HEAT	39
2.3.2 AMIGA	40
2.3.3 AERA	41
2.4 The upgrade of the Pierre Auger Observatory	42

3	Multi-Messenger astrophysics with the Pierre Auger Observatory	45
3.1	Searches for different types of cosmic messengers	45
3.1.1	Search for diffuse photons	46
3.1.2	Search for photons from point-like sources	50
3.1.3	Photon follow-up of gravitational wave events with the SD	52
3.1.4	Search for diffuse neutrinos with the SD	53
3.1.5	Search for neutrinos from point-like sources with the SD	59
3.1.6	Neutrino follow-up of gravitational wave events with the SD	62
3.1.7	Search for neutrons with the SD	64
3.2	The puzzle of the ANITA anomalous events	65
3.2.1	The ANITA experiment	65
3.2.2	The ANITA anomalous events	67
3.3	Search for ANITA-like events with the FD	69
4	A Fast Monte Carlo simulation for upward-going showers	71
4.1	Simulation of proton induced upward-going showers	71
4.1.1	Parameterization of the X_{\max} distributions	72
4.1.2	A tool for the X_{\max} distributions	74
4.2	Geometric features of the simulation	76
4.3	Trigger conditions	77
4.4	Study of the detection efficiency	79
4.4.1	Dependence on the position of the exit point	79
4.4.2	Dependence on the injection height	80
4.4.3	Dependence on the primary energy and zenith angle	82
4.5	Exposure to upward-going showers	84
4.5.1	Exposure calculation	84
4.5.2	A first estimate of the exposure	85
5	Search for upward-going showers with the FD	89
5.1	Signal simulation	89
5.1.1	Detection efficiency and exposure without selection cuts	92
5.2	Background simulation	94
5.3	The Profile Constrained Geometry Fit reconstruction	96
5.4	Data cleaning and event selection criteria	98
5.4.1	Pre-selection criteria applied on the monocular reconstruction	99
5.4.2	Selection criteria applied on the PCGFup reconstruction	100
5.5	Discrimination between signal events and background events	101
5.6	Detection efficiency and exposure with selection cuts	105
5.7	Unblinding of the data and differential exposure	107
	Conclusions	111

Appendices	113
A Measurement of the linearity of two Hamamatsu R9420 PMTs	113
A.1 The experimental setup	113
A.2 Non-linearity measurements	113
B Hadronic interaction models used in air shower simulations	119
B.1 High energy hadronic interaction models	119
B.2 Low energy hadronic interaction models	122
List of Abbreviations	123
List of Figures	125
List of Tables	137
Bibliography	139
Acknowledgements	153

Introduction

Since cosmic rays were discovered, many steps have been made towards the comprehension of their properties. Piece by piece, cosmic ray experiments have contributed to the unveiling of their mysteries, but their puzzle is still far from complete. One of the most challenging questions about cosmic rays concerns their origin and composition. Answering this question is even harder for cosmic rays at energies above $\sim 10^{18}$ eV, the so-called Ultra High Energy Cosmic Rays (UHECRs), whose flux is too low to allow for their direct detection in space. UHECRs can be detected only by measuring the secondary particles produced by their interaction with the atmosphere, the so-called Extensive Air Showers (EAS). For this reason, the detection of UHECRs requires ground-based experiments covering large areas. In this respect, the Pierre Auger Observatory is the largest cosmic ray observatory of the world. It is located in Malargüe, Argentina and combines an array of 1660 water Cherenkov stations covering an area of about 3000 km² and 24 fluorescence telescopes overlooking the same area. The surface detectors allow to measure the Cherenkov light produced in water by the secondary particles of the air shower at ground level, while the fluorescence telescopes allow to measure the light emitted by the nitrogen molecules excited by the particles of the air shower on clear moonless nights. Many results have been achieved by the Pierre Auger Observatory since it became operative in 2004, such as the measurement of the UHECR energy spectrum, which provides evidence of a flux suppression at the highest energies, the studies on the mass composition and the distribution of the arrival directions. To further shed some light on the mass composition of the UHECRs and the origin of the flux suppression, the Pierre Auger Observatory has started a major upgrade, whose main component consists of surface scintillator detectors. These detectors allow for a better discrimination between the electromagnetic and muonic component of the air shower.

When the first gravitational wave was detected, it became clear that the information from different cosmic messengers such as cosmic rays, neutrinos, gamma rays, gravitational waves and neutrons could be used together to study the corresponding astrophysical sources. Since the Pierre Auger Observatory is sensitive also to neutral particles, it took part to the combined Multi-Messenger searches that were coupled to the later detection of gravitational waves. Furthermore, Multi-Messenger searches for neutrinos, photons and neutrons have been performed and are currently on-going within the Pierre Auger Collaboration. Important limits on the flux of these particles have been set, leading, together with the results obtained for cosmic rays, to a better

comprehension of our Universe.

Sometimes, the detection of anomalous events poses new challenges and questions, especially when these events appear to be in tension with well established results. Such events represent a unique opportunity to test the current models and provide some insight into new phenomena. This is the case of the recent events reported by the ANITA Collaboration, which are consistent with the interpretation of upward-going showers. These events have been detected at energies and elevation angles that appear to be in tension with the predictions of the standard model of particle physics, therefore, if confirmed, they would require significant modifications to this theory or new phenomena. A possible explanation of these events within the standard model of particle physics would be a transient neutrino flux from a point source. This hypothesis has been tested by the IceCube collaboration, but no evidence of such a flux has been found in any of its analyses. To confirm or constrain the interpretation of the ANITA events as upward-going showers and thus add some pieces to this puzzle, the Pierre Auger Collaboration has performed a generic search for ANITA-like events. These events are not expected to produce signals in the surface detectors because of their elevation angles, but they can be detected with the fluorescence telescopes, which are sufficiently sensitive to them.

My work, described in this thesis, has been mainly focused on the search of such upward-going showers with the fluorescence telescopes of the Pierre Auger Observatory and has been conducted within the Multi-Messenger task of the Auger Collaboration. A relevant part of my thesis work concerned the setting up of a Monte Carlo simulation reproducing the exact hardware configuration of the data taking of the Pierre Auger Observatory during a period of about 14 years. This simulation, hereinafter referred to as “Real Monte Carlo simulation”, is needed to estimate the exposure of the Pierre Auger Observatory to upward-going showers. To study the detectability of upward-going showers from a geometrical point of view and define an effective area for the generation of the events of the Real Monte Carlo simulation, I preliminarily developed a Monte Carlo simulation for upward-going showers based on simple geometrical and physical assumptions. Moreover, I contributed to the simulation of background events and the definition of the selection criteria used in this analysis. Also the derivation of the upper limits was part of my work. While the analysis is almost complete, the comparison of the results with those from the ANITA experiment is still underway within the Pierre Auger Collaboration.

This thesis will be organized in five chapters. Chapter 1 will deal with a general overview of the cosmic ray physics. In Chapter 2, the Pierre Auger Observatory will be described. Chapter 3 will focus on the Multi-Messenger searches carried out within the Pierre Auger Collaboration. The ANITA experiment and the properties of the ANITA anomalous events will be also described. Chapter 4 will deal with the description of the so-called “Fast Monte Carlo simulation” that has been used to guide the Real one. Finally, the details and the results I obtained for the generic search of upward-going showers with the fluorescence telescopes of the Pierre Auger Observatory will be presented in Chapter 5.

Chapter 1

The cosmic rays

The cosmic rays are elementary particles and nuclei that hit the Earth's atmosphere from space. When reaching the Earth, they are classified as "primary" if they have not yet interacted in the atmosphere or "secondary" if they have been produced in the interactions of primary cosmic rays with the atmosphere. Primary cosmic rays can be detected directly with space or balloon experiments at energies where their flux is high enough, while at the highest energies, where their flux is much smaller, the arrival direction, energy and composition of the primary cosmic rays can be measured by using the cascades of secondary particles produced by their interaction with the atmosphere. Cosmic rays can originate both inside and outside our own galaxy, the Milky Way, but their origin and composition still remain uncertain, especially for the ones at the highest energies.

1.1 The discovery of the cosmic rays

The discovery of the cosmic rays at the beginning of the 20th century allowed to solve some problems that had arisen during the 19th century. In the late 19th century it was known that a charged electroscope spontaneously discharged because of the ionization of the atmosphere, but the motivation for such ionization was not known. At the beginning of the 20th century the discovery of the spontaneous radioactivity seemed to provide a possible explanation for this behaviour because it was observed that an electroscope rapidly discharged in the presence of a radioactive material. The discharge was interpreted as due to the emission of charged particles from the radioactive material that caused the formation of ions in the air. The spontaneous discharge of the electroscope was thus attributed to the radioactivity of the Earth's crust. If this hypothesis was true the electroscope discharge rate should have decreased if measured far from the ground. To test this hypothesis, in 1909 Father Theodor Wulf, a Jesuit priest and a scientist, measured the electroscope discharge rate at the top of the Eiffel tower (about 300 m above the sea level), but he observed a decrease that was too small to confirm the hypothesis. Despite of this surprising result, he still attributed the electroscope discharge to the emission of charged particles from the ground.

The question was finally solved in 1912 by the Italian physicist Domenico Pacini and the Austrian physicist Victor Hess, that measured respectively the discharge rate of the electroscope underwater and at high altitudes. Pacini observed a decrease of the discharge rate with the depth in the water [1], while Hess measured an increase of the discharge rate with the altitude [2]. These results led to the conclusion that the discharge of the electroscope was caused by extraterrestrial radiation.

In 1926 Robert A. Millikan called that radiation “cosmic rays” because he believed that it was made by high energy γ rays [3]. Although during the following years several experiments proved that they were mainly composed by particles with a positive charge, the expression “cosmic rays” survived and is still used in the present day.

1.2 The energy spectrum of the cosmic rays

The energy spectrum of the cosmic rays covers a wide range of energies. Below $E \sim 10^9$ eV the flux is very high and is modulated by the solar wind, the plasma that emanates from the Sun, while above $E \sim 10^9$ eV it has a regular shape and follows a power law that shows two main break points (see Figure 1.1). The differential flux as a function of energy can be expressed as:

$$\frac{dN}{dE} \propto E^{-\gamma}, \quad (1.1)$$

where γ is the spectral index, that is considered to be related to the origin, acceleration mechanism and propagation of the cosmic rays.

At $E \sim 5 \cdot 10^{15}$ eV the spectral index changes from $\gamma \sim 2.7$ to $\gamma \sim 3.1$. This first break point is called “knee” and is considered to mark the beginning of the transition from the cosmic rays that have a galactic origin to the ones that are produced outside our galaxy. The second break point is called “ankle” and is observed at $E \sim 5 \cdot 10^{18}$ eV. At this energy the spectral index drops to $\gamma \sim 2.5$. Between the knee and the ankle the transition from galactic to extragalactic cosmic rays is supposed to take place. Above the ankle, the cosmic rays are believed to be mostly of extragalactic origin.

In order to emphasize the features of the cosmic ray energy spectrum the flux is usually multiplied by a power of the energy. The flux multiplied by $E^{2.6}$ as a function of the energy is shown in Figure 1.2. A further change in the spectral index between the knee and the ankle is clearly visible at $E \sim 4 \cdot 10^{17}$ eV. This additional break point is called “second knee”. Furthermore, the flux is suppressed above $E \sim 4 \cdot 10^{19.5}$ eV.

Above the knee, experimental evidences suggest that the composition of the cosmic rays changes from light nuclei to heavier ones, up to the second knee where the energy spectrum steepens to $\gamma \sim 3.3$. Above the second knee, the cosmic ray composition still remains uncertain.

The Pierre Auger Collaboration has recently identified a new feature in the cosmic ray energy spectrum above the ankle [5]. The energy spectrum above 10^{18} eV measured by Auger is shown in Figure 1.3. At $E \sim 1.3 \cdot 10^{19}$ eV the spectral index steepens from $\gamma \sim 2.5$ to $\gamma \sim 3$. This third break point is called “instep”. The features of the observed

energy spectrum can be reproduced by using mass composition models that depend on the energy. The suppression of the flux above $E \sim 4 \cdot 10^{19}$ eV will be discussed more in detail in section 1.3.4.

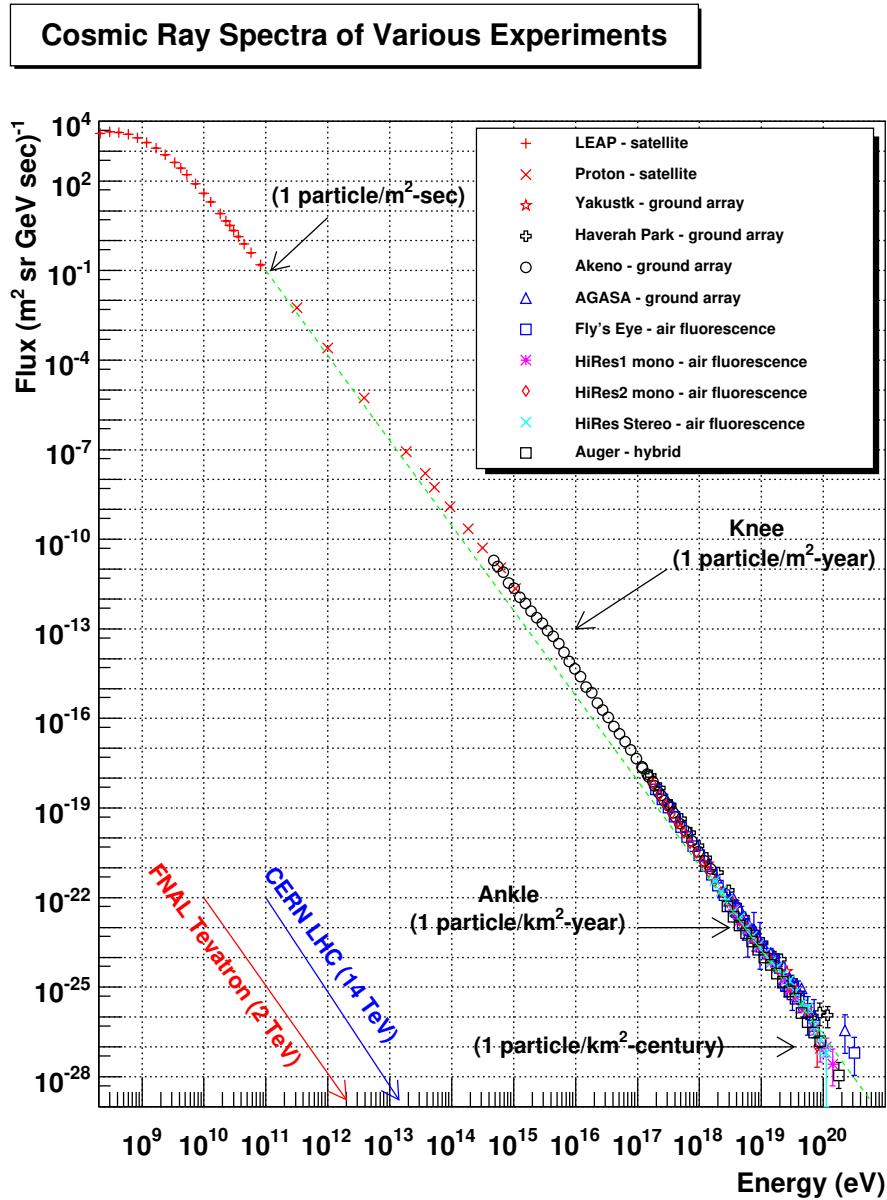


Figure 1.1: The cosmic ray energy spectra measured by different experiments. Figure from <http://www.physics.utah.edu/~whanlon/spectrum.html>

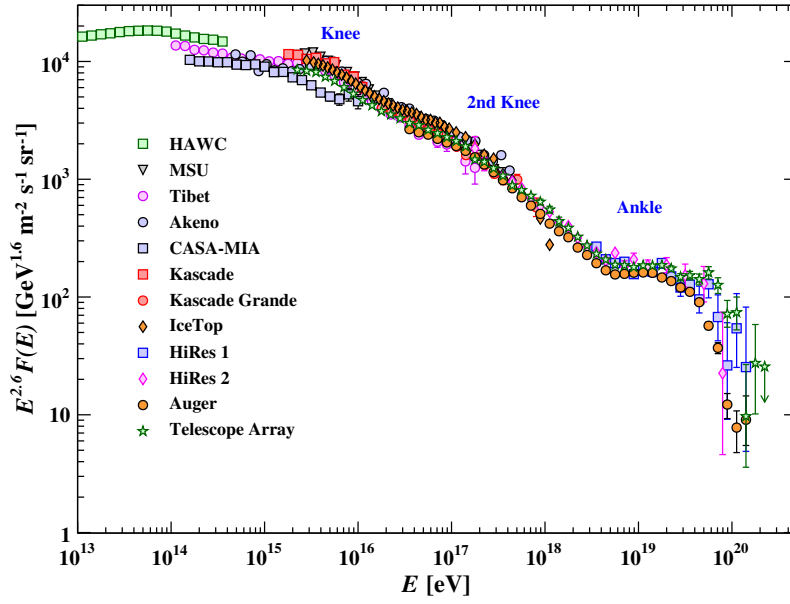


Figure 1.2: The cosmic ray energy spectra scaled by $E^{2.6}$ measured by different experiments. Figure from [4].

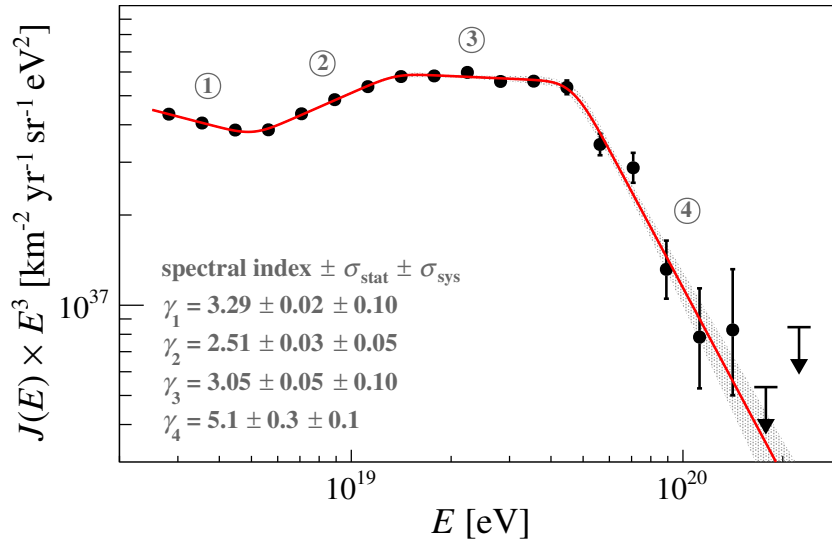


Figure 1.3: The cosmic ray energy spectrum scaled by E^3 measured by the Pierre Auger Observatory. In each energy region identified by a number the spectrum can be described by a power law with a different spectral index. The shaded band represents the statistical uncertainty of the fit. The upper limits shown in the plot are at the 90% confidence level. Figure from [6].

1.3 Acceleration, sources and propagation of the cosmic rays

The production of cosmic rays is usually associated to the most energetic astrophysical objects. The acceleration of charged cosmic rays can take place in regions of the interstellar medium in which a strong variable magnetic field is present. A static magnetic field can not change the magnitude of the velocity of a charged cosmic ray, because the work it does is null, but in the presence of a non-static magnetic field the magnitude of the velocity can change because of the induced electric field. Furthermore, a static electric field can not last long in most of the astrophysical environments because the ionised gases are very highly conductive. The first attempt to explain the acceleration mechanism was made by E. Fermi in 1949 [7]. He developed a model based on stochastic interactions of charged particles with ionised gas clouds, but his model failed to explain the cosmic ray energy spectrum. Today, cosmic rays are believed to be accelerated according to the diffusive shock acceleration model, that is derived by applying the Fermi mechanism to astrophysical shock waves such as the ones that are produced after a gravitational collapse. After their production and acceleration, the cosmic rays travel through magnetic fields in the interstellar and intergalactic medium and then reach the Earth. In the following sections the acceleration models, the candidate sources and the propagation mechanisms of the cosmic rays will be treated in detail.

1.3.1 The Fermi acceleration

The Fermi model is based on the interactions of charged relativistic particles ($v \sim c$) with moving magnetic clouds in the interstellar medium¹. The clouds act like magnetic mirrors on which charged particles can be reflected. A charged particle is accelerated or decelerated depending on whether it undergoes an head-to-head collision or a head-to-tail collision. The collision between a charged particle with velocity v and a moving magnetic cloud with velocity V is shown in Figure 1.4. Referring to this figure, the probability for an head-to-head collision is proportional to $v - V \cos \theta_1$ and is greater than the one for a head-to-tail collision, which is proportional to $v + V \cos \theta_1$. The particle undergoes several collisions inside the cloud, so it is randomly scattered when exiting the cloud:

$$\langle \cos \theta_2 \rangle = 0. \quad (1.2)$$

Considering the probability to have an head-to-head collision, for $v \sim c$ the average value of $\cos \theta_1$ is given by:

$$\langle \cos \theta_1 \rangle = \frac{\int_{-1}^1 \cos \theta_1 (1 - \frac{V}{c} \cos \theta_1) d \cos \theta_1}{\int_{-1}^1 (1 - \frac{V}{c} \cos \theta_1) d \cos \theta_1} = -\frac{V}{3c}. \quad (1.3)$$

¹Typically, astrophysical ionised gases are collisionless i.e. the mean free path of the Coulomb collisions is greater than their size. This means that the collisions a charged particle undergoes inside the cloud are due to the variable magnetic field.

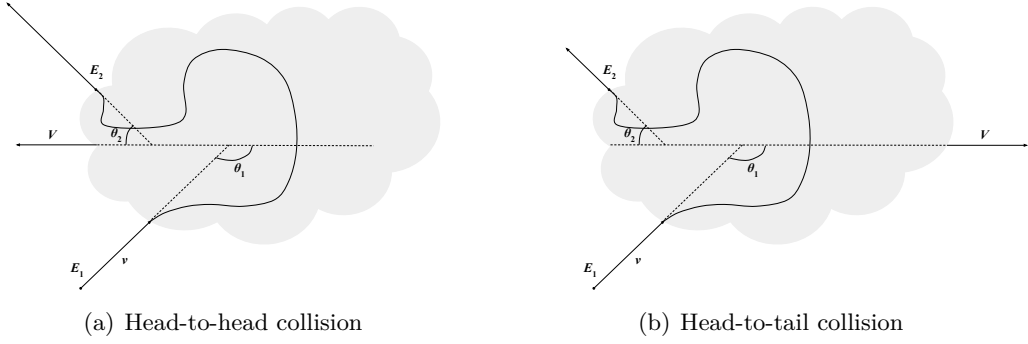


Figure 1.4: Collision between a charged particle with velocity v and energy E_1 with a moving magnetic cloud with velocity V . The particle undergoes several collisions inside the cloud and then exits with an energy E_2 . An head-to-head collision (a) and a head-to-tail collision (b) are shown.

The mass of the cloud is considered to be infinite, so its velocity does not change after the reflection. In the cloud reference frame $E_1^* = E_2^*$ and

$$E_1^* = \frac{1}{\sqrt{1 - \frac{V^2}{c^2}}} E_1 \left(1 - \frac{V}{c} \cos \theta_1\right). \quad (1.4)$$

The energy of the particle when it exits the cloud with respect to an external observer is:

$$E_2 = \frac{1}{\sqrt{1 - \frac{V^2}{c^2}}} E_2^* \left(1 + \frac{V}{c} \cos \theta_2\right). \quad (1.5)$$

Taking into account Eq. 1.4, this equation can be rewritten as:

$$E_2 = \frac{1}{1 - \frac{V^2}{c^2}} E_1 \left(1 - \frac{V}{c} \cos \theta_1\right) \left(1 + \frac{V}{c} \cos \theta_2\right). \quad (1.6)$$

By the knowledge of E_1 and E_2 , it is possible to calculate the percentage change in the energy of the charged particle:

$$\frac{\Delta E}{E} = \frac{E_2 - E_1}{E_1} = \frac{1}{1 - \frac{V^2}{c^2}} \left[1 - \frac{V}{c} \cos \theta_1 + \frac{V}{c} \cos \theta_2 - \frac{V^2}{c^2} \cos \theta_1 \cos \theta_2\right] - 1. \quad (1.7)$$

Using Eq. 1.2 and Eq. 1.3, the average percentage change in the energy is

$$\left\langle \frac{\Delta E}{E} \right\rangle = \frac{1}{1 - \frac{V^2}{c^2}} \left(1 + \frac{V^2}{3c^2}\right) - 1. \quad (1.8)$$

Assuming $V \ll c$ and expanding to second order in $\frac{V}{c}$,

$$\left\langle \frac{\Delta E}{E} \right\rangle \sim \frac{4}{3} \frac{V^2}{c^2}. \quad (1.9)$$

This is the second order Fermi acceleration. It predicts a power law energy spectrum, but it does not explain the observations because the spectral index can assume in principle any value. Furthermore, it is too slow because $\frac{V^2}{c^2} \sim 10^{-8}$ even in supernovae. These problems will be solved by the diffusive shock acceleration model.

1.3.2 The diffusive shock acceleration

The diffusive shock acceleration model takes the moves from the Fermi acceleration. If the Fermi acceleration mechanism is applied to shock waves, such as the ones around the supernova remnants, the average percentage change in the energy becomes linear in $\frac{V}{c}$. Considering a shock wave that propagates with a locally plane wave front, the downstream high-pressure region and the upstream low-pressure region are located respectively behind and in front of the shock front. A relativistic charged particle that crosses the shock front suffers a great number of collisions because of the turbulent magnetic field, so its velocity distribution becomes isotropic in the reference frame in which the gas is at rest on both sides of the shock front. The particle can thus cross the shock front several times in an head-to-head collision (the velocity of the shock is supposed to be much lower than the speed of light). Referring to Figure 1.5, in the shock wave rest frame the gas in the downstream region moves away from the shock front with velocity u_2 , while the gas in the upstream region moves towards the shock front with velocity u_1 . A particle crossing the wave front goes towards a gas that is moving with a velocity $V = u_1 - u_2$ with respect to the gas the particle is in. The

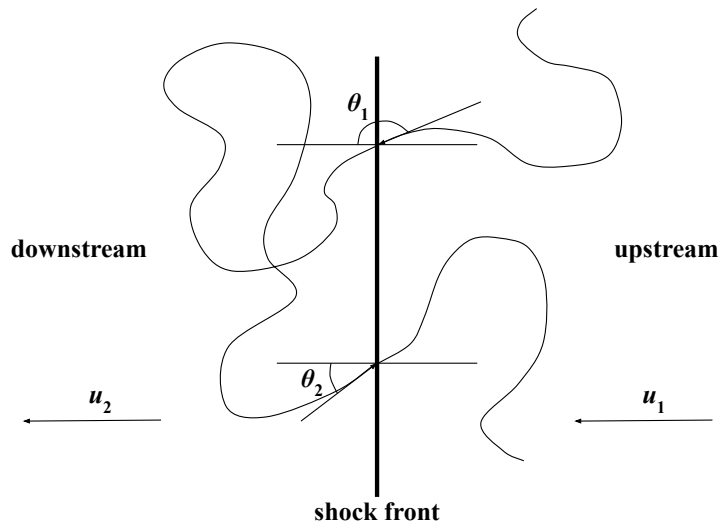


Figure 1.5: A charged particle crossing a plane shock front. The shock front is moving from left to right. Every time the particle crosses the shock front it undergoes an head-to-head collision.

particle have a probability to cross the wave front that is proportional to $\cos \theta_1$ or to $\cos \theta_2$ depending on the side it is in. So

$$\langle \cos \theta_1 \rangle = \frac{\int_{-1}^0 \cos^2 \theta_1 d \cos \theta_1}{\int_{-1}^0 \cos \theta_1 d \cos \theta_1} = -\frac{2}{3} \quad (1.10)$$

and

$$\langle \cos \theta_2 \rangle = \frac{\int_0^1 \cos^2 \theta_2 d \cos \theta_2}{\int_0^1 \cos \theta_2 d \cos \theta_2} = \frac{2}{3}. \quad (1.11)$$

Recalling Eq. 1.7, the average percentage change in the energy of the particle is:

$$\left\langle \frac{\Delta E}{E} \right\rangle = \frac{1}{1 - \frac{V^2}{c^2}} \left(1 + \frac{4V}{3c} + \frac{4V^2}{9c^2} \right) - 1. \quad (1.12)$$

Expanding to first order in $\frac{V}{c}$, the average energy gain is:

$$\left\langle \frac{\Delta E}{E} \right\rangle \sim \frac{4V}{3c}. \quad (1.13)$$

This is the diffusive shock acceleration, also known as the first order Fermi acceleration.

If P is the probability of the particle to remain in the shock region after one acceleration cycle and N_0 is the starting number of particles, after n cycles the number of particles in the shock region is:

$$N = N_0 P^n. \quad (1.14)$$

The energy of a particle with a starting energy E_0 after n cycles is:

$$E = E_0 \left(1 + \left\langle \frac{\Delta E}{E} \right\rangle \right)^n. \quad (1.15)$$

Putting together Eq. 1.14 and Eq. 1.15,

$$\frac{N}{N_0} = \left(\frac{E}{E_0} \right)^{\frac{\ln P}{\ln(1 + \langle \frac{\Delta E}{E} \rangle)}}. \quad (1.16)$$

Then

$$\frac{dN}{dE} \propto E^{-\gamma}, \quad (1.17)$$

where

$$\gamma = 1 - \frac{\ln P}{\ln(1 + \langle \frac{\Delta E}{E} \rangle)}. \quad (1.18)$$

So a power law energy spectrum is predicted. Using a classical kinetic approach due to Bell [8], it can be demonstrated that $P = 1 - \frac{4V}{3c}$. So in a first order approximation:

$$\gamma = 1 - \frac{\ln(1 - \frac{4V}{3c})}{\ln(1 + \langle \frac{\Delta E}{E} \rangle)} \sim 2 \quad (1.19)$$

and

$$\frac{dN}{dE} \propto E^{-2}. \quad (1.20)$$

The derived spectral index is close to the observed one and can be even steeper if the propagation in the interstellar medium is taken into account. The diffusive shock acceleration can explain the lower region of the cosmic ray energy spectrum shown in Figure 1.1 i.e. the energy spectrum of the galactic cosmic rays.

1.3.3 The sources of the cosmic rays

The cosmic rays with an energy up to the knee are likely produced in our galaxy by supernova remnants, but the origin of the highest energy cosmic rays remains more uncertain. The diffusive shock acceleration predicts a maximum energy that can be achieved within a source, because a charged particle has to remain trapped inside the source until the energy E is reached i.e. the Larmor radius r_L of the particle has to remain smaller than the source size R :

$$r_L = \frac{p}{ZeB} < R. \quad (1.21)$$

Taking into account the velocity of the scattering centers $\beta_s c$ (velocity of the shock), the maximum achievable energy is given by:

$$E_{\max} = \beta_s c ZeBR, \quad (1.22)$$

where Ze is the charge of the particle and B is the magnetic field of the source. Eq. 1.22 is called Hillas criterion [9] and provides a benchmark maximum energy up to which a charged particle can be accelerated, but it does not take into account the efficiency of the acceleration mechanism and the energy losses. Using the Hillas criterion, it is possible to identify which astrophysical objects satisfy the requirements to accelerate a particle with a certain charge up to a specific energy. The so-called Hillas plot, in which each source is classified according to its size and its magnetic field, is shown in Figure 1.6. Within the accelerating region, processes entailing energy losses can take place. Therefore, the maximum energy achieved can be computed as the interplay between the rate of acceleration and the rate of the considered processes.

Below the knee the cosmic rays are considered to have a galactic origin, while the transition between galactic and extragalactic cosmic rays is believed to take place between the knee and the ankle. Among the candidate sources for the galactic cosmic rays there are supernova remnants and pulsars. Candidate sources for the extragalactic cosmic rays include neutron stars, Active Galactic Nuclei (AGN) and Gamma Ray Bursts (GRBs).

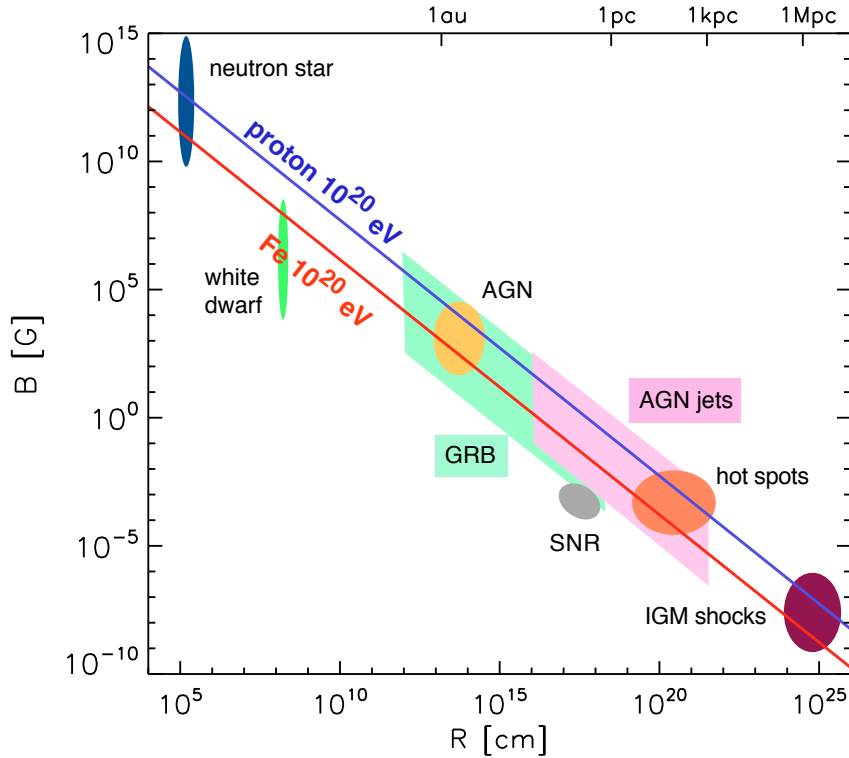


Figure 1.6: The Hillas plot. The size of the source is plotted on the x-axis, the magnetic field of the source is plotted on the y-axis. The plot shows the regions that correspond to different astrophysical objects. For each particle charge and maximum energy, Eq. 1.22 establishes a linear relationship between R and B , so each primary particle is represented by a line once a maximum energy is fixed. Given a certain particle and a certain maximum energy, it is possible to identify the sources that are able to accelerate that particle up to that energy by comparing the corresponding line with the regions that identify the astrophysical objects. The blue and the red line, corresponding respectively to protons and iron nuclei with the same energy $E = 10^{20}$ eV, show that the acceleration of nuclei is less demanding than the one of protons because of the larger Ze . Figure from [10].

1.3.4 The propagation of the cosmic rays and the GZK cutoff

Once the cosmic rays escape from their acceleration regions, they can travel long distances and then eventually reach the Earth. The propagation of the cosmic rays that are produced in our galaxy is affected by the galactic magnetic field, which has a large-scale (regular) component that is of the order of a μG and a small-scale (turbulent) component. The Larmor radius of a charged particle propagating in our galaxy is given by the same expression in Eq. 1.21, being B in this case the component of the galactic magnetic field perpendicular to the direction of the particle. At energies below the knee,

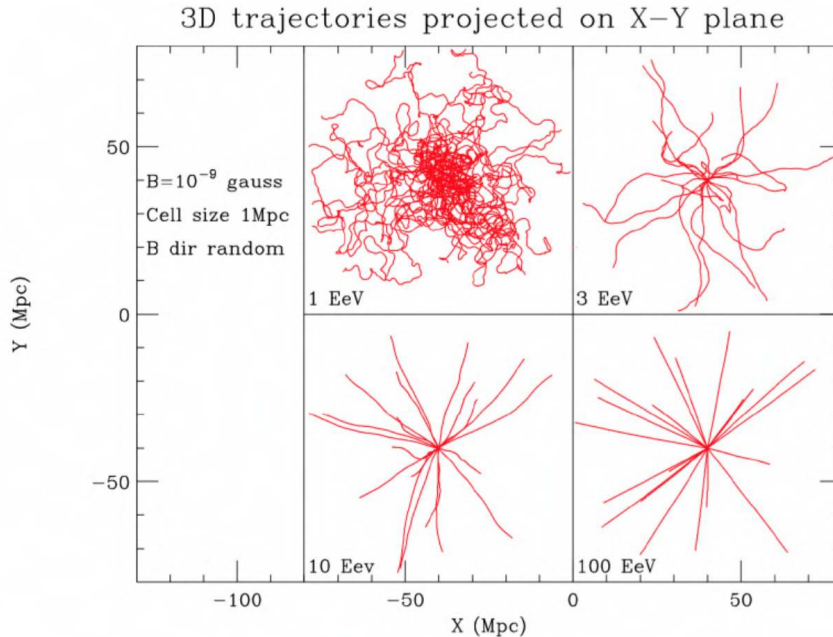


Figure 1.7: Projected view of 20 trajectories of proton primaries emanating from a point source for several energies. Trajectories are plotted until they reach a physical distance from the source of 40 Mpc. Propagation energy losses are not considered. Figure from [12].

the cosmic rays have a Larmor radius that is smaller than the field correlation scale, so they propagate in a diffusive regime [11]. At these energies the Larmor radius does not exceed the thickness of the galactic disk, so the cosmic rays remain confined inside the galaxy. When the energy of the cosmic rays is high enough to make the Larmor radius greater than the galactic disk thickness, the particles, whose propagation is no longer diffusive, can escape from the galaxy.

In addition to being affected by the galactic magnetic field, the cosmic rays that propagate in our galaxy can undergo radioactive decays, spallation processes, convective transport in the galactic winds, energy losses and energy gains.

The cosmic rays that are produced outside our galaxy travel through the intergalactic medium before reaching the Earth. The magnetic fields of the intergalactic medium are usually described by using a simple model that consists of cells with a size of ~ 1 Mpc and a randomly oriented mean magnetic field of strength ≤ 1 nG. The trajectories of the cosmic rays are affected by these magnetic fields even if they are small. The projected trajectories of 20 protons propagating in the intergalactic medium for different primary energies without considering the energy losses are shown in Figure 1.7. Protons at $E = 1$ EeV suffers from diffusive propagation, while at $E = 100$ EeV the propagation is basically rectilinear [12]. The situation changes for nuclei, because at the same energies they have a smaller Larmor radius because of their largest charge and so their propagation is less rectilinear.

Unlike the interactions with the intergalactic magnetic fields, the interactions with the cosmic backgrounds change the energy and the composition of the cosmic rays and produce secondary gamma rays and neutrinos. The backgrounds in the intergalactic medium are represented by the photons of the Cosmic Microwave Background (CMB)² and by the infrared, optical and ultra-violet (IR-UV) photons. The CMB spectrum is peaked at longer wavelengths than the IR-UV ones, but UHECRs can interact with the CMB photons via photo-pion and photo-pair production. In 1966 Greisen [13] and Zatsepin and Kuzmin [14] independently predicted the suppression of the flux of the cosmic rays above 10^{20} eV because of the energy losses due to UHECR interactions with the CMB photons. This feature is called Greisen-Zatsepin-Kuzmin (GZK) cutoff. Ultra high energy protons interact with the CMB photons producing pions through the Delta resonance:

$$p + \gamma_{\text{CMB}} \rightarrow \Delta^+ \rightarrow N + \pi, \quad (1.23)$$

where γ_{CMB} is the CMB photon, N is a nucleon and π is a π^0 or a π^+ . The energy threshold of the process can be calculated by imposing that the center-of-mass energy has to be equal to the sum of the nucleon and pion mass:

$$E_{\text{CM}} = \sqrt{(E_p + E_\gamma)^2 - |\vec{p}_p + \vec{p}_\pi|^2} = m_p + m_\pi. \quad (1.24)$$

This condition can be rewritten as:

$$2E_p E_\gamma (1 - \cos \theta) = m_\pi^2 + 2m_p m_\pi, \quad (1.25)$$

where θ is the angle between the two particles. In the case of a head-to-head collision ($\cos \theta = -1$) the energy threshold of the proton is given by:

$$E_p^{\text{th}} = \frac{m_\pi(m_\pi + 2m_p)}{4E_\gamma}. \quad (1.26)$$

Considering the energy of a typical CMB photon ($\sim 10^{-3}$ eV), the proton energy threshold for the photo-pion production is $E_p^{\text{th}} \sim 7 \cdot 10^{19}$ eV. The proper calculation requires the integration over the Planck spectrum of the CMB and over all the collision angles. Therefore the proton energy threshold for the photo-pion production reduces to $E_p^{\text{th}} \sim 10^{19}$ eV.

Using the photo-pion production cross section $\sigma_{\gamma p} \sim 2.5 \cdot 10^{-32}$ m² and the number density of CMB photons $n_\gamma \sim 5 \cdot 10^8$ m⁻³, the mean free path for a single collision is given by [15]:

$$\lambda = \frac{1}{\sigma_{\gamma p} n_\gamma} \sim 10^{23} \text{ m} \sim 3 \text{ Mpc}. \quad (1.27)$$

A proton undergoes an energy loss of about 10% in each GZK interaction. The mean energy of protons as a function of propagation distance through the CMB is shown in Figure 1.8. The distance traveled by a proton before reaching an energy below the

²The Cosmic Microwave Background is a relic radiation from the early universe that has a thermal spectrum of a black body with a temperature of 2.7 K.

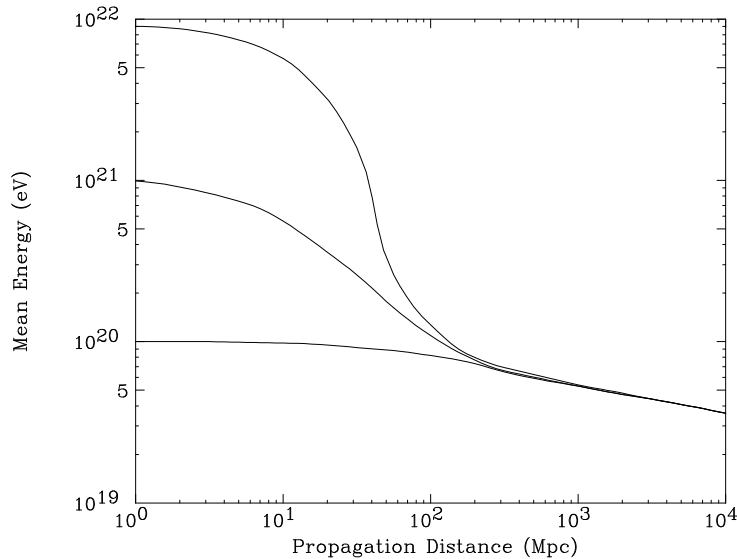


Figure 1.8: Mean energy of protons as a function of propagation distance through the CMB for different energies at the source (10^{22} eV, 10^{21} eV, and 10^{20} eV). Figure from [12].

energy threshold for the photo-pion production is ~ 100 Mp. This means that the highest energy protons have to be produced within this distance from the Earth. If they are produced far from our galaxy the result is a suppression of their flux at energies above the photo-pion production energy threshold.

If a similar calculation is carried out [15] for the electron-positron photo-pair production process,

$$p + \gamma_{\text{CMB}} \rightarrow p + e^+ + e^-, \quad (1.28)$$

the resulting energy threshold for protons is $\sim 10^{18}$ eV. Since in the ultra-relativistic limit the cross section for this process is $\sigma_{\text{pair}} = 10^{-30}$ m², the fractional loss of energy for each photo-pair production event is 10^{-5} above threshold. This results in a distortion of the particle spectrum down to energies of about 10^{18} eV. This feature is called “dip” [16, 17].

The previous calculations refer only to protons. Except neutrinos, all particle species can interact with the CMB. The panorama of the interactions of the different particle species with the CMB is shown in Figure 1.9. If heavier nuclei are considered, the dominant photo-disintegration interactions lead to a cutoff at an energy similar to that of protons. The same occurs with photons whose dominant interactions are the pair production processes.

As regards ultra high energy neutrinos, they do not interact with the CMB but they undergo a GZK-like interaction with the cosmological neutrinos ν_c . As soon as the center-of-mass energy of this interaction becomes large enough to open the inelastic channels, the cross section $\sigma_{\nu\nu_c}$ increases [18]. The universe becomes opaque to these

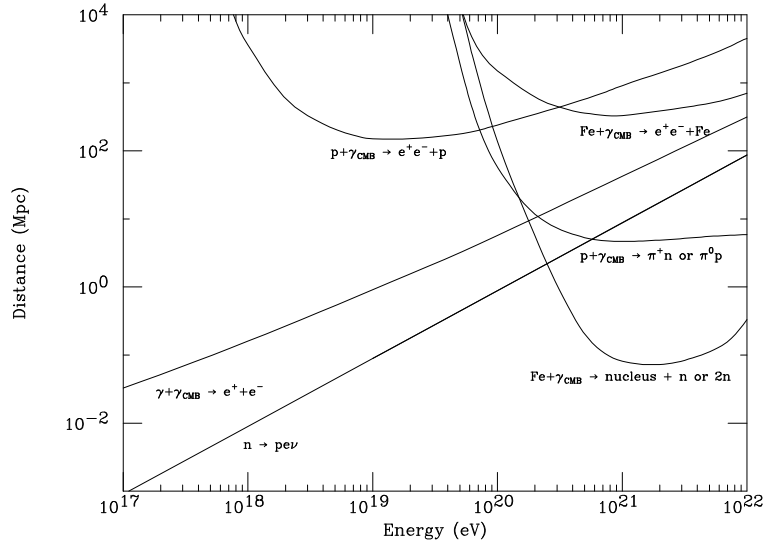


Figure 1.9: Panorama of the interactions of possible cosmic primaries with the CMB. Curves marked by “ $p + \gamma_{\text{CMB}} \rightarrow e^+ e^- + p$ ” and “ $Fe + \gamma_{\text{CMB}} \rightarrow e^+ e^- + p$ ” are energy loss lengths (the distance for which the proton or Fe nucleus loses $1/e$ of its energy due to pair production). The curve marked by “ $p + \gamma_{\text{CMB}} \rightarrow \pi^+ n$ or $\pi^0 p$ ” is the mean free path for photo-pion production of a proton on the CMB. The curve marked “ $Fe + \gamma_{\text{CMB}} \rightarrow \text{nucleus} + n$ or $2n$ ” is the mean free path for a photo-nuclear reaction where one or two nucleons are chipped off the nucleus. The curve marked “ $\gamma + \gamma_{\text{CMB}} + \gamma_{\text{CMB}} \rightarrow e^+ e^-$ ” is the mean free path for the interaction of a high energy photon with the CMB. Added for reference is the mean decay length for a neutron indicated by “ $n \rightarrow p e \nu$ ”. Figure from [12].

neutrinos when the interaction $\nu\nu_c \rightarrow Z^0$ becomes resonant, which happens at $E_\nu \sim 10^{21}$ eV.

1.4 Interaction of the cosmic rays with the atmosphere

The high energy hadrons, photons and electrons that enter the atmosphere interact with the nuclei from the air and produce cascades of secondary particles. The schematic views of an electromagnetic (EM) shower initiated by a photon and an hadronic shower initiated by an hadronic cosmic ray are shown in Figure 1.10. A photon that converts in the Coulomb field of a nucleus produces a $e^+ e^-$ pair, each of which produces photons via bremsstrahlung that then produce $e^+ e^-$ pairs and so on. The result is an EM cascade. An hadronic particle that interact with a nucleus, on the other hand, produces a large number of nuclear fragments, neutral and charged pions and kaons. The nuclear interactions carry away a large part of the initial energy of the hadronic particle. Neutral pions have a short lifetime and decay immediately in two photons, each one

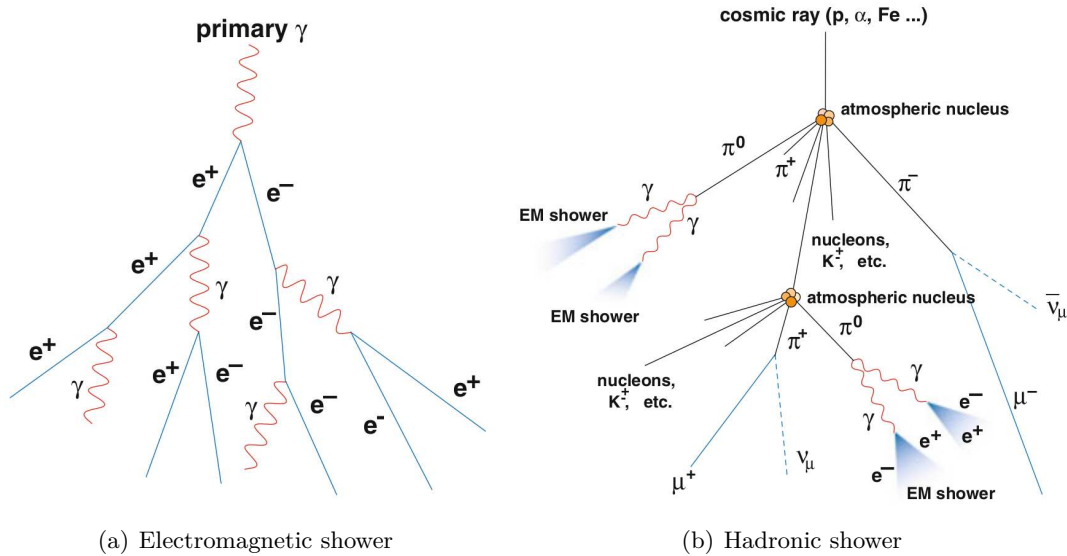


Figure 1.10: Schematic views of an electromagnetic shower (a) and an hadronic shower (b). Figures from [19].

giving rise to an EM shower, while charged pions, whose lifetime is larger, can interact with the atmosphere before decaying and produce other pions. As soon as the energy of the charged pions becomes sufficiently low, they decay producing muons and neutrinos. Also the decay of the other charged mesons results in the production of muons and neutrinos, while other neutral mesons produce additional EM showers. Penetrating muons and neutrinos produced during the shower development propagate straight to the ground. Both astrophysical neutrinos and neutrinos produced in the interaction of the cosmic rays with the atmosphere are not easy to detect because of their small cross section.

1.4.1 Electromagnetic showers

The main features of an EM shower can be inferred by using the simple Heitler model [21]. Under the assumption that the energy E_0 of the primary particle is much greater than the critical energy E_c (the energy at which the radiation energy loss becomes greater than the ionization energy loss), this simple model assumes that after one splitting length X_s electrons give half of their initial energy to a bremsstrahlung photon, while photons create an electron and a positron, each one with half of the original energy of the photon. The characteristic amount of matter traversed for these related interactions is referred as X_0 and is called the radiation length, which is usually measured in g cm^{-2} . The splitting length X_s is the amount of matter traversed by an electron or a photon before losing on average half of its energy and is given by $X_s = X_0 \ln 2$ from the resolution of the equation $\langle E(x) \rangle = E_0 e^{-x/X_0}$ by imposing $\langle E(X_s) \rangle = E_0/2$.

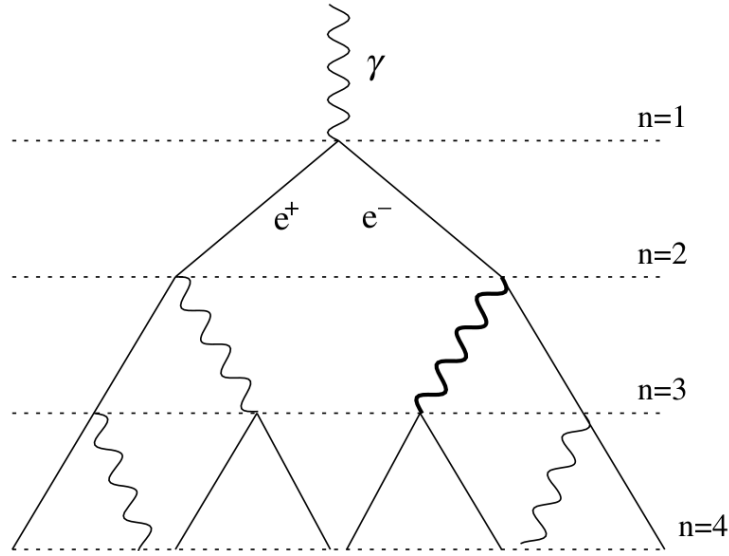


Figure 1.11: Schematic view of the Heitler model for the development of an electromagnetic shower. Figure from [22].

The amount of matter traversed after n splitting lengths is given by $X_n = nX_0 \ln 2$ and the total number of electrons and photons is $N = 2^n = (e^{\frac{X_n}{X_0}})^n = e^{\frac{X_n}{X_0}}$. When the energy of the particles becomes lower than the critical energy E_c the multiplication process stops. The scheme of the Heitler model is shown in Figure 1.11. If the shower is initiated by a particle with energy E_0 the maximum size of the shower N_{\max} is reached when all the particles have an energy equal to E_c . Considering that $N_{\max} = 2^{n_c}$, where n_c is the number of splitting lengths needed to reduce the energy of the particles to E_c , and that $E_c = E_0/N_{\max}$, the depth X_{\max} at which the shower reaches the maximum size is given by $X_{\max} = n_c X_0 \ln 2 = (\ln \frac{E_0}{E_c} / \ln 2) X_0 \ln 2 = X_0 \ln \frac{E_0}{E_c}$. This is the depth of the shower maximum for a pure EM shower. Its dependence on the energy of the primary particle is predicted also by more accurate models and is experimentally confirmed.

1.4.2 Hadronic showers

Hadronic showers can be modeled using a similar approach as for EM showers [23, 24]. However, hadrons that interact with the nuclei of the atmosphere lose a significant part of their energy in the nuclear processes. Furthermore, the multiparticle production of hadrons together with the particle decays make it hard to treat the shower development in an analytical way. The calculation of the hadronic shower development is usually performed numerically using Monte Carlo simulations. However, the main features of the hadronic showers can be inferred by generalizing the Heitler model [22]. According to this generalization (see Figure 1.12) [25], an hadron with energy E_0 that interact in the atmosphere produces n_{tot} particles with energy E_0/n_{tot} .

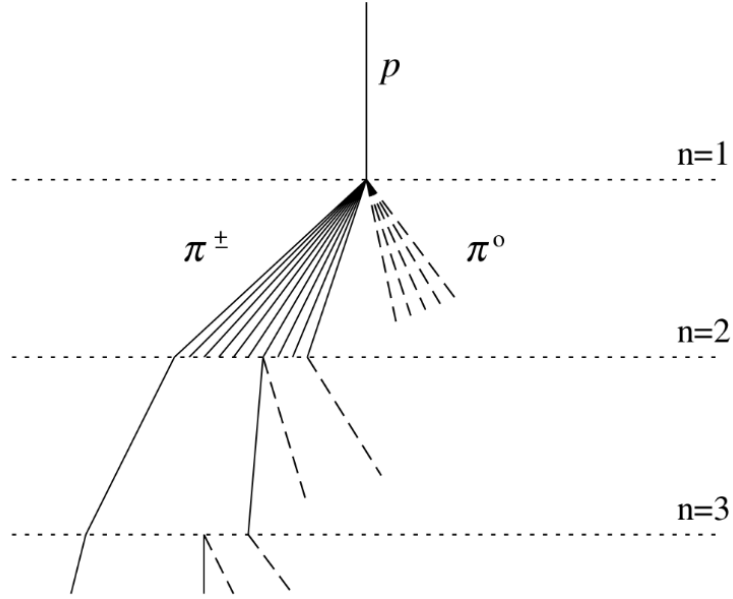


Figure 1.12: Schematic view of the generalization of the Heitler model for the development of a hadronic shower. Solid lines represent charged pions, while dashed lines stand for neutral pions that do not interact but decay producing electromagnetic sub-showers. Not all the pions are shown after the level $n=2$. Figure from [22].

One-third of them are neutral pions, that do not interact and produce EM sub-showers, while two-third of them are charged pions and their number is referred as n_{ch} . If the energy of the charged pions is greater than a typical decay energy E_{dec} , they interact again with air nuclei after travelling a distance corresponding to the mean inelastic interaction length λ_{had} . When the energy of the charged pions becomes lower than E_{dec} , they decay producing one muon per pion. In each hadronic interaction, neutral pions carry away one-third of the energy of the original hadron and then they decay transferring their energy to the EM component of the shower. After n steps the energy of the hadronic component and of the EM component is, respectively,

$$E_{\text{had}} = \left(\frac{2}{3}\right)^n E_0 \quad (1.29)$$

and

$$E_{\text{EM}} = E_0 - E_{\text{had}} = \left[1 - \left(\frac{2}{3}\right)^n\right] E_0. \quad (1.30)$$

After $n \approx 6$ most of the energy of the initial hadron is carried by the EM component of the shower, that thus mainly affects the depth of the shower maximum. If only EM particles produced in the first hadronic interaction are considered, the depth of the shower maximum can be written as:

$$X_{\text{max(had)}} \approx \lambda_{\text{had}} + X_{\text{max(EM)}} \left(\frac{E_0}{2n_{\text{tot}}}\right) \sim \lambda_{\text{had}} + X_0 \ln \left(\frac{E_0}{2n_{\text{tot}} E_c}\right). \quad (1.31)$$

When E_{dec} is reached, charged pions decay producing one muon each. If this happens at $n = n_{\text{d}}$, the energy of the charged pions is then $E = E_{\text{dec}} = E_0/(n_{\text{ch}})^{n_{\text{d}}}$ and the number of muons is given by $N_{\mu} = (n_{\text{ch}})^{n_{\text{d}}}$. Using these two equations the number of muons can be expressed as:

$$N_{\mu} = \left(\frac{E_0}{E_{\text{dec}}} \right)^{\alpha}, \quad (1.32)$$

where $\alpha = \ln n_{\text{ch}}/\ln n_{\text{tot}}$. According to Eq. 1.32, N_{μ} depends on the energy of the initial hadron, the density of the air and the charged and total particle multiplicities of hadronic interactions.

If the particle that initiates the shower is a nucleus with mass number A , it can be treated as A independent nucleons with energy E_0/A (superposition model). Using the indices (A) and (p) for quantities that refers respectively to nuclei and nucleons, the maximum number of particles, the depth of the shower maximum and the number of muons for nucleus induced showers are given by:

$$N_{\text{max(EM)}}^{(A)}(E_0) = A \cdot N_{\text{max(EM)}}^{(p)}\left(\frac{E_0}{A}\right) \approx N_{\text{max(EM)}}^{(p)}(E_0), \quad (1.33)$$

$$X_{\text{max}}^{(A)}(E_0) = X_{\text{max}}^{(p)}\left(\frac{E_0}{A}\right), \quad (1.34)$$

$$N_{\mu}^{(A)} = A \cdot \left(\frac{E_0/A}{E_{\text{dec}}} \right) = A^{1-\alpha} \cdot N_{\mu}^{(p)}(E_0). \quad (1.35)$$

Both Eq. 1.34 and Eq. 1.35 depend on the mass of the nucleus that initiates the shower. As a consequence, the depth of the shower maximum of heavier nuclei is lower than that of lighter nuclei, while the number of muons is higher.

When averaged on many showers, the nucleon interaction points predicted by the superposition model are the same as more detailed calculations. Similarly, some main features of nucleus induced showers, such as the depth of the shower maximum or the number of muons, are well described by the superposition model.

The energy of the particle that initiates the shower can be inferred from the longitudinal profile of the shower, i.e. the energy deposited by the shower in the atmosphere as a function of the traversed depth X , that can be measured by detecting the fluorescence light emitted by the nitrogen molecules excited by the charged particles of the shower. The integral of the longitudinal profile gives a measurement of the calorimetric energy of the shower. The relation between the calorimetric energy of the shower and its total energy depends on the primary particle. Neutrinos and muons produced by hadronic primary particles do not interact or deposit only a small fraction of their energy into the atmosphere. The fraction of the non-detected energy depends in a first approximation only on the number of steps n at which the production of muons occurs. With $n = 5-6$ this fraction is 9–13% from Equation 1.29 [25], which is in good agreement with simulations.

Since the flux of the cosmic rays decreases with the energy (see section 1.2), the detection of the UHCRs is possible only with ground-based experiments that measure the secondary particles produced by their interaction with the atmosphere. The next chapter will be focused on the detection of the UHCRs with the Pierre Auger Observatory.

Chapter 2

The Pierre Auger Observatory

The Pierre Auger Observatory [26] is the largest cosmic ray observatory of the world. It is located near the town of Malargüe in the Province of Mendoza, Argentina. The Pierre Auger Observatory was designed to probe the origin and the nature of the highest energy cosmic rays. It combines a surface detector (SD) that consists of 1660 water Cherenkov stations covering an area of $\sim 3000 \text{ km}^2$ and a fluorescence detector (FD) that comprises 24 fluorescence telescopes that overlooks the SD array from four sites. The SD detects the Cherenkov light produced in water by the secondary particles of the air shower at ground level, while the FD measures the longitudinal profile of the air showers on clear moonless nights. Its hybrid nature allows to compensate for the limitations of the single detection techniques by complementary measurements. The array is located on the Pampa Amarilla plateau and the detectors have altitudes between 1340 m and 1610 m, resulting in a mean altitude of $\sim 1400 \text{ m}$ that corresponds to an atmospheric depth of $\sim 875 \text{ g cm}^{-2}$. The layout of the Pierre Auger Observatory is shown in Figure 2.1.

The construction of the Pierre Auger Observatory was started in 2002 and was completed in 2008. The Pierre Auger Observatory has been taking stable data since 2004, adding detectors as they became active until the full configuration was reached. In this chapter the detection techniques of the Pierre Auger Observatory will be described.

2.1 The surface detector

The surface detector is made up of 1660 water Cherenkov stations arranged in a triangular grid at a distance of 1500 m from each other (see Figure 2.1). This distance is required to have a minimum of five triggered stations for showers with an energy of 10^{19} eV and is a good compromise between costs, energy threshold and sampling of the shower at ground level [27]. At this distance, showers with an energy above $3 \cdot 10^{18} \text{ eV}$ are detected by the SD with a 100 % trigger efficiency [28] and a vertical shower with an energy of 10^{20} eV triggers approximately 10 stations, number that increases for inclined showers. The large area of $\sim 3000 \text{ km}^2$ covered by the SD is required by the low flux of the highest energy cosmic rays to have a sufficiently high statistics in

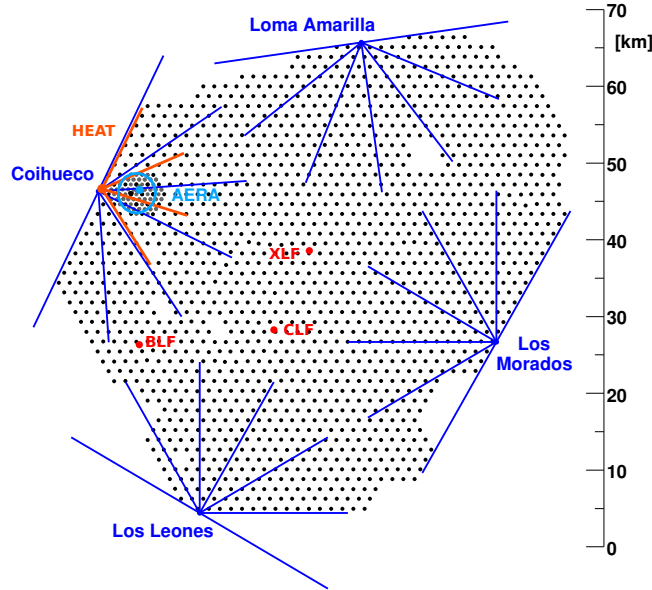


Figure 2.1: The layout of the Pierre Auger Observatory. Each black dot stands for a water Cherenkov station, while the blue lines represent the azimuthal field of views of the 24 fluorescence telescopes. The four fluorescence detector sites (Los Leones, Los Morados, Loma Amarilla, Coihueco), each of which with six telescopes, are shown. The Coihueco site hosts three extra high elevation (HEAT) telescopes, whose field of views are shown with red lines. The laser facilities (CLF and XLF) that monitor the aerosol content in the atmosphere and the weather balloon launching facility (BLF) are shown with red dots. A denser region of water Cherenkov detectors, named infill array, is located near the Coihueco site. The light-blue circle represents the area equipped with radio antennas (AERA). Figure from <https://pc.auger.unam.mx/>.

a reasonable time. A region of water Cherenkov stations arranged at a distance of 750 m from each other and called infill (see Figure 2.1) allows to detect showers with lower energies.

Each SD station consists of a cylindrical water tank with a diameter of 3.6 m and a height of 1.2 m. The tank is made of polyethylene and contains a sealed liner with a reflective inner surface filled with 1200 l of ultra-pure water. The relativistic charged particles that cross the water produce Cherenkov light that is collected by three photomultiplier tubes (PMTs) with a diameter of 9 inch. These PMTs are placed on the surface of the liner at a distance of 1.20 m from the center of the tank and look downward into the water through windows of clear polyethylene. The height of the tanks makes them sensitive also to high energy photons that produce $e^+ e^-$ pairs within their volume. The tanks are powered by batteries connected to two solar panels that provides an average of 10 W for the PMTs and electronics package consisting of a processor, GPS receiver, radio transceiver and power controller. A schematic view of a tank with its components is shown in Figure 2.2.

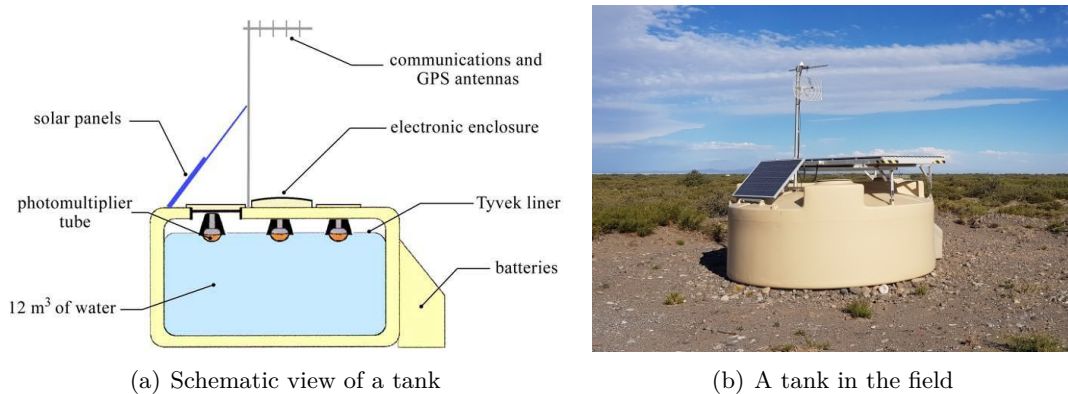


Figure 2.2: A schematic view of a tank with its component from [29] (a) and a personal photo of a tank placed in the Pampa Amarilla (b).

2.1.1 The electronics of the SD

The PMTs have a photocathode with a diameter of 9 inch that is grounded and eight dynodes that operate at a positive voltage. The high voltage supply is located on the PMT base and is controlled by the slow control system [30]. The PMTs operate at a nominal gain of $2 \cdot 10^5$ and have the signals from both the anode and the last dynode as outputs. The PMT base electronics amplifies and inverts the signal at the last dynode so that it is 32 times the charge gain of the anode. The anode signal is used for large signals, typically the ones from the tanks that are close to the shower core i.e. the intersection between the shower axis and the ground. Six channels of electronics digitize the signals from the anode and the dynode through six 10 bit Fast Analog to Digital Converters (FADCs) running at 40 MHz. The event timing and the communication synchronization are provided by a GPS receiver located at the top of the communication mast of each tank (see Figure 2.2). Two local triggers T1 and T2 (see section 2.1.3) are associated to a global trigger T3. The data acquisition system that is implemented on the station controller [30] transmits the time stamps of the T2 events to the Central Data Acquisition System (CDAS), which in response transmits T3 requests. T1 and T2 data corresponding to the T3 requests are build into an event and then transmitted to the CDAS together with calibration data.

2.1.2 The calibration of the SD

The Cherenkov light produced by the particles that cross the tanks is measured in units of Vertical Equivalent Muon (VEM), which is the average charge measured for a Vertical Centered Through-going (VCT) muon i.e. a vertical muon going through the center of the tank. However, only the signal from omni directional muons that trigger on coincidence of the three PMTs can be measured. The peak in the total charge distribution resulting from this measurement can be used to infer the value of VEM (see Figure 2.3(a)), which is obtained from a tank equipped with two vertically aligned

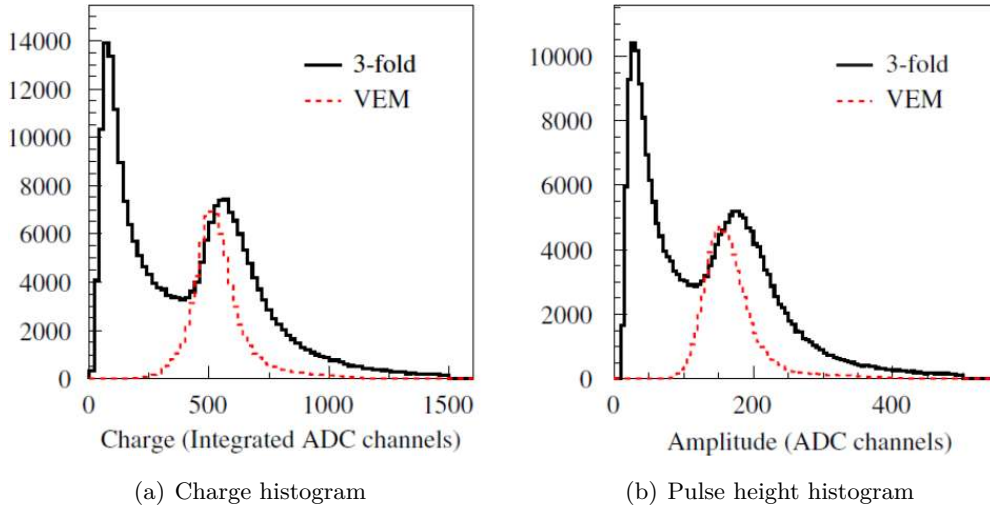


Figure 2.3: Charge (a) and pulse height (b) histograms from a tank triggered on coincidence of its three PMTs at a trigger level of five channels above baseline. In both histograms the signal from the three PMTs is summed. The black solid histograms refer to a tank simply triggered on a threefold coincidence, while the red dashed histograms refer to a tank triggered on central vertically aligned plastic scintillators. The bin containing the peak of the red dashed charge histogram is defined as a vertical equivalent muon. The peak on the left in the black solid histograms is due to low energy and corner-clipping muons convolved with the low threshold coincidence of the three PMTs. The muon peak of the black solid histograms is at a higher value compared to the one of the red dashed histograms because non-vertical muons produce more Cherenkov light. Figures from [32].

plastic scintillators and then applied to all the other tanks [31]. The purpose of the SD calibration is to measure the value of 1 VEM in terms of hardware units i.e. in integrated FADC channels. Referring to Figure 2.3(a), the muon peak of the black solid histogram will be referred as $Q_{\text{VEM}}^{\text{peak}}$, while the peak of the red dashed one as Q_{VEM} (or equivalently VEM). The relationship between $Q_{\text{VEM}}^{\text{peak}}$ and Q_{VEM} is $Q_{\text{VEM}}^{\text{peak}} = 1.09 Q_{\text{VEM}}$ for the sum of the three PMTs and $Q_{\text{VEM}}^{\text{peak}} = (1.03 \pm 0.02) Q_{\text{VEM}}$ for each PMT [32]. Together with the peak in the charge histogram, there is also the peak in the pulse height histogram (see Figure 2.3(b)), which is used as a reference unit for threshold levels and is related to the peak produced by a VCT muon. Using the same notation as for the charge, they will be referred respectively as $I_{\text{VEM}}^{\text{peak}}$ and I_{VEM} . The calibration is performed in three main steps:

1. The end-to-end gains of each of the three PMTs are set up to have $I_{\text{VEM}}^{\text{peak}}$ at 50 channels.
2. A local calibration is continually performed to determine $I_{\text{VEM}}^{\text{peak}}$ in channels. This step allows to adjust the electronics level trigger and to compensate for drifts.

3. The value of $Q_{\text{VEM}}^{\text{peak}}$ is determined to high accuracy using charge histograms, and the known relationship between $Q_{\text{VEM}}^{\text{peak}}$ and Q_{VEM} is used to obtain a conversion from the integrated signal of the PMT to VEM units.

2.1.3 The local trigger of the SD

The local trigger of the SD has two levels of selection named T1 and T2, whose purpose is to detect the electromagnetic and muonic components of an air shower. The T1 trigger has two independent modes. The first mode consists in a threshold trigger (T1-TH) requiring that the coincidence of all three PMTs is above $1.75 I_{\text{VEM}}^{\text{peak}}$. This threshold allows to reduce the rate of atmospheric muons from ~ 3 kHz to ~ 100 Hz. The T1-TH trigger can be used to select large signals that are not necessarily spread in time. Very inclined showers that are dominantly muonic because they traverse large atmospheric depths can be selected with this trigger. The second mode is a Time-over-Threshold (T1-ToT) trigger requiring that at least 13 bins in 120 FADC bins within a window of $3 \mu\text{s}$ are above $0.2 I_{\text{VEM}}^{\text{peak}}$ in coincidence of two out of three PMTs. The T1-ToT rate is lower than 2 Hz. This mode is used to select sequences of small signals spread in time. The T1-ToT trigger allows to select low energy showers with a core close to the tank dominated by the electromagnetic component or high energy showers with a distant core.

The T2 trigger reduces the rate of T1 triggers to ~ 20 Hz. T1-TH triggers are required to have a coincidence of all three PMTs above $3.2 I_{\text{VEM}}^{\text{peak}}$ to be promoted to T2-TH, while all T1-ToT triggers become T2-ToT. T2 triggers are then combined at the CDAS to form the T3 trigger, that initiates the data acquisition. A description of higher level triggers can be found in [33].

2.1.4 The SD event reconstruction

The size and timing of the signals registered by the single tanks are used to determine the shower properties i.e. the shower core, the shower size, the shower arrival direction and the shower energy.

The shower geometry can be reconstructed by fitting the start times of the signals, referred as t_i , in the single tanks. If the number of triggered tanks is high enough, the start times can be described by a concentric-spherical model (see Figure 2.4(a)) according to which the shower front is approximated with a sphere that inflates at the speed of light:

$$c(t_i - t_0) = |\vec{x}_{\text{sh}} - \vec{x}_i|, \quad (2.1)$$

where c is the speed of light, \vec{x}_i are the positions of the tanks on the ground and t_0 , \vec{x}_{sh} are respectively a virtual start time and a virtual origin of the shower development. An example of a fit according to this shower front evolution model is shown in Figure 2.4(b).

The lateral distribution function (LDF), which describes the decrease of the signals in the tanks as a function of the distance, can be fitted to obtain the impact point of

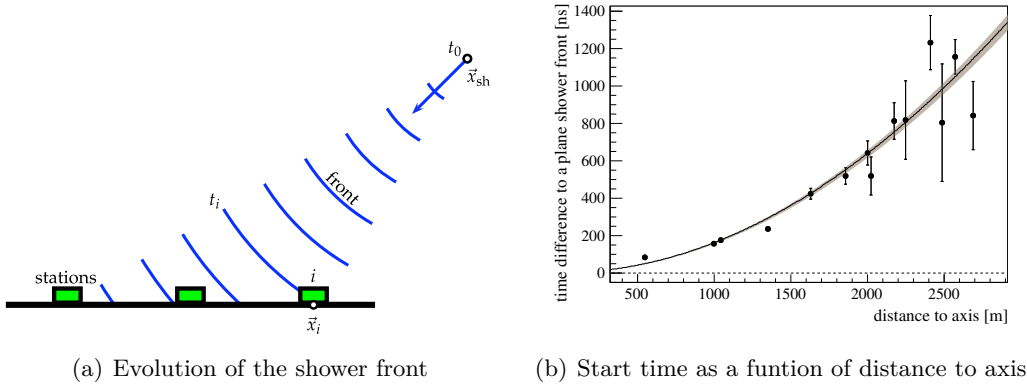


Figure 2.4: Schematic view of the evolution of a shower front (a) and start time relative to the timing of a plane shower front as a function of the perpendicular distance to the shower axis (b). The shaded line in Figure (b) represents the fit according to the shower front evolution model and its uncertainty. Figures from [26].

the shower on the ground, referred as \vec{x}_{gr} . The LDF can be described by a modified Nishimura-Kamata-Greisen function:

$$S(r) = S(r_{\text{opt}}) \left(\frac{r}{r_{\text{opt}}} \right)^{\beta} \left(\frac{r + r_1}{r_{\text{opt}} + r_1} \right)^{\beta + \gamma}, \quad (2.2)$$

where r_{opt} is the optimum distance from the shower core at which the fluctuations in the signal are minimised, $S(r_{\text{opt}})$, which is an estimator of the shower size and is used in the energy determination, is the signal corresponding to r_{opt} , $r_1 = 700$ m and β , γ are parameters that determine the slope of the LDF. For the SD array with 1500 m spaced stations the optimum distance is $r_{\text{opt}} = 1000$ m [34] and the corresponding signal is thus referred as $S(1000)$. An example of a footprint of a shower on the SD with the corresponding LDF is shown in Figure 2.5.

Using the virtual origin of the shower \vec{x}_{sh} coming from the geometrical reconstruction and the impact point of the shower on the ground \vec{x}_{gr} coming from the LDF fit, the shower axis \hat{a} can be determined:

$$\hat{a} = \frac{\vec{x}_{\text{sh}} - \vec{x}_{\text{gr}}}{|\vec{x}_{\text{sh}} - \vec{x}_{\text{gr}}|}. \quad (2.3)$$

Events with more than three stations have an angular resolution better than 1.6° , which becomes better than 0.9° for events with more than six stations [35].

The energy of the primary particle can be obtained using the estimator $S(1000)$. However, for a fixed energy, the attenuation of the particles of the shower and geometrical effects make $S(1000)$ decreasing with the zenith angle θ . Under the assumption of an isotropic flux for the primary cosmic rays, this attenuation can be determined using the Constant Intensity Cut (CIC) method [36]. The attenuation curve $f_{\text{CIC}}(\theta)$ i.e. $S(1000)$ as a function of θ is fitted with a third degree polynomial in $x = \cos^2 \theta - \cos^2 \bar{\theta}$,

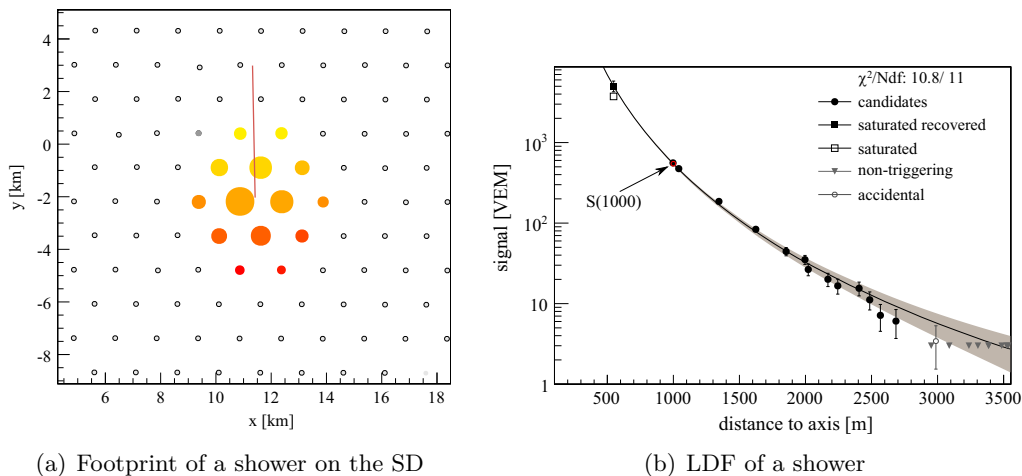


Figure 2.5: Signal induced by a shower on the 1500 m spaced stations of the SD (a) and the corresponding LDF (a). The different colors in Figure (a) refer to the time arrival of the shower front (signal arriving first are marked with yellow, signals arriving last with red), while the size of the markers is proportional to the logarithm of the signal. Figures from [26].

where $\bar{\theta} = 38^\circ$ is the median zenith angle for events measured by the SD with $\theta < 60^\circ$. The median zenith angle $\bar{\theta}$ is taken as a reference to convert $S(1000)$ to $S38$:

$$S38 = \frac{S(1000)}{f_{\text{CIC}}(\bar{\theta})}. \quad (2.4)$$

$S38$ is an energy estimator that is independent from the zenith angle and can be considered as the signal $S(1000)$ that a shower would have produced if it had arrived with a zenith angle of 38° . The hybrid nature of the Pierre Auger Observatory allows to calibrate $S38$ to the energy measured by the fluorescence detector, E_{FD} . This calibration is performed using a high quality set of hybrid data with $\theta < 60^\circ$ without relying on Monte Carlo simulations. The relation between $S38$ and E_{FD} can be described using the function:

$$E_{\text{FD}} = A \left(\frac{S38}{\text{VEM}} \right)^B, \quad (2.5)$$

where A and B are parameters determined by fitting the data. The energy of the SD is then given by:

$$E_{\text{SD}} = A \left(\frac{S(1000)}{f_{\text{CIC}}(\bar{\theta}) \text{VEM}} \right)^B, \quad (2.6)$$

and the ratio $E_{\text{SD}}/E_{\text{FD}}$ can be used to calculate the energy resolution of the SD. Given an FD energy resolution of 7.6%, the resulting SD energy resolution decreases from $\sim 21\%$ around 10^{18} eV to $\sim 10\%$ around 10^{19} eV [37].

For zenith angles $\theta > 60^\circ$, the signal in the SD stations is dominantly muonic and the energy estimator, called N_{19} , which is a relative scale factor relating the measured

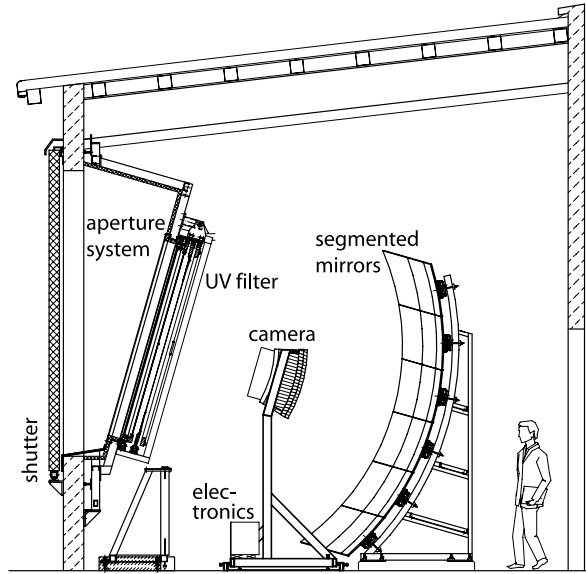


Figure 2.6: Schematic view of a FD telescope with its components. Figure from [26].

muon density at ground to a reference simulated one, is fitted to the data and calibrated to the energy measured by the FD [38].

2.2 The fluorescence detector

The fluorescence detector consists of 24 telescopes that overlooks the area covered by the SD [39]. It comprises four sites (“eyes”), called Los Leones, Los Morados, Loma Amarilla and Coihueco, each of which hosts six telescopes (see Figure 2.1). Each telescope has a field of view of $30^\circ \times 30^\circ$ in azimuth and elevation, resulting in an azimuthal coverage of 180° at each FD site. The minimum elevation of the telescopes is 1.5° above the horizontal, so they cover an elevation range between 1.5° and 31.5° with respect to the horizontal. A schematic view of a telescope is shown in figure 2.6. The charged particles of an air shower interact in the air with the nitrogen molecules, that get excited and then isotropically emit a radiation in the UV wavelength range between 300 nm and 400 nm when returning to the ground state. This radiation is called fluorescence light and can be detected with the fluorescence telescopes. The fluorescence light enters a telescope by passing through a diaphragm with a radius of 1.1 m covered by a Schott MUG-6 filter glass window. An annular corrector ring with an inner radius of 0.85 m and an outer radius of 1.1 m, made of 24 sectors of UV transmitting glass, corrects spherical aberration and eliminates coma aberration. The diaphragm, the filter and the corrector ring are held by the aperture system (see Figure 2.6). A segmented spherical mirror of $3.5 \text{ m} \times 3.5 \text{ m}$ focuses the fluorescence light onto a camera made of 440 hexagonal PMTs (pixels) arranged in 22 rows and 20

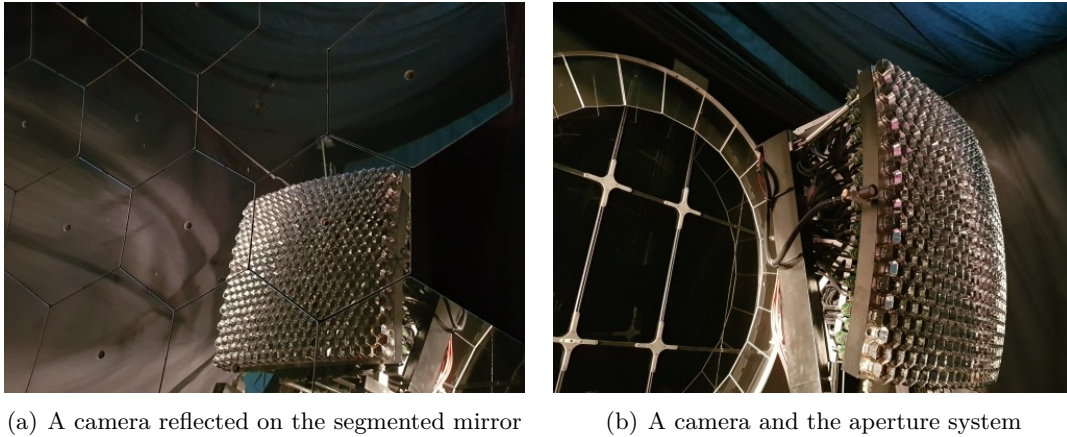


Figure 2.7: A camera reflected on the segmented mirror (a) and a camera with the aperture system behind it (b) at the Coihueco site. Personal photos.

columns (see Figure 2.7). The field of view for each PMT is 1.5° . Two sliding doors called shutters (see Figure 2.6) protect the telescope from daylight and weather. They are closed during daytime and close automatically at night if the wind is too high or if it rains. Furthermore, a curtain is placed behind the diaphragm to protect the camera from daylight in case of failures.

2.2.1 The electronics of the FD

The electronics of the FD ensures a large dynamic range and a strong background rejection, allowing also to anti-alias filter, digitize, and store signals from the PMTs. The PMT low and high voltage are provided by an Head Electronics (HE) unit that is soldered to the flying leads of the PMT. The nominal gain for the standard operation of the FD is $5 \cdot 10^4$. Ten distribution boards are placed behind the camera, each serving 44 PMTs. The HE of each PMT is connected to a distribution board, which provides both low and high voltage and receives the output signals. The signal is shaped and digitized by a front-end electronics unit that contains 20 Analog Boards (ABs), 20 First Level Trigger (FLT) boards and 1 Second Level Trigger (SLT) board. The ABs, each of which collect data from one column of the camera, have a dynamic range of 15 bits and a timing of 100 ns. The event data from the front-end electronics are read by a computer called Mirror PC, which also implements a third level trigger (TLT). Data passing the FLT, the SLT and the TLT (see section 2.2.2) are sent through the Mirror PC to the central readout computer of the site, called Eye PC. The coincident data from the telescopes of a site are used to build an event by the Eye PC, which also generates a hybrid trigger (T3) for the SD.

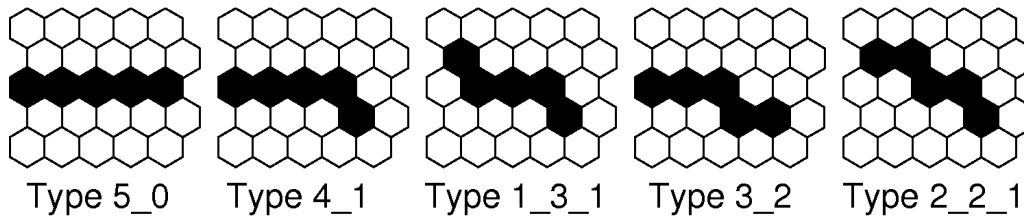


Figure 2.8: Fundamental patterns of the SLT. They are used together with their rotation and reflection. Figure from [39].

2.2.2 The trigger of the FD

The FLT is a pixel trigger implemented in Field Programmable Gate Array (FPGA) firmware. It consists of a threshold cut on the integrated ADC signals of the PMT. The threshold level is adjusted to keep the rate of pixel triggers at around 100 Hz under variable background light conditions, which are monitored by analysing the variances of the ADC values. The pixel triggers generated in the 20 FLT boards corresponding to the 20 columns of the camera are read by a SLT board. The SLT is implemented in FPGA logic and searches for patterns with a length of at least five pixels. The fundamental patterns, used together with their rotation and reflection, are shown in Figure 2.8. In order to take into account pixels below the FLT threshold and defective PMTs, only four triggered pixels out of five are required. This makes the total number of patterns be 108. The pixel triggers of a camera column are read by a pipelined mechanism that searches for the patterns on a submatrix of 22×5 pixels. Two adjacent columns are read every 100 ns. If a pattern is identified while scanning the full camera, data are stored and sent to the TLT. The full scan is carried out in $1 \mu\text{s}$. The TLT is a software trigger whose purpose is to reject the noise events from lightnings, muons impacting on the camera and random triggers that pass the FLT and the SLT. If an event passes the TLT, it is sent to the Eye PC and merged with the coincident events from the other telescopes of the site. If the event satisfies further quality requirements after performing a simple shower reconstruction, the Eye PC sends a T3 trigger to the CDAS. The T3 algorithm calculates a preliminary shower direction and ground impact time using a fast online reconstruction. The T3 trigger is used as an external trigger of the SD for hybrid events with energies below $3 \cdot 10^{18}$ eV at which the SD could not generate an independent trigger.

2.2.3 The calibration of the FD

To properly reconstruct the longitudinal profile of a shower, the ADC counts of each pixel that receives a portion of the signal from a shower need to be converted to a light flux. Therefore, a method to measure the response of each pixel given a certain flux of incident photons from the solid angle covered by that pixel is needed. An absolute end-to-end calibration is provided using a drum shaped light source that measures 2.5

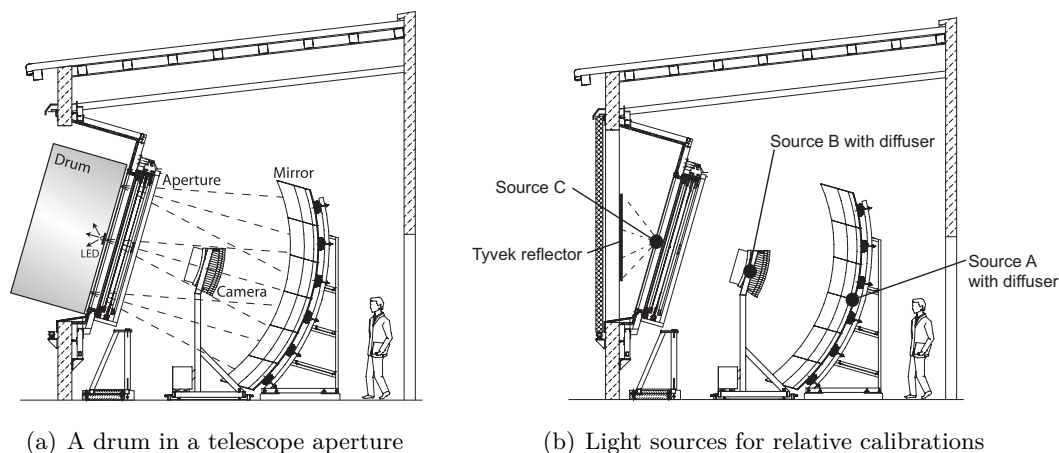
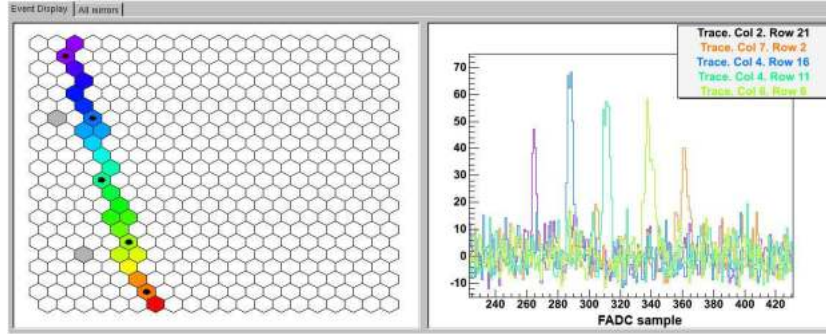


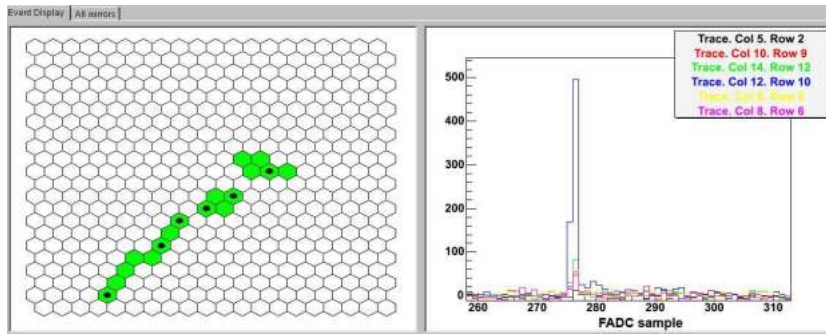
Figure 2.9: Schematic views of a drum mounted in a telescope aperture (a) and positions of light sources for three different relative calibrations (b). Figures from [39].

m in diameter and 1.4 m deep placed at the aperture of the telescope. The effects of diaphragm area projection, optical filter transmittance, mirror reflectivity, pixel light collection efficiency and area, cathode quantum efficiency, PMT gain, preamp and amplifier gains, and digital conversion are taken into account when the end-to-end calibration is performed. The drum light source consists of a pulse UV LED, emitting in a narrow band around 365 nm, that is mounted against the face of a 2.5 cm diameter \times 2.5 cm long Teflon cylinder. The Teflon cylinder is mounted in a reflector cup with a diameter of 15 cm mounted flush to the center of the drum front surface, illuminating the interior and the back surface of the drum. The sides and back surfaces of the drum, together with the reflective cup, are lined with Tyvek, a material diffusively reflective in the UV. The front face of the drum is made of a thick Teflon sheet, which transmits light diffusively. The drum light source intensity, which is measured relative to a NIST calibrated photodiode, is calibrated to a precision better than 4% in a dark room. The knowledge of the pulsed flux of photons emitted by the drum and the corresponding ADC pulse integrals of the camera pixels allows to obtain the absolute calibration constants. A schematic view of a drum mounted in a telescope aperture is shown in Figure 2.9(a).

The long-term variations in the calibration of the telescopes is monitored using an optical system for relative calibration. Three light sources coupled to optical fibers illuminate three different detector components on each telescope. The first light source is a 470 nm LED, whose signals are brought to a Teflon diffuser at the center of the mirror (position A in Figure 2.9(b)). The light of this source is directed towards the camera. The fibers from the second source, a xenon flash lamp, on the other hand, split near the camera and terminate at 1 mm thick Teflon diffusers at the center of two sides of the camera (position B in Figure 2.9(b)), so that the light is directed towards the mirror. The third source is also a xenon flash, whose fibers split terminating at the



(a) Cosmic ray shower as seen on an event display



(b) Background event as seen on an event display

Figure 2.10: An event corresponding to a cosmic ray shower as seen on an event display of the camera is shown in Figure (a). The activated pixels are shown in the left panel, while the response of the selected pixels (marked by black dots) as a function of time is shown in the right panel. The bin size is 100 ns. A background event most likely due to cosmic ray muon interacting with the glass of the PMT is shown in Figure (b). The event is not compatible with a cosmic ray shower because all the activated pixels give a signal in the same time. Figures from [39].

sides of the entrance aperture (position C in Figure 2.9(b)). Reflective Tyvek sheets mounted on the inside of the shutters reflect the light from this source back into the telescopes. The comparison of the measurements from these three light sources allows to identify the changes in the temporal performance of pixels, mirror and aperture components.

2.2.4 The FD event reconstruction

The cosmic ray showers are detected by the FD as a sequence of triggered pixels. As an example, two events corresponding to a cosmic ray shower and to a background event as seen on an event display of the camera are shown in Figure 2.10. The reconstruction of FD events follows two steps: a geometrical reconstruction and a profile reconstruction. The geometrical reconstruction has, in turn, two steps. The first step

by minimizing the quantity:

$$\chi^2 = \sum_i w_i (t_i^{\text{exp}} - t_i^{\text{meas}})^2, \quad (2.9)$$

where t_i^{meas} is the measured time at which the light arrives at the i th pixel.

The reconstruction of an event detected by a single eye (monocular reconstruction) may present problems if the curvature of the function reported in Eq. 2.8 is too small. For these events, which have usually short tracks, there is a degeneracy between R_p and χ_0 that reflects on the determination of the shower parameters. If a particular class of events does not trigger the SD and thus can be reconstructed only with a monocular reconstruction, such as the one described in Chapter 5, the degeneracy can be removed by using the Profile Constrained Geometry Fit reconstruction (see section 5.3), which use an additional requirement on the profile of the energy deposit in the atmosphere. If a detection with the SD is possible, the degeneracy can be resolved by performing a hybrid reconstruction, which combines the timing information from the SD with the one from the FD. The signal from a single SD station is sufficient to perform a hybrid reconstruction. Considering that the duty cycle of the SD is around 100% compared with 12-15% of the FD and that the signal from the FD is used as an SD external trigger for low energy showers that do not trigger the SD (see section 2.2.2), most of the events detected by the FD are hybrid events.

The profile reconstruction is performed by converting the light measured at the aperture as a function of time to an energy deposit as a function of slant depth¹. Since it is important to know the attenuation of the light from the shower to the telescope, the atmosphere is continuously monitored using different facilities (see section 2.2.5). Furthermore, the contributions from the scattered light (direct and scattered Cherenkov light and multiply scattered light) have to be identified and subtracted in order to correctly reconstruct the primary energy. An example of the light measured at the aperture with the reconstructed light contributions and the profile of the energy deposit is shown in Figure 2.12. The profile of the energy deposit is fitted with a Gaisser-Hillas function [43]:

$$\frac{dE}{dX} = \left(\frac{dE}{dX} \right)_{\text{max}} \left(\frac{X - X_0}{X_{\text{max}} - X_0} \right)^{\frac{X_{\text{max}} - X_0}{\lambda}} e^{-\frac{X_{\text{max}} - X}{\lambda}}, \quad (2.11)$$

where dE/dX is the energy deposit at depth X , $(dE/dX)_{\text{max}}$ is the energy deposit at the depth of the shower maximum X_{max} , X_0 and λ are two shape parameters. The

¹The slant depth $X(l)$ at a distance l along the shower axis is defined as:

$$X(l) = \int_l^\infty \rho(z) dl, \quad (2.10)$$

where $\rho(z)$ is the density of the air as a function of the altitude z and the integration is performed along the shower axis from l to infinity. Eq. 2.10 can not be solved analytically for a generic geometry [42], but if the curvature of the Earth is not taken into account, the slant depth at altitude h is given by $X(h) = X_v(h)/\cos\theta$, where θ is the zenith angle and X_v is the vertical depth defined as $X_v(h) = \int_h^\infty \rho(z) dz$.

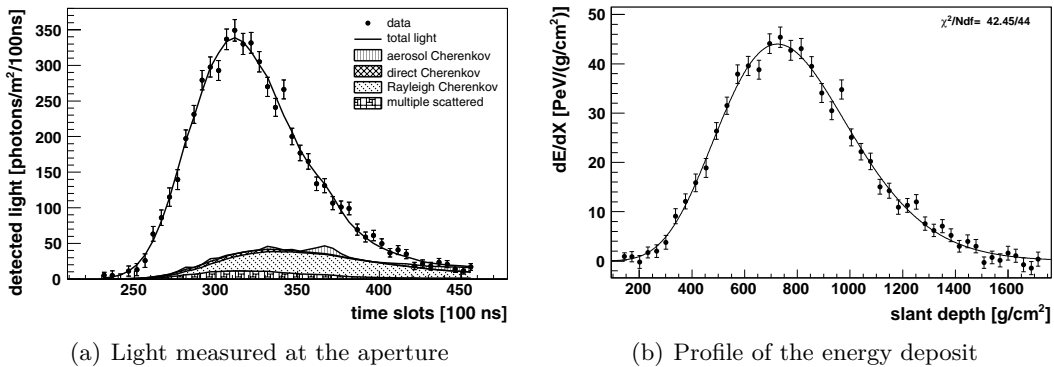


Figure 2.12: Light measured at the aperture as a function of time with the reconstructed light contributions (a) and the the energy deposit as a function of the slant depth (b) obtained from the light at the aperture shown in (a). Figures from [39].

calorimetric energy of the shower is then calculated by integrating the fitted Gaisser-Hillas function. The total energy of the shower is finally estimated by taking into account the corrections for the energy carried away by neutrinos and high energy muons, called “invisible energy”.

2.2.5 The atmospheric monitoring

Since the atmosphere is used as a giant calorimeter, the atmospheric monitoring [44] plays a crucial role in the detection of the air showers. As mentioned in section 2.2.4, the atmospheric conditions need to be known in order to properly reconstruct the air showers detected by the FD. The state variables of the atmosphere, temperature, pressure and humidity, affect the longitudinal development of the shower and the amount of the emitted fluorescence light. Once the fluorescence light is emitted, it propagates towards the FD and it undergoes reduction processes which also have to be taken into account during the reconstruction [45]. These processes are the Rayleigh scattering, the Mie scattering and the obscuration by clouds. The Rayleigh scattering, which occurs when the light is scattered off the molecules of the air whose diameter is much smaller than its wavelength, is analytically obtained from the knowledge of the state variables of the atmosphere. The Mie scattering, on the other hand, which is the scattering of the light off the aerosols (i.e. the suspensions of liquid or solid particles in the air) that have a diameter similar to or larger than its wavelength, can be determined only with dedicated measurements. As regards the obscuration by clouds, the presence of clouds can reduce the fluorescence light from parts of the shower or increase the detected light if the Cherenkov light of a shower is scattered while crossing a cloud layer [46]. For this reason, measurements of cloud cover and cloud height need also to be performed. The atmospheric monitoring plays an important role also during unusual atmospheric conditions, such as the one shown in Figure 2.13, in which the presence of diffuse smoke is visible.

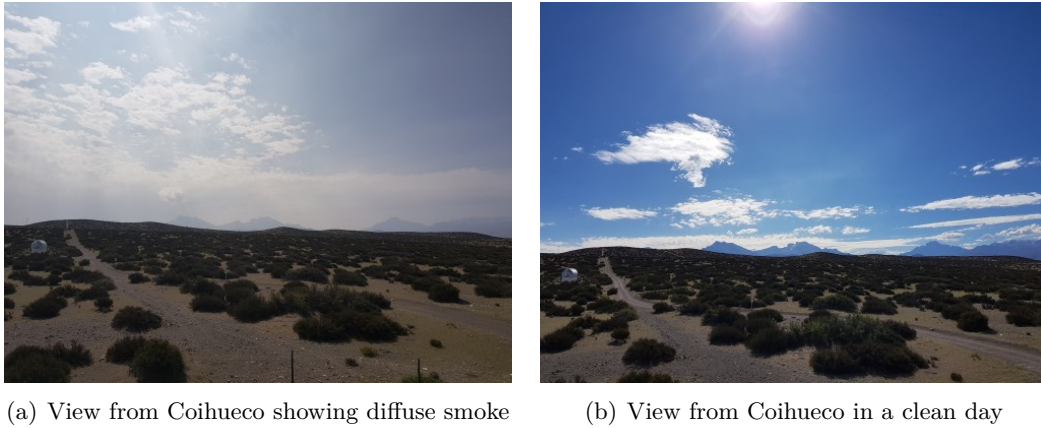


Figure 2.13: View from the top of the Coihueco building as seen in two different periods, showing the importance of a continuous monitoring of the atmosphere. The presence of diffuse smoke is visible in picture (a), which was taken on 18th January 2020. As a reference, the same view as seen in a clean day is shown in picture (b), which was taken on 7th March 2019. On the left side of both pictures the lidar station of the Coihueco site is also visible. Personal photos.

The temperature, the pressure, the humidity and the wind speed are recorded every 5 minutes by ground-based weather stations, located one at each FD site and one at the Central Laser Facility (CLF). The reconstruction of the air showers detected by the FD requires also the knowledge of the state variables of the atmosphere at all the altitudes below 20 km [47, 48]. These quantities were measured by using meteorological radiosondes in the first years of operation of the Pierre Auger Observatory. The outcome of these measurements was then used to calibrate the Global Data Assimilation System (GDAS) [48], which is the input actually used for shower reconstructions. The measurement of the aerosol optical depth profiles [49] used in the reconstruction of the showers detected by the FD is performed by using laser pulses from the CLF and the eXtreme Laser Facility (XLF), each of which is located at almost equal distance from three FD sites 2.1). These two facilities shoot 50 vertical laser beams of wavelength 355 nm every 15 minutes. The scattered light is detected by the FD telescopes and then compared to the one from reference clear nights during which only Rayleigh scattering occurs to obtain the Vertical Aerosol Optical Depth (VAOD). The light profiles of the laser beams allows also to measure the heights of the clouds above the CLF and the XLF. The CLF and XLF have also a steerable system to shoot inclined laser beams. An elastic lidar station is installed at each FD site. The lidars are steerable and are used to measure cloud cover, cloud height and aerosol optical depth. They produce pulsed laser beams with a wavelength of 351 nm at a repetition rate of 333 Hz. The backscattered light is focused by three 80 cm mirrors on as many PMTs. The laser beams are usually shot outside the field of view of the telescopes to avoid interferences with the FD measurements. Information on clouds is provided also by infrared cam-



Figure 2.14: HEAT as seen from the top of the Coihueco building overlooking the SD array (a) and close view of the HEAT telescopes in tilted orientation (b). Personal photos.

eras, located one at each FD site, which detect the infrared light emitted by the clouds in the field of view of the telescopes. A more detailed description of the atmospheric monitoring can be found in [26].

2.3 The enhancements to the Pierre Auger Observatory

To extend the science reach of the Pierre Auger Observatory, new enhancements to its baseline design were proposed. These enhancements include the High Elevation Fluorescence Telescopes (HEAT), the Auger Muon and Infilled Ground Array (AMIGA) and the Auger Engineering Radio Array (AERA).

2.3.1 HEAT

HEAT consists of three additional telescopes located 180 m north-east of the Coihueco site [50]. These telescopes are similar to the FD telescopes described above but can be tilted by 29° . Their field of view covers an angular range between 30° and 58° in elevation. HEAT is shown in Figure 2.14, while a schematic view of one of its telescopes is shown in Figure 2.15. In combination with the infill array, an array of SD stations placed at a distance of 750 m from each other (see Figure 2.1), the HEAT telescopes allow to lower the energy threshold of hybrid data down to 10^{17} eV. HEAT can operate in both horizontal and tilted mode (see Figure 2.15). The horizontal mode is used for service and absolute calibration of the telescopes. When operated in horizontal mode, HEAT has the same field of view of the Coihueco telescopes, and the events detected by both detectors can be used to perform special analyses and test the alignment of the HEAT telescopes. The tilted mode is used for data taking and makes the combination HEAT-Coihueco have a field of view in the elevation range between

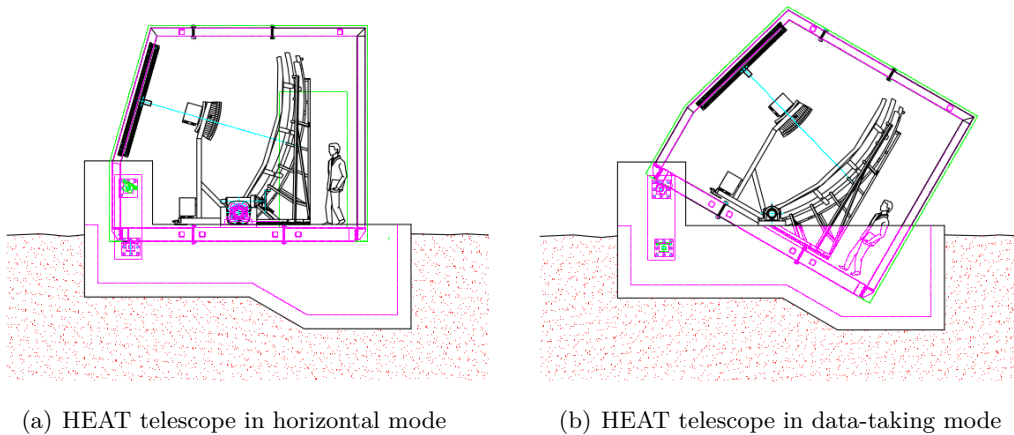


Figure 2.15: Schematic view of a HEAT telescope in horizontal mode, which is used for service and cross calibration, (a) and tilted mode, which is used for data taking (b). Figures from [26].

about 1.5° and 58° . HEAT has been taking data since September 2009.

2.3.2 AMIGA

AMIGA consists of 61 synchronised pairs of SD stations and underground scintillator detectors deployed on a 750 m triangular grid covering an area of 23.5 km^2 (infill array). The underground detectors are buried under 2.3 m of soil, which provides a vertical shielding of 540 g cm^{-2} from the electromagnetic particles of air showers [51]. An underground detector is triggered externally if the corresponding SD station of the infill array is triggered by an air shower. In this way, the particles of air showers are sampled at ground and 2.3 m below the ground. The objective of AMIGA is to extend the energy threshold down to 10^{17} eV and measure the muonic component of air showers. The deployment of the SD stations of the infill array was completed in September 2011, while the so-called Unitary Cell, which is the first prototype hexagon of underground scintillator detectors (see Figure 2.16), has been fully operational since March 2015. The Unitary Cell consists of seven SD stations paired with 30 m^2 underground scintillator detectors (six at each vertex of the hexagon and one at its center), which are segmented in four modules, two 10 m^2 modules and two 5 m^2 modules. Two positions of the hexagon are equipped with an extra 30 m^2 segmented underground scintillator detector (twin detectors) to directly measure the accuracy of the muon counting. Furthermore, one position is equipped with an extra 20 m^2 underground scintillator detector buried at a shallower depth to study the shielding features of the soil. The lower energy events recorded by the infill array are reconstructed using the same methods used for the 1500 m SD array data. The map of the AMIGA infill is shown in Figure 2.16.

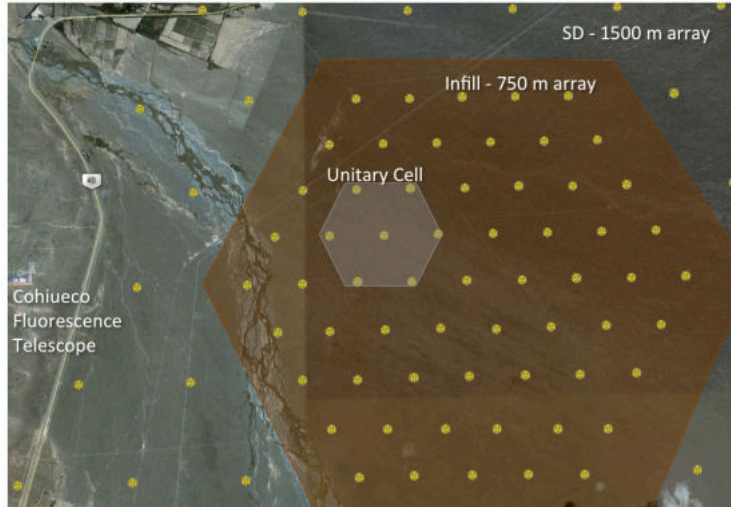


Figure 2.16: Map of the AMIGA infill with the Unitary Cell (shaded area). Figure from [26].

2.3.3 AERA

Electrons and positrons in an air shower produce radio pulses via two main emission processes: the geomagnetic emission [52] and the Askaryan emission [53]. The geomagnetic emission is caused by electrons and positrons that are deflected in opposite directions by the Earth’s magnetic field. Since the number of electrons and positrons changes during the shower development, the drift current induced in the air changes over time producing a radio signal. The Askaryan emission is due to the time variation of the negative net charge excess in the shower front. The charge excess is caused by the annihilation of positrons into photons and the production of further electrons via Compton scattering. The radio signal produced by an air shower can be used to infer the depth of the shower maximum, the arrival direction and the energy of the primary particle. Furthermore, the radio detection techniques have a 100% duty cycle.

AERA measures the radio emission from air showers with energies above 10^{17} eV in the frequency range between 30 and 80 MHz, which is a radio quiet region between the shortwave and FM bands. It is located inside the area of the infill array allowing for a detection of air showers in coincidence with HEAT and AMIGA and cross calibration. The deployment of AERA started in 2010 with 24 stations equipped with logarithmic periodic dipole antennas and connected to a central data acquisition system via a fiber optic link. These stations are placed at a distance of 144 m from each other. In May 2013, 100 additional radio detector stations arranged at a distance of 250 m and 375 m were installed. Contrary to the previous ones, these stations have butterfly antennas and are connected to a central data acquisition system via a wireless communication system. Further 25 butterfly antenna stations were deployed in March

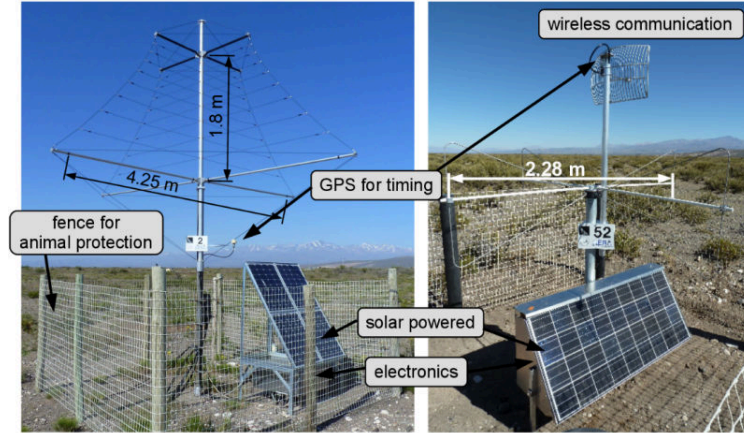


Figure 2.17: An AERA station with a logarithmic periodic dipole antenna (left) and an AERA station with a butterfly antenna (right). Figure from [54].

2015 at a distance of 750 m from each other. AERA actually consists of 153 stations covering an area of 17 m^2 . The two types of stations deployed at AERA are shown in Figure 2.17.

Considering that the radio emission is produced around the depth of the shower maximum, X_{max} can be determined from the shape of the radio signal at the ground, which depends on the distance to the emission region [55]. The arrival direction of the primary particle can be reconstructed from the timing of the signals in the stations using a wavefront model for the radio emission. The energy of the primary particle can be inferred by using the radiation energy as an energy estimator. The radiation energy is calculated by converting the measured electric field strength at the station positions to an energy density. The energy density is interpolated by using a LDF which takes into account the asymmetries due to the combined geomagnetic and Askaryan effect. The radiation energy is then obtained by integrating this LDF [56, 57].

2.4 The upgrade of the Pierre Auger Observatory

The determination of the cosmic ray composition in the energy range in which the flux suppression is observed plays an important role in the identification of the UHECR sources. The duty cycle of the FD does not allow to reach a significant statistics for this energy range, while mass composition analyses performed with the SD are affected by the systematic uncertainties related to the determination of the muonic component of the shower. For this reason, the Pierre Auger Observatory has started a major upgrade, called AugerPrime [58], which is currently under deployment. The main component of the upgrade consists of a plastic scintillator detector, called Surface Scintillator Detector (SSD), installed above each SD station. The different responses of the two detectors to muons and electromagnetic particles allow to better discriminate between the muonic and electromagnetic component of the shower. The SSD consists of two

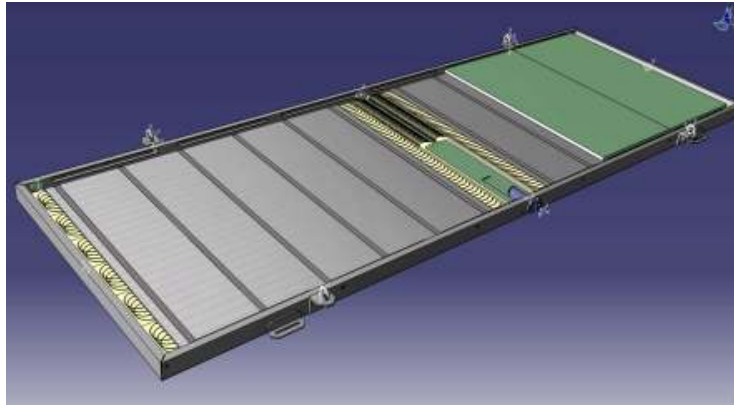


Figure 2.18: The layout of the SSD. The enclosing box, the scintillator bars, the fibers and the PMT are visible. Figure from [59].

modules of 2 m^2 extruded plastic scintillators, each of which is made by 24 extruded polystyrene scintillator bars of 1.6 m length, 1 cm thickness and 5 cm width. The two modules are enclosed in a box of $3.8 \text{ m} \times 1.3 \text{ m}$ and are read out by wavelength-shifting fibers, which are inserted into holes in the bars and are coupled to a single PMT. The fibers follow the grooves of the routers at both ends in a “U” configuration that maximizes the light yield allowing to use a single PMT. The PMT used in the SSD is the Hamamatsu R9420, which has a good quantum efficiency in the wavelength region of interest and a good linearity range. The measurement of the linearity of two Hamamatsu R9420 PMTs used to test the SSD modules assembled at the University of Salento, Lecce (Italy), is reported in Appendix A. The layout of the SSD is shown in Figure 2.18, while a SSD installed above a tank is visible in Figure 2.2(b).

To improve the quality of the data, the calibration, the local trigger, the monitoring and processing capabilities of the SD, each SD station is upgraded with new electronics that processes the signals from both the tank and the SSD. Furthermore, a small PMT (SPMT) dedicated to the readout of large signals is installed in each SD station. More than 40% of the events with an energy above $3 \cdot 10^{19} \text{ eV}$ have saturated signals at least in the SD station closest to the shower core [58]. The addition of the SPMT is expected to reduce the percentage of saturated events at the highest energies to less than 2%.

In addition to the SD upgrade, the FD operation time will be extended into periods with higher night sky background. To operate in these conditions, the gain of the FD PMTs will be lowered, in order to reduce their long-term aging due to the increased exposure to the background light. This will allow to increase the current duty cycle of the FD by about 50% [58].

The upgrade of the Pierre Auger Observatory aims to shed some light on the mass composition of UHECRs and the origin of the flux suppression at the highest energies. This will improve the comprehension of the separation between propagation effects and maximum energy that can be achieved within the cosmic accelerators, allowing to

constrain the astrophysical sources and better estimate the fluxes of ultra high energy neutrinos and photons. The upgrade will allow also to search for a proton contribution at the highest energies, providing useful information for proton astronomy and helping to predict the associated secondary fluxes of neutrinos and photons. Furthermore, the improvement in the determination of the mass composition will allow to study the hadronic interactions at energies much higher than those attainable by colliders.

Chapter 3

Multi-Messenger astrophysics with the Pierre Auger Observatory

In addition to UHECRs, the Pierre Auger Observatory is sensitive also to neutral particles, such as photons, neutrinos and neutrons. Furthermore, the design of the FD allows to perform searches for upward-going showers, which are a possible interpretation of the recent events reported by the ANtarctic Impulsive Transient Antenna (ANITA) Collaboration [60, 61]. The sensitivity to these other classes of events allows the Pierre Auger Observatory to take active part to Multi-Messenger searches in collaboration with other observatories.

3.1 Searches for different types of cosmic messengers

The complementary information from cosmic rays, neutrinos, high energy gamma rays, gravitational waves and neutrons provides insights into the properties of the corresponding astrophysical sources. After the detection of the first gravitational wave [62], the Multi-Messenger astronomy underwent a significant boost. The later discovery of gravitational waves from a binary neutron star merger [63] was coupled with a combined search for high energy gamma rays [64] and neutrinos [65] to which the Pierre Auger Observatory took part. The importance of Multi-Messenger searches in the comprehension of astrophysical sources became evident also with the detection of a high energy neutrino from the blazar TXS-0506+056 in coincidence with a flare of high energy gamma rays in 2017 [66]. The analysis of archival data allowed to identify an enhanced neutrino emission from this source between 2014 and 2015 [67].

Multi-Messenger analyses are currently on-going within the Pierre Auger Collaboration. Searches for photons and neutrinos can be performed by exploiting the design of the Pierre Auger Observatory, which allows to use the different properties of cosmic ray, neutrino and photon induced showers to discriminate between them.

3.1.1 Search for diffuse photons

Ultra high energy photons can originate from the decay of neutral pions produced in the interaction of protons with the CMB photons (see Eq. 1.23) and from the interaction of protons within the sources or their local environment. In both cases, their average energy is approximately 10% of that of the interacting proton [68]. In addition to this “bottom-up” scenario, a large flux of ultra high energy photons is expected in “top-down” models, which assume that UHECRs are the decay products of Super Heavy Dark Matter (SHDM) particles, topological defects (TD) or Z^0 bosons produced in the interaction of high energy neutrinos with the relic neutrino background (Z-burst) [69, 70, 71]. Limits on the flux of ultra high energy photons can provide a discrimination between these two different scenarios.

During their propagation, photons interact with the extragalactic background light (EBL) and generate EM cascades. Considering that the attenuation length of EeV photons is about 4.5 Mpc [72], the maximum distance from which photons at those energies can be detected is limited. The secondary $e^+ e^-$ pairs interact with background photons via inverse Compton scattering. The result is an EM cascade ending at GeV-TeV energies. The corresponding diffuse fluxes can be measured by using detectors sensitive to this energy range.

Air showers induced by ultra high energy photons can be identified by relying on their reduced muon content and deeper depth of the shower maximum X_{\max} . If compared to simulated proton showers, simulated photon showers have an average X_{\max} that differs by about 200 g cm^{-2} in the EeV energy range [68]. At energies above 10 EeV this difference becomes larger because of the Landau-Pomeranchuk-Migdal (LPM) effect [73, 74]. Furthermore, photons with an energy above 50 EeV can convert in the geomagnetic field [75, 76, 77] and produce a pre-shower of low energy electromagnetic particles, whose X_{\max} is smaller than that of non-converted showers. This results in a reduced separation between the average X_{\max} for protons and photons. The X_{\max} separation allows to use the FD to discriminate between photon and hadron showers. The reduced muon content, on the other hand, makes the LDF for photons steeper than that for hadrons, making photon showers detectable also with the SD. The number of triggered stations N_{stat} is typically smaller for photon showers [78]. Furthermore, the rise of the signal in the SD stations for photon showers is slower than that for hadron showers.

For energies above 10 EeV, photon showers are searched for with the SD in the zenith angle range $30^\circ < \theta < 60^\circ$. The minimum zenith angle is chosen to be 30° in order to ensure that most of the photon showers with these energies are fully developed. Data taken from 1 January 2004 to 30 June 2018 are used. The optimal separation between hadron and photon showers is estimated by performing a Monte Carlo (MC) simulation of photon showers [79]. Two discriminating observables are used. The first one is based on the steeper LDF of photon showers:

$$L_{\text{LDF}} = \log_{10} \left(\frac{1}{N} \sum_{i=1}^N \frac{S_i}{S_{\text{LDF}}(R_i)} \right), \quad (3.1)$$

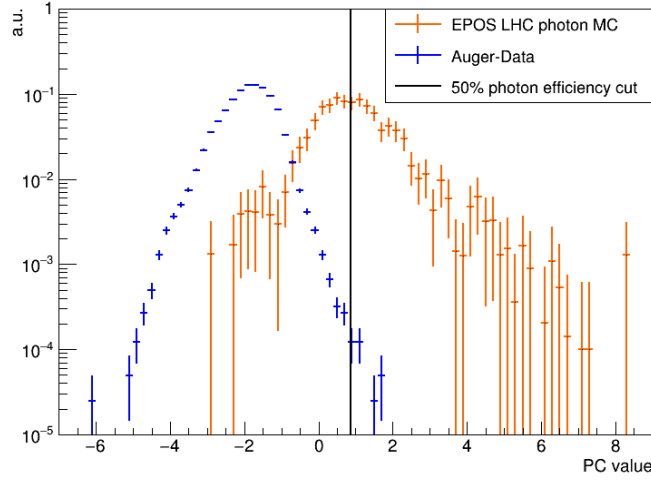


Figure 3.1: Distribution of the PCA variable for the data (blue) and the MC photons (orange). The cut at 50% efficiency on the MC photon distribution is indicated by the black line. 11 data events are above the cut value. Figure from [79].

where S_i is the signal of the i th station, $S_{\text{LDF}}(R_i)$ is the expected signal of the i th station according to the LDF fit at the distance R_i from the shower axis and N is the number of SD stations. The sum is performed only on SD stations with $R_i > 1000$ m. A $L_{\text{LDF}} < 0$ is expected for photon showers, because of their smaller signal at larger distances from the shower axis.

The second discriminating observable is based on the electromagnetic signal of the SD stations, which is delayed compared to that of muons. The risetime, which is defined as the time a SD station takes to increase from 10% to 50% of its total signal, is used to define the observable Δ :

$$\Delta = \frac{1}{N} \sum_{i=1}^N \frac{t_{1/2}^i - t_{1/2}^{\text{bench}}}{\sigma_{t_{1/2}}^i}, \quad (3.2)$$

where $t_{1/2}^i$ is the risetime of the i th station corrected in order to take into account its dependence on the zenith angle and the distance of the shower axis, $t_{1/2}^{\text{bench}}$ is the expected average risetime, called benchmark, $\sigma_{t_{1/2}}^i$ is the risetime uncertainty and N is the number of SD stations. In this case, the sum is performed only on SD stations with a signal larger than 6 VEM and a distance from the shower axis $600 \text{ m} < R_i < 2000$ m. The two discriminating observables are used to perform a Principal Component Analysis (PCA) [79]. The cut on the resulting PCA variable is set in order to have a 50% efficiency on the photon signal [80]. The distributions of the PCA variable for the data and the MC photons is shown in Figure 3.1. After the application of the selection cut 11 data events are left. Since the background hypothesis could not be excluded for these events [79], an upper limit on the photon flux at 95% confidence level was derived (see Figure 3.3).

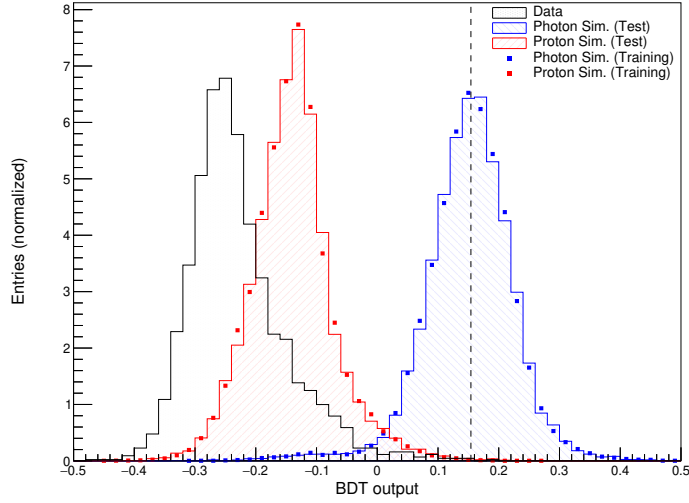


Figure 3.2: BDT output variable distribution for the simulated photon signal (blue), the simulated proton background (red), and the data-set (black). Both the training and the test samples are shown for simulations. The dashed line represents the cut at 50% efficiency on the photon distribution. Figure from [79].

For energies below 10 EeV, the smaller number of SD stations with a signal does not allow to discriminate between photon and hadron showers. However, the X_{\max} measured by the FD can be used as a discriminating observable because of the increased statistics of the events. The zenith angle range considered for these energies is $0^\circ < \theta < 60^\circ$. For hybrid measurements, the discrimination is performed by using X_{\max} , N_{stat} and S_b [81], which is defined as:

$$S_b = \sum_i^N S_i \left(\frac{R_i}{R_0} \right)^b, \quad (3.3)$$

where S_i is the signal of the i th station, R_i is the distance of the i th station from the shower axis, $R_0 = 1000$ m is a reference distance and $b = 4$ is an optimized constant which provides the best discrimination between photon and hadron showers. Simulations of photons and protons are used respectively as signal and background to train a Boosted Decision Tree (BDT) which takes into account also the energy and zenith angle dependence of the discriminating observables. A selection cut on the BDT output variable is defined at 50% efficiency on the photon distribution.

The search for photon showers can be extended below 1 EeV by using the data from the infill array and the measurement of X_{\max} from HEAT. The data used for this analysis are those from 1 June 2010 to 31 December 2015. The distribution of the BDT output variable for data, simulated signal and simulated background is shown in Figure 3.2. The distribution for data differs from that for simulated protons following the experimental indications of a mass composition changing from light to heavy in the EeV range [82] and the observation of a muon deficit in simulations with respect to

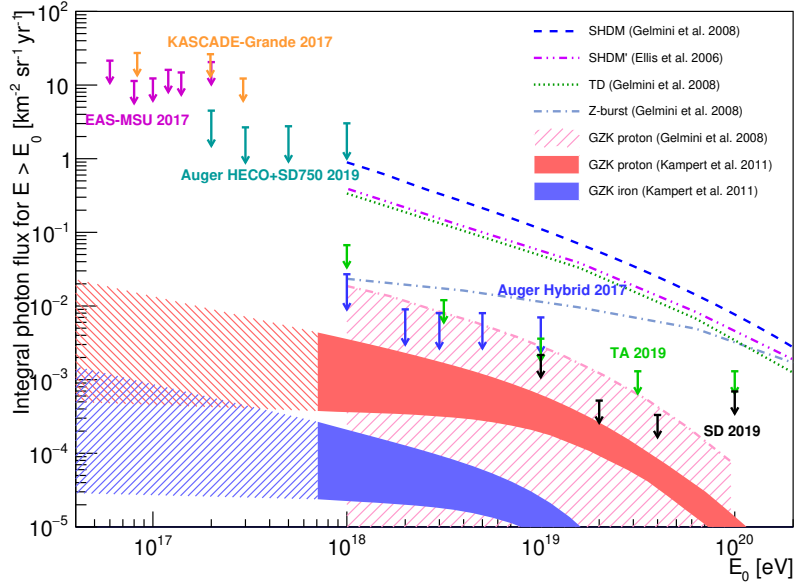


Figure 3.3: Upper limits on the photon flux at 95% confidence level obtained with the Pierre Auger Observatory. Predictions from models [87, 88, 89] and other experimental results at 95% (TA [90]) or 90% (KASCADE-Grande [91], EAS-MSU [92]) confidence level are also shown. Figure from [79].

data [83, 84]. Only one event is observed above the cut value. This number is consistent with the number of events expected from background, therefore an upper limit on the integral photon flux at 95% confidence level for the energy thresholds 0.2, 0.3, 0.5 and 1 EeV was derived (see Figure 3.3).

The upper limit on the integral photon flux at 95% confidence level is calculated as [85]:

$$\Phi_{\text{UL}}^{0.95}(E_\gamma > E_0) = \frac{N_\gamma^{0.95}(E_\gamma > E_0)}{\langle \varepsilon_\gamma \rangle}, \quad (3.4)$$

where $N_\gamma^{0.95}$ is the Feldman-Cousins upper limit [86] at 95% confidence level and $\langle \varepsilon_\gamma \rangle$ is the weighted average exposure for $E_\gamma > E_0$ under the assumption of a E_γ^{-2} power law spectrum. The weighted average exposure is calculated as:

$$\langle \varepsilon_\gamma \rangle = \frac{1}{c_E} \int_{E_\gamma > E_0} \int_T \int_S \int_\Omega E_\gamma^{-2} \epsilon(E_\gamma, t, \theta, \phi, x, y) dS dt dE_\gamma d\Omega, \quad (3.5)$$

where $c_E = \int_{E_\gamma > E_0} E_\gamma^{-2} dE_\gamma$, $\epsilon(E_\gamma, t, \theta, \phi, x, y)$ is the detection efficiency for photons as a function of energy E_γ , time t , zenith angle θ , azimuth angle ϕ and position (x, y) of the impact point at ground, S is the generation area enclosing the SD used in simulations and Ω is the solid angle.

The upper limits on the photon flux at 95% confidence level obtained with the Pierre Auger Observatory are shown in Figure 3.3.

3.1.2 Search for photons from point-like sources

In addition to the search for diffuse photons, the Pierre Auger Collaboration performs also searches for ultra high energy photons from point-like sources. As mentioned in section 3.1.1, the energy of the interacting protons is typically one order of magnitude higher than that of the resulting photons. If protons interact within a source or its local environment, an accumulation of photon showers is expected from the direction corresponding to that source. TeV photon sources [93, 94] should produce EeV photons detectable by the Pierre Auger Observatory if their energy spectra are assumed to extend to EeV energies. Furthermore, a source that produce particle fluxes with a E^{-2} energy spectrum injects equal energy into each decade, therefore a energy flux of $1 \text{ eV cm}^{-2} \text{ s}^{-1}$ in the TeV decade, as measured in different sources of our galaxy, would result in the same energy flux in the EeV decade if the propagation energy losses are negligible [95]. The TeV photon spectrum without a cutoff or a spectral break measured by the H.E.S.S. Collaboration in the Galactic center region is an indication of the presence of a PeV accelerator, called “PeVatron”, in the Galactic center [96]. This makes the search for photons from the Galactic center region of particular interest.

To avoid large statistical penalties, the search for photons is performed considering twelve target sets, each consisting of a class of possible sources of ultra high energy photons [95]. One of the classes is precisely the Galactic center. Since the signal from more than one source should be more significant than that from a single source, the possible sources of photons in each target set are combined in a “stacked analysis”. This analysis is performed by using the hybrid events in the energy range between $10^{17.3} \text{ eV}$ and $10^{18.5} \text{ eV}$ with a zenith angle smaller than 60° collected from 1 January 2005 to 31 December 2013 [95]. The targets considered in this search are those within the maximum distance given by the attenuation length of the photons at the energies of interest. Similarly to the search for diffuse photons described in section 3.1.1, the discrimination between hadron and photon showers is provided by a selection cut defined using the BDT method. The selection cut on the BDT output variable for a given source direction i depends on the number of isotropic events expected without the photon flux from that direction. This number is given by the average number obtained from 5×10^3 simulated data sets, whose number of events is equal to that of the actual data set. The arrival directions and arrival times are assigned randomly from the measured distributions. For each target direction a top-hat counting region of 1° is used [97]. Sources within a given target set are weighted according to their electromagnetic flux and their exposure to the Pierre Auger Observatory. Weights are normalized in order to sum to 1 in each target set. Given a set with N targets, any target i is assigned with a p-value p_i , which is defined as the Poisson probability of having a number of events equal to or greater than the one actually measured, using the average number from the simulated data sets as number of background events. The p-values from the different targets are then used to obtain the combined p-value for both unweighted and weighted target sets. For an unweighted set of N targets, the combined p-value P is given by the fraction of simulations that have a product $\prod_{i=1}^N p_i$ equal to or less than the one obtained from measured data. If each target i in

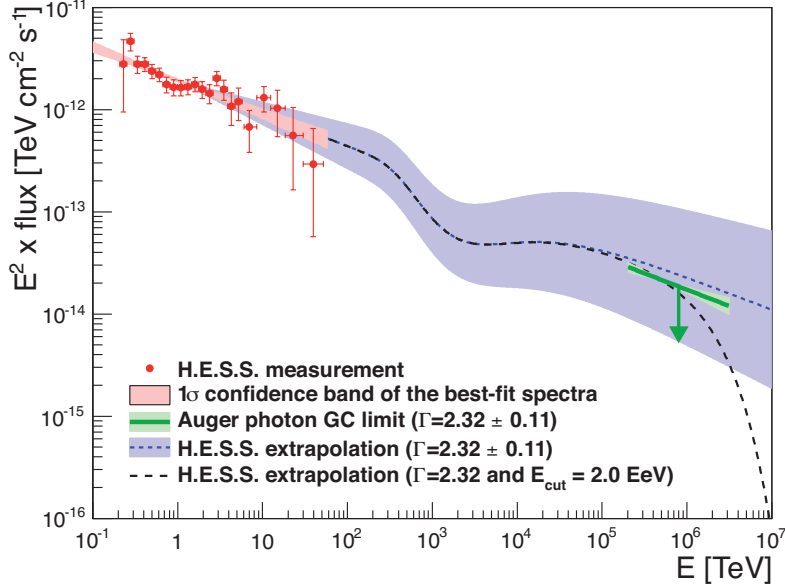


Figure 3.4: Photon energy spectrum from the region of the Galactic center as measured by the H.E.S.S. Collaboration [96] (red points) together with the extrapolations in the EeV range (dashed lines) and the Auger upper limit (green line). The green and blue bands are obtained by varying the spectral index by ± 0.11 according to the systematics of the H.E.S.S. measurement. The dashed black line represents the extrapolation obtained by assuming an exponential cutoff with $E_{\text{cut}} = 2.0$ EeV, which is the upper limit of the cutoff energy derived from the upper limit on the flux. Figure from [95].

a set of N targets has a weight w_i , the combined p-value P_w is given by the fraction of simulations having a weighted product $\prod_{i=1}^N p_i^{w_i}$ equal to or less than the one from measured data. In the weighted case, the weights w_i can be interpreted as the number of times a target i is counted with respect to other targets.

No evidence of a statistical significance larger than 3σ was found, therefore an upper limit on the photon flux from the target with the smallest p-value in each target set was derived assuming a power law spectrum of E^{-2} [95]. The upper limit on the photon flux is computed by dividing the Zech upper limit [98] at 95% confidence level on the number of photons by the directional exposure and by the expected signal fraction in the top-hat search region. The directional exposure as a function of the equatorial coordinates δ (declination) and α (right ascension) used in the calculation of the upper limit is given by [97]:

$$\varepsilon_\beta(\delta, \alpha) = \varepsilon(\delta, \alpha) \cdot \epsilon_\gamma^\beta, \quad (3.6)$$

where $\varepsilon(\delta, \alpha)$ is the exposure before applying the selection cut on the BDT output variable β and ϵ_γ^β is the photon efficiency when applying the cut on β . The exposure $\varepsilon(\delta, \alpha)$ is calculated in a similar way as in section 3.1.1 (see Eq. 3.5), with the exception

of the integration over the solid angle. Focusing on the region of the Galactic center and using a spectral index of 2.32, which is the same as measured by the H.E.S.S. Collaboration [96], the upper limit $J_{\text{UL}} = 0.034 \text{ km}^{-2} \text{ yr}^{-1}$ was derived. As shown in Figure 3.4, the derived upper limit constrains the allowed parameter space for the photon flux at EeV energies.

The non-observation of candidate events from any of the considered targets can be an indication of the extragalactic origin of EeV protons. However, EeV photons could originate within our galaxy from sources that produce fluxes not pointing to the Earth or from transient sources, since the upper limits are calculated by averaging on time. The results could be also explained with a larger escape probability for EeV protons with respect to those that produce TeV photons.

3.1.3 Photon follow-up of gravitational wave events with the SD

Among the Multi-Messenger activities of the Pierre Auger Collaboration there are also the follow-up searches of gravitational waves from the merging of binary systems detected by the LIGO/Virgo Collaboration. The memorandum of understanding signed by the Pierre Auger Collaboration and the LIGO/Virgo Collaboration allowed the Pierre Auger Collaboration to receive alerts on gravitational wave events from the LIGO/Virgo Collaboration. Recently, a follow-up of gravitational wave events has been performed within the Pierre Auger Collaboration by searching for photons with energies above 10 EeV in temporal coincidence with the gravitational wave events observed by the LIGO/Virgo Collaboration. Photon showers are searched for with the SD by using the standard photon search described in section 3.1.1 in both the time window between 500 s before and after the merger and the 24-hour period after the merger, which are the same time windows used in the neutrino follow-up of gravitational wave events (see section 3.1.6). Close and well localized gravitational wave sources are selected to reduce background and account for the attenuation length of photons. The LIGO/Virgo Collaboration provides the localization of a gravitational wave source in terms of a probability sky map. To have a good compromise between the expected background and the confidence level of the source localization, the photon follow-up is performed considering the 50% confidence level region of the convolution between the probability sky map from LIGO/Virgo and the directional resolution of the SD for photon showers [99]. Among the selected gravitational wave sources, only four are found to have some overlap with the SD field of view during the 1 day period. These sources consist of a binary neutron star merger (GW170817 [63]), two binary black hole mergers (GW170818 [100], GW190701_203306 [101]), and black hole-neutron star merger candidate (GW190814 [102]). The selection criteria used in this analysis are described in [99]. No candidate photon showers were found in coincidence with these events. Under the assumption of a E_{γ}^{-2} energy spectrum, a preliminary upper limit on the photon spectral fluence at 90% confidence level was set for each source using the Feldman-Cousins approach [86] and the exposure to photons from transient sources [99]. The exposure is calculated taking into account the fraction of observation time in which the zenith angle of the source, which is a function of the sidereal time, is between

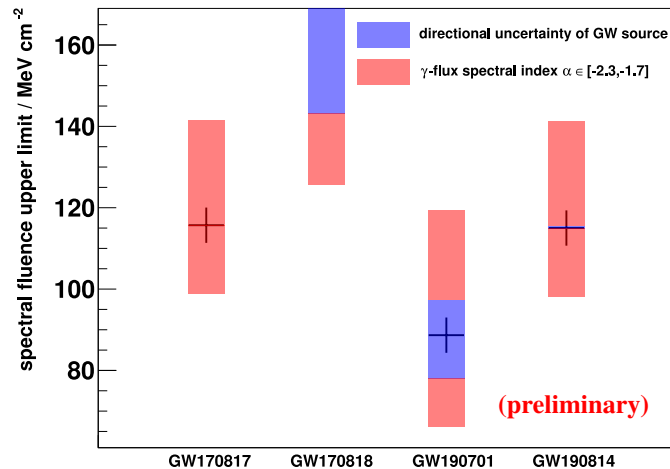


Figure 3.5: Preliminary upper limits at 90% confidence level on the spectral fluence for the four gravitational wave sources reported in the text. The uncertainties due to the limited sky localization of the sources (blue bars) and the variation of the spectral index α in the range $[-2.3, -1.7]$ (red bars) are also shown. The central value of the upper limit for GW170818 is not shown because its sky localization is close to the edge of the field of view. Figure from [99].

30° and 60° [99]. The preliminary upper limits on the photon spectral fluence for the four sources considered in this analysis are shown in Figure 3.5.

3.1.4 Search for diffuse neutrinos with the SD

Similarly to photons, ultra high energy neutrinos can arise from the interaction of protons within the sources, from the decay of charged pions produced in the interaction of protons with the CMB photons and from the interactions of protons with matter. Neutrinos can travel long distances without being absorbed, pointing directly to their sources and providing useful information about extragalactic sources that accelerate UHECRs. Since neutrinos have a low interaction probability, they have to interact with a large amount of matter in order to be detected. Ultra high energy neutrinos are searched for by looking at inclined downward-going showers or nearly horizontal upward-going showers. Hadron showers with a zenith angle $\theta > 60^\circ$ traverse large atmospheric depths, resulting in an almost complete absorption of their electromagnetic component. As a consequence, the SD stations are reached mainly by muons. Neutrinos, on the other hand, can interact deep in the atmosphere and produce showers with a large concentration of electrons and photons at ground. The resulting broader signal in the SD stations can be discriminated from that produced by hadron showers. Furthermore, tau neutrinos can interact in the Earth producing tau leptons that in turn decay and produce upward-going showers. The maximum exit probability is expected for nearly horizontal directions for neutrino energies above 100 PeV [103]. Again, the

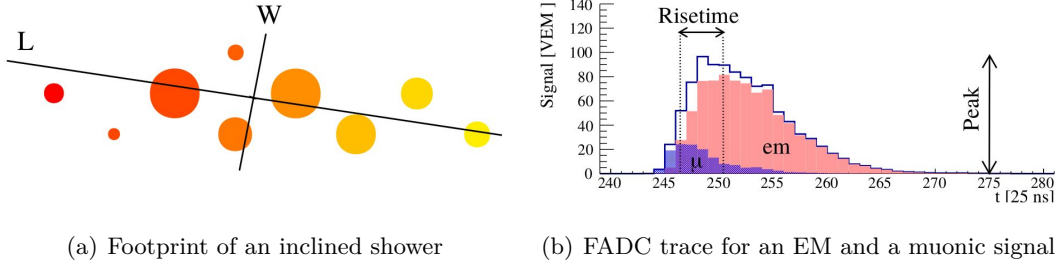


Figure 3.6: A footprint of an inclined shower on SD stations (a) and the FADC trace in a SD station for a dominant electromagnetic signal with its electromagnetic and muonic components (b). Following the same convention as Figure 2.5(a), the different colors in Figure (a) refer to the time arrival of the shower front (signal arriving first are marked with yellow, signals arriving last with red), while the size of the markers is proportional to the logarithm of the signal. The AoP ratio of a dominant muonic signal is larger than that of a dominant electromagnetic signal, as clearly visible in Figure (b). Figures from [105].

broader signal in the SD stations due to the dominant presence of electrons and photons at ground can be used to identify the events from these so-called Earth-skimming neutrinos. The searches for inclined downward-going showers and nearly horizontal upward-going showers are performed in the zenith angle ranges $[60, 90]^\circ$ and $[90, 95]^\circ$, respectively. The zenith angle range for inclined downward-going showers is further divided in two sub-ranges, $[60, 75]^\circ$ and $[75, 90]^\circ$. Nearly horizontal upward-going showers are searched for by scanning all the triggered events, while inclined downward-going showers are required to have a minimum of four triggered stations in order to reduce background. Inclined events can be selected by using the footprints of the showers on SD stations: the ratio L/W between the length L along the shower axis and the width W perpendicular to it is close to 1 for vertical showers and progressively increases with the zenith angle. Also the average apparent speed $\langle V \rangle$ of the trigger between pairs of SD stations along the major axis of the footprint can be used to select inclined events. Vertical showers have a $\langle V \rangle$ that is greater than the speed of light because the SD stations are triggered at almost the same time, while for inclined showers $\langle V \rangle$ is around the speed of light. Furthermore, $\text{RMS}(V)$ is small. The requirements on these parameters, which are used to select inclined events, differs depending on the zenith angle range [104]. The reconstructed zenith angle is used only in the search for inclined downward-going showers. To select showers that develop deep in the atmosphere the Area-over-Peak ratio (AoP) is used. The AoP, which is defined as the ratio between the integral of the FADC trace and its peak value, normalized to the average signal produced by a single muon, allows to select showers that produce broad signals in the SD stations i.e. signals with a dominant electromagnetic component and to reject background hadron showers. A footprint from an inclined shower and the FADC trace of a signal with a dominant electromagnetic component are shown in Figure 3.6.

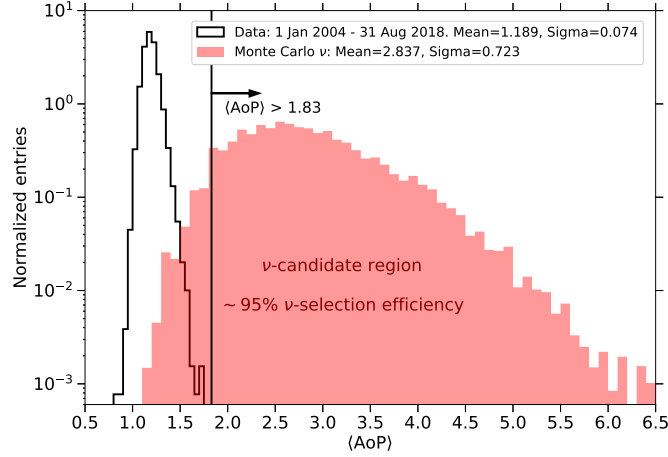


Figure 3.7: Distribution of $\langle \text{AoP} \rangle$ for the data in the whole period considered in the analysis (black histogram) and the simulated Earth-skimming tau neutrinos events (red shaded histogram). The $\langle \text{AoP} \rangle$ optimized cut value is represented by the black line. Figure from [106].

The selection criteria used to discriminate between neutrino and hadron showers are optimized by performing Monte Carlo simulations of ultra high energy neutrinos [104]. Both inclined downward-going showers and nearly horizontal upward-going showers are searched for by defining a single discriminating variable, whose distribution is studied for both neutrino simulations and a fraction of $\sim 15\%$ of the data assumed to be background hadron showers [106]. The cut on this variable is set in order to have less than 1 hadron shower in 50 years (for nearly horizontal upward-going showers and inclined downward-going showers with a zenith angle in the range $[75, 90]^\circ$) or 20 years (for downward-going showers with a zenith angle in the range $[60, 75]^\circ$) according to the extrapolation from an exponential fit performed on the background distribution [104]. Once the selection procedure is defined, the remaining data are unblinded to search for neutrino candidates. This analysis is performed by using data from 1 January 2004 to 31 August 2018.

For nearly horizontal upward-going showers, the selection procedure changes according to the data taking period. For data collected prior to 31 May 2010, the discriminating variable is the fraction of SD stations having ToT trigger and $\text{AoP} > 1.4$. This fraction is required to be larger than 60% of the triggered stations. For data beyond 1 June 2010, the discriminating variable is $\langle \text{AoP} \rangle$, which is the average value of AoP over all the triggered SD stations. The optimized cut value for this variable is $\langle \text{AoP} \rangle = 1.83$. This last procedure is not applied to data before that one because they were already unblinded under older cuts. The distribution of $\langle \text{AoP} \rangle$ for the data in the whole period from 1 January 2004 to 31 August 2018 and the Earth-skimming tau neutrino simulations is shown in Figure 3.7. No candidate events were found [106].

For inclined downward-going showers, the selection procedure is optimized by us-

ing the multivariate Fisher discriminant method [107]. The observables used in this method are obtained from the AoP values of the single SD stations. In the zenith angle range $[75, 90]^\circ$ the selection procedure is further optimized by dividing the events in three sub-samples depending on the number of triggered SD stations, while events in the zenith angle range $[60, 75]^\circ$ are divided in five sub-samples according to the reconstructed zenith angle. A different Fisher variable is defined in each sub-sample. For events in the zenith angle range $[75, 90]^\circ$, the Fisher variables are obtained from ten observables that exploit the lower attenuation of the electromagnetic component of the shower in the SD stations triggered first with respect to those triggered last. The distribution of the Fisher variable for data and simulations belonging to the sub-sample with a number of triggered stations between 7 and 11 is shown in Figure 3.8(a). For events in the zenith angle range $[60, 75]^\circ$, the Fisher variables are constructed from the AoP values of the SD stations closest to the core, which are shown by Monte Carlo simulations to have the highest discriminating power [106]. Furthermore, in this zenith angle range 75% of the triggered SD stations is required to have ToT trigger. The distribution of the Fisher variable for data and simulations in the sub-sample with a reconstructed zenith angle in the range $(58.5, 76.5]^\circ$ is shown in Figure 3.8(b). The upper bound of this range exceeds 75° to take into account the angular resolution. No neutrino candidates were found in any of the three plus five sub-samples.

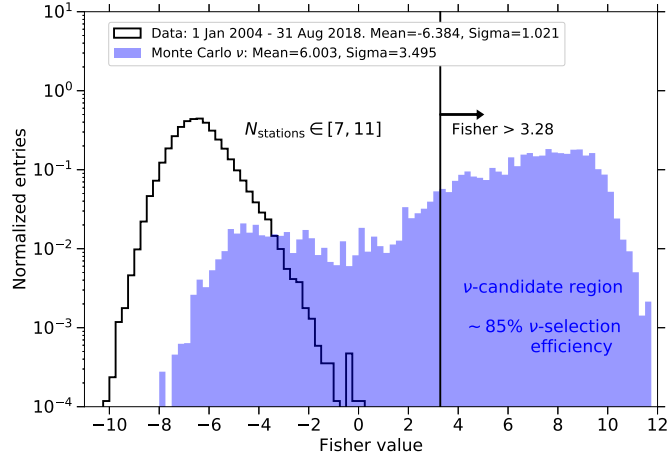
Since no candidate events were found, an upper limit on the diffuse flux of ultra high energy neutrinos can be derived. Therefore, the SD exposure to neutrino showers is needed. For inclined downward-going neutrinos, the exposure for a specific neutrino flavor $i = e, \mu, \tau$ and interaction channel $c = \text{Neutral Current (NC), Charged Current (CC)}$ is calculated as [104, 106, 108]:

$$\varepsilon_{\nu_i, c}(E_\nu) = \int_S \int_\theta \int_\phi \int_X \int_t \cos \theta \sin \theta \epsilon_{\nu_i, c}(E_\nu, \theta, \phi, x, y, X, t) \sigma_\nu^c m_p^{-1} dS d\theta d\phi dX dt, \quad (3.7)$$

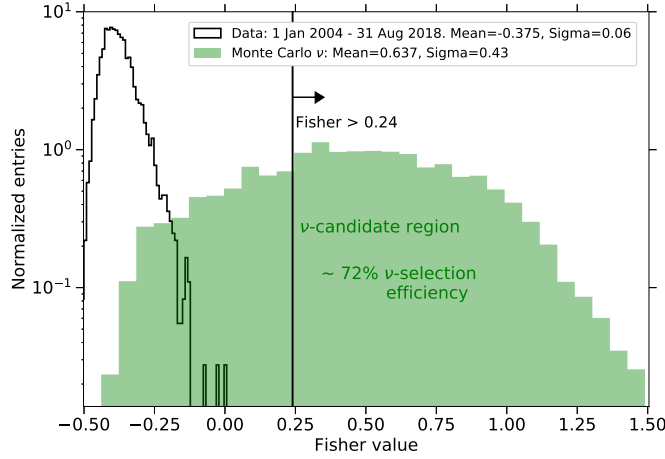
where S is the area of the SD, m_p is the mass of a proton, σ_ν^c is the neutrino-nucleon cross section and $\epsilon_{\nu_i, c}(E_\nu, \theta, \phi, x, y, X, t)$ is the detection efficiency for neutrinos of flavor i and interaction channel c as a function of energy E_ν , zenith angle θ , azimuth angle ϕ , position (x, y) of the shower core, depth in the atmosphere X at which the neutrino is forced to interact in the simulations and time t . The product $\sigma_\nu^c m_p^{-1} dX$ represents the probability of neutrino-nucleon interactions along a depth dX . The factor $\cos \theta$ comes from the projection of the area of the SD onto the direction perpendicular to the arrival direction of the neutrino. The exposure for all flavor and interaction channels can be obtained by summing the individual contributions after weighting them with the corresponding flavor ratio. Assuming a flavor ratio of 1:1:1, the weight for each contribution is 1.

For Earth-skimming tau neutrinos, the exposure is given by:

$$\varepsilon_{\text{ES}}(E_\nu) = \int_S \int_\theta \int_\phi \int_{E_\tau} \int_{h_{\text{dec}}} \int_t |\cos \theta| \sin \theta p_{\text{exit}} p_{\text{dec}} \cdot \epsilon_{\text{ES}}(E_\tau, \theta, \phi, x, y, h_{\text{dec}}, t) dS d\theta d\phi dE_\tau dh_{\text{dec}} dt, \quad (3.8)$$



(a) Sub-sample with $7 \leq N_{\text{stat}} \leq 11$



(b) Sub-sample with $58.5^\circ < \theta_{\text{rec}} \leq 76.5^\circ$

Figure 3.8: Distribution of the Fisher variable for the data in the period from 1 January 2004 to 31 August 2018 (black histograms) and the simulated downward-going neutrino events (blue shaded histogram in Figure (a) and green shaded histogram in Figure (b)). The optimized cut value on the Fisher variable is represented by the black line. Figure (a) refers to the sub-sample of nearly horizontal upward-going showers with a number of triggered stations between 7 and 11, while Figure (b) refers to the sub-sample of inclined downward-going showers with a reconstructed zenith angle θ_{rec} in the range $(58.5, 76.5]^\circ$. Figures from [106].

where S is the area of the SD, $p_{\text{exit}} = dp_{\text{exit}}/dE_\tau$ is the differential probability for a tau lepton to exit from the Earth with energy E_τ , $p_{\text{dec}} = dp_{\text{dec}}/dh_{\text{dec}}$ is the differential probability for a tau lepton to decay at an altitude h_{dec} and $\epsilon_{\text{ES}}(E_\tau, \theta, \phi, x, y, h_{\text{dec}}, t)$ is the detection efficiency averaged over the tau lepton decay channels as a function of

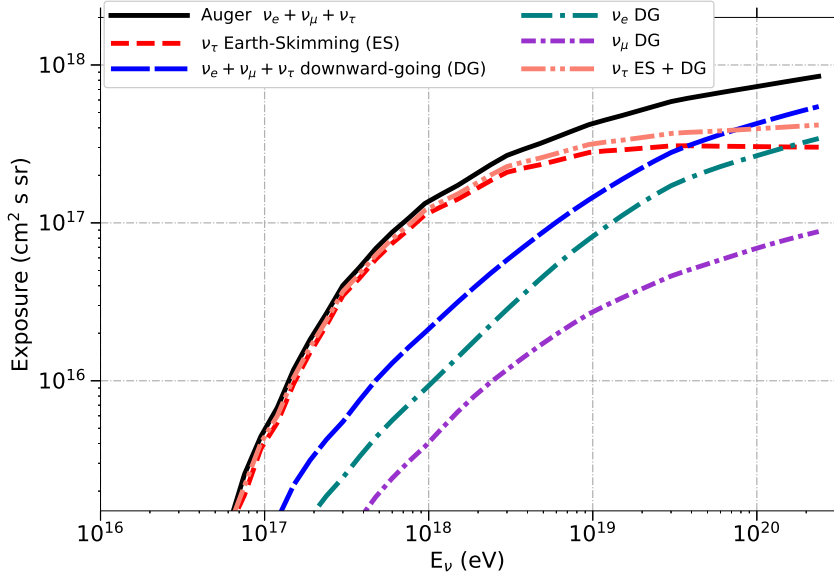


Figure 3.9: Exposure of the SD to ultra high energy neutrinos as a function of the neutrino energy in the period from 1 January 2004 to 31 August 2018. The total exposure is represented by the black solid line. Exposures for Earth-skimming tau neutrinos only (red dashed line), all flavors downward-going neutrinos (blue dashed line), downward-going electron neutrinos (green dashed line), downward-going muon neutrinos (purple dashed line) and Earth-skimming and downward-going tau neutrinos (pink dashed line) are also shown. The exposures are obtained assuming a flavor ratio of 1:1:1. Figure from [106].

the energy of the emerging tau lepton E_τ , zenith angle θ , azimuth angle ϕ , position (x, y) of the shower on the SD array, the altitude of the decay point of the tau lepton above the ground h_{dec} and time t . The total exposure ε_{tot} of the SD to ultra high energy neutrino events, together with the single and combined Earth-skimming and upward-going neutrino exposures, is shown in Figure 3.9.

Assuming a differential neutrino flux $\Phi = k \cdot E_\nu^{-2}$, an upper limit on the value of k at 90% confidence level can be set as:

$$k^{0.90} = \frac{N_\nu^{0.90}}{\int_{E_\nu} E_\nu^{-2} \varepsilon_{\text{tot}}(E_\nu) dE_\nu}, \quad (3.9)$$

where $N_\nu^{0.90} = 2.39$ is the Feldman-Cousins upper limit [86] at 90% confidence interval on the number of neutrino events for zero observed events and zero events expected from background. The integrated limit at 90% confidence level for a single neutrino flavor is [106]:

$$k^{0.90} < 4.4 \cdot 10^{-9} \text{GeV cm}^{-2} \text{s}^{-1} \text{sr}^{-1}. \quad (3.10)$$

The upper limit on k can be calculated also in a differential way by dividing the integration interval in bins of width ΔE_ν . Both the integrated upper limit and the

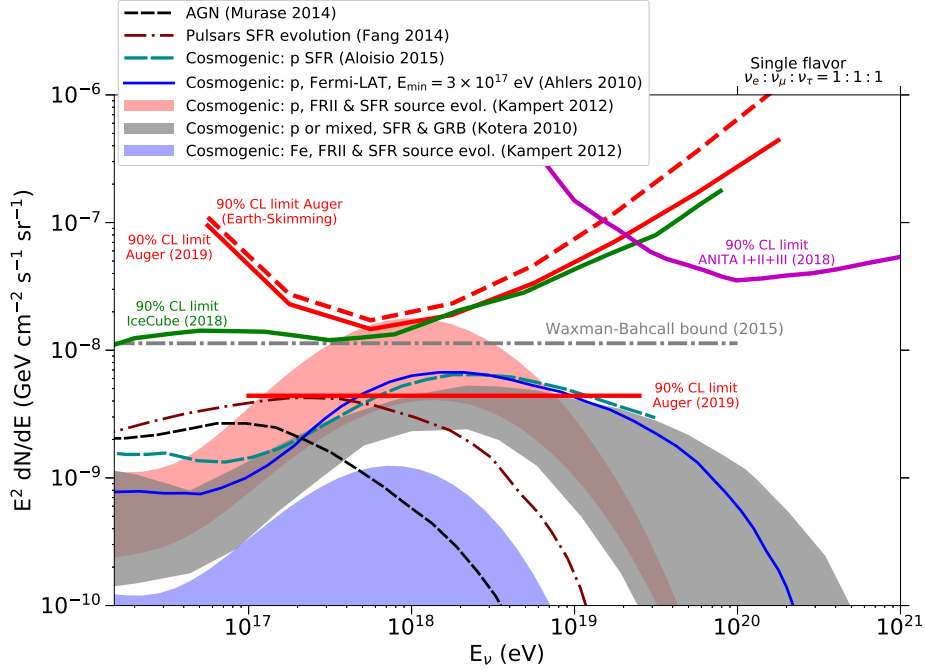


Figure 3.10: Upper limits on k at 90% confidence level from the Pierre Auger Observatory. The integrated upper limit is represented by the solid straight red line, while the differential upper limits for all channels and flavors and for Earth-skimming tau neutrinos are represented by the solid red line and the dashed red line, respectively. The differential limits from IceCube [109] (solid green line) and ANITA I+II+III [110] (solid dark magenta line) are also shown. The expected neutrino fluxes from different cosmogenic and astrophysical models of neutrino production [111, 112, 113, 114], as well as the Waxman-Bahcall bound [115], which is derived from the observed cosmic ray flux, have also been added to the plot. All limits and fluxes are converted to single flavor. Figure from [106].

differential upper limit with $\Delta \log_{10} E_\nu = 0.5$, together with the results from other experiments and the flux predictions from different models, are shown in Figure 3.10. Upper limits can be used to constrain the so-called cosmogenic models that predict the production of neutrinos from the interaction of UHECRs with the intergalactic radiation fields.

3.1.5 Search for neutrinos from point-like sources with the SD

The Pierre Auger Observatory can be used also to search for neutrinos from point-like sources. Since the search for diffuse neutrinos described in section 3.1.4 is performed in the zenith angle range $[60, 95]^\circ$, neutrinos from point-like sources can be searched for at a certain instant only from the region of the sky defined by this range. The time dependent zenith angle corresponding to a point-like source of equatorial coordinates

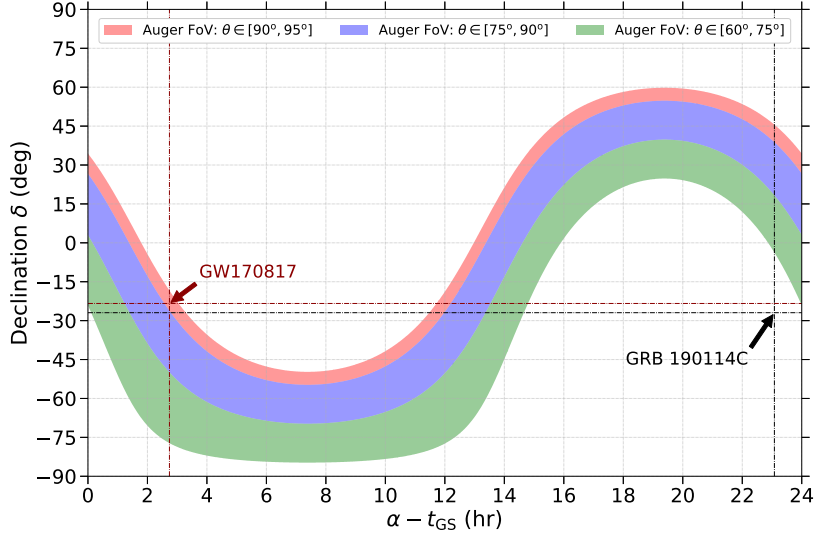


Figure 3.11: Instantaneous field of view (FoV) of the Pierre Auger Observatory for Earth-skimming neutrinos (red band), inclined downward-going neutrinos with a zenith angle in the range $[75, 90]^\circ$ (blue band) and inclined downward-going neutrinos with a zenith angle in the range $[60, 75]^\circ$ (green band) as a function of the hour angle $\alpha - t_{\text{GS}}$. The declination range for a given location in right ascension α at a given GST converted to angle t_{GS} can be directly read at the corresponding hour angle $\alpha - t_{\text{GS}}$. As an example, the positions of two sources are shown: GW170817 visible in Auger in the Earth-skimming channel at the time of emission [65], and GRB 190114C [118] not visible in the different channels of Auger at the time of the burst. Figure from [119].

δ and α as seen from the latitude $\lambda = -35.2^\circ$ of the Pierre Auger Observatory is given by [116]:

$$\cos \theta(t) = \sin \lambda \sin \delta + \cos \lambda \cos \delta \sin \left(2\pi \frac{t}{T} - \alpha \right), \quad (3.11)$$

where t is the local sidereal time and T is the duration of one sidereal day. The three zenith angle ranges into which the analysis is divided correspond to different fields of view for the neutrino search. The field of view bands in equatorial coordinates as a function of $\alpha - t_{\text{GS}}$, where $t_{\text{GS}} = 2\pi \frac{t}{T} + \ell$ is the Greenwich Sidereal Time (GST) converted to angle and ℓ is the mean longitude of the Pierre Auger Observatory, is shown in Figure 3.11.

The exposure of the SD to neutrinos from point-like sources as a function of the neutrino energy and source declination, $\varepsilon(E_\nu, \delta)$, is calculated in the same way as in the search for diffuse neutrinos (see Eq. 3.7 and Eq. 3.8), except for the solid angle integration over the sky. The dependence on the declination δ is given by Eq. 3.11. The integration over time is performed considering only the periods when the source is in the zenith angle range of the corresponding analysis. The time dependence of the SD configuration during data taking can make the exposure dependent also on α . However,

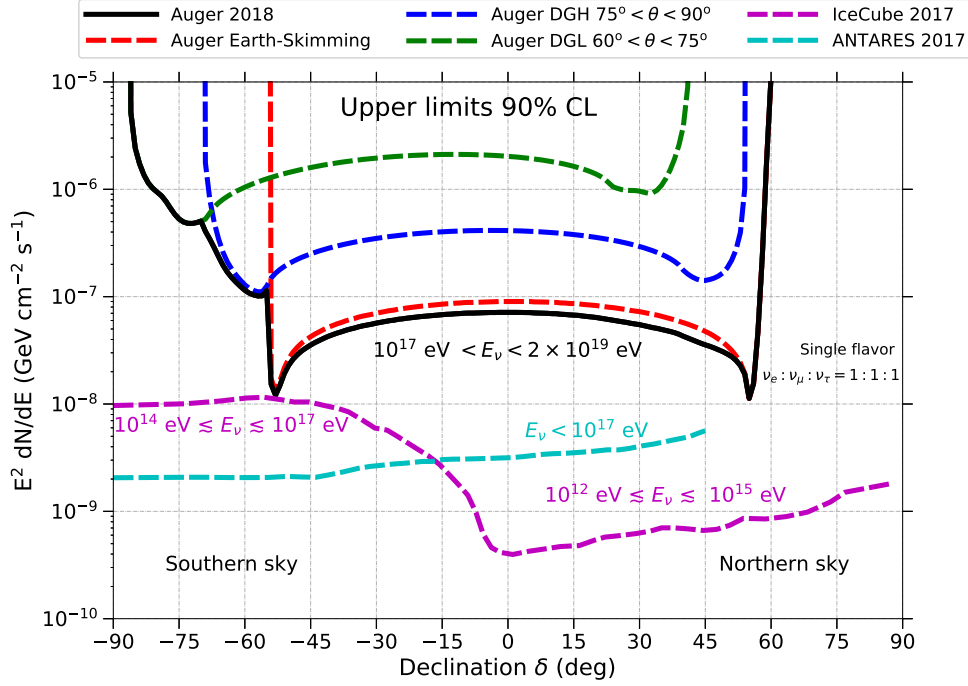


Figure 3.12: Upper limits at 90% confidence level on k_{PS} for a single flavor point-like neutrino flux as a function of the source declination δ obtained with the Pierre Auger Observatory for all channels and flavors (solid black line) and for Earth-skimming neutrinos (dashed red line), inclined downward-going neutrinos with a zenith angle in the range $[75, 90]^\circ$ (dashed blue line) and inclined downward-going neutrinos with a zenith angle in the range $[60, 75]^\circ$ (dashed green line). The upper limits obtained by IceCube (2008-2015) [120] and ANTARES (2007-2015) [121] in different energy ranges are also shown. Figure from [119].

the modulation in α , caused by the small diurnal variation due to the fluctuations in the number of stations, is less than 1% when averaged over a large number of sidereal days [117]. For this reason, the exposure can be considered to depend only on δ .

No candidate events were found in data taken from 1 January 2004 to 31 August 2018, therefore upper limits on the neutrino flux from point-like sources can be derived. Assuming a differential neutrino flux $\Phi = k_{\text{PS}}(\delta) \cdot E_\nu^{-2}$ and zero events expected from background, an upper limit on $k_{\text{PS}}(\delta)$ at 90% confidence level can be set for all channels and flavors and independently for Earth-skimming neutrinos, inclined downward-going neutrinos with a zenith angle in the range $[75, 90]^\circ$ and inclined downward-going neutrinos with a zenith angle in the range $[60, 75]^\circ$ by following the same procedure as described in section 3.1.4. The upper limits as a function of the source declination, together with the results obtained by ANTARES and IceCube in different energy ranges, are shown in Figure 3.12.

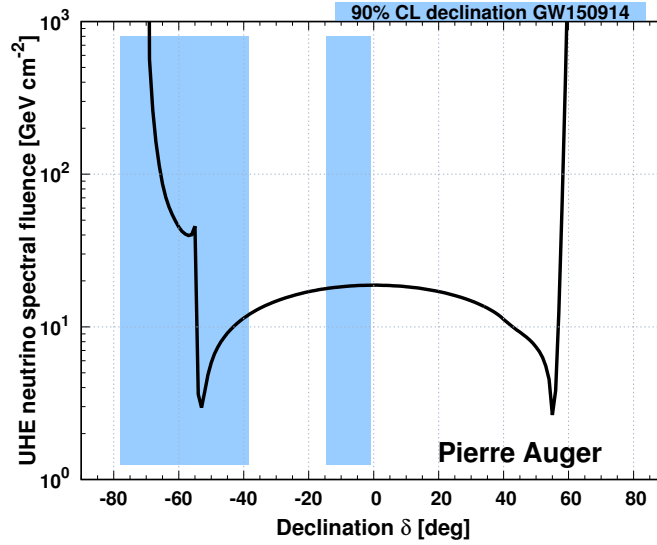


Figure 3.13: Upper limits at 90% confidence level on the ultra high energy neutrino spectral fluence per flavor from GW150914 as a function of the declination δ . The declination values corresponding to the 90% confidence level region of the source localization in the sky for GW150914 are represented by the blue bands. Figure from [123].

3.1.6 Neutrino follow-up of gravitational wave events with the SD

The neutrino follow-up of gravitational wave events is performed by applying the standard neutrino search (see section 3.1.4) in the same time windows mentioned in section 3.1.3 i.e. the time window of 500 s before and after the merger and the 24-hour period after the merger. Inside these two time windows, the search is limited to the periods when the 90% confidence level region of the source localization in the sky is in the SD neutrino field of view of the Pierre Auger Observatory. The two time windows are defined in order to take into account the properties of the prompt and afterglow emissions of the GRBs that are produced in the merging of compact objects. Neutrinos are expected to be produced in the interaction of accelerated cosmic rays with GRB photons of the prompt phase and lower energy photons of the afterglow. The two time windows are upper bounds on the time delay between gravitational wave events and neutrinos produced in the prompt phase [124] and the duration of the afterglow [125]. Since no candidate events were found [122], upper limits on the value of $k^{0.90}$ were derived in a similar way as for neutrinos from point-like sources (see section 3.1.5) and then used to calculate upper limits on the neutrino spectral fluence. The upper limits on the neutrino fluence for the first gravitational wave event ever detected, GW150914 [62], is shown in Figure 3.13. The later observation of the gravitational wave event GW170817 from a binary neutron star merger [63] was coupled with the detection of a short gamma ray burst after ~ 1.7 s from the merger [63]. The Pierre Auger

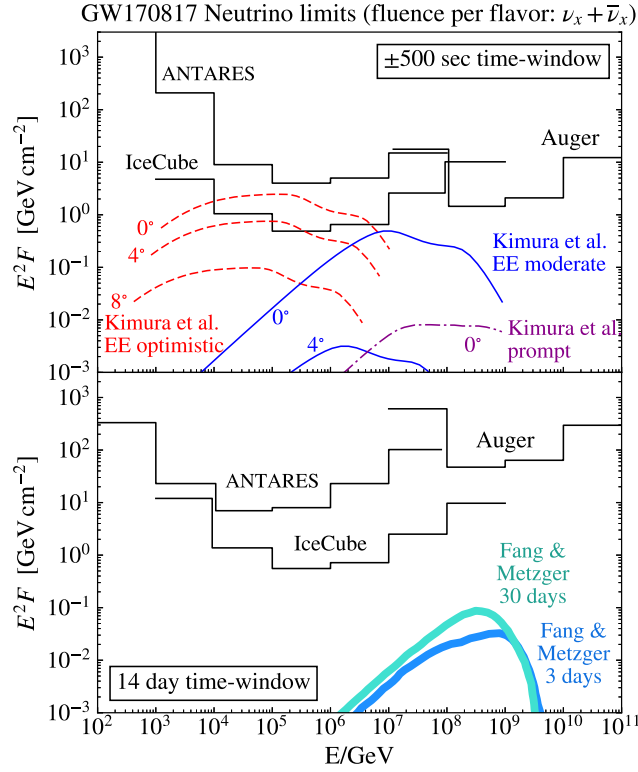


Figure 3.14: Upper limits at 90% confidence level on the neutrino spectral fluence from GW170817 during the time window of 500 s before and after the merger (upper plot), and the 14-day period after the merger (lower plot). Assuming a spectral fluence $F = F_{up} \cdot (E_\nu/\text{GeV})^{-2}$, upper limits on F_{up} are calculated separately for each energy bin. Predictions from neutrino emission models are also shown. The upper limits in the upper plot are compared with the predictions from models of prompt emission and extended emission (EE) [126] for the case of line of sight aligned with the rotation axis and for different off-axis viewing angles. The upper limits in the lower plot, on the other hand, are compared with the predictions from models for longer lived emission [127]. The models shown in both the plots are scaled to 40 Mpc, which is the distance of the galaxy NGC 4993 where the merger is localized. Assuming that all flavors have the same fluence, as expected from the standard neutrino oscillation, all fluences are shown as the per flavor sum of neutrino and anti-neutrino fluence. Figure from [65].

Collaboration performed a neutrino follow-up for this event together with the IceCube and ANTARES Collaborations [65]. Given the prolonged photon emission, the three Collaborations agreed to search for neutrino events over an extended 14-day period after the merger. The resulting upper limits at 90% confidence level on the neutrino spectral fluence during the time window of 500 s before and after the merger and the 14-day period after the merger are shown in Figure 3.14.

3.1.7 Search for neutrons with the SD

Similarly to photons and neutrinos, neutrons are not deflected by magnetic fields and thus point directly to their sources. They are produced in charge exchange interactions of high energy protons with ambient photon fields, protons or nuclei. The positively charged pion produced in these interactions is associated to a neutron which carries most of the energy of the proton. The interactions of protons give rise also to neutral pions, which decay producing photons. For this reason, neutrons are necessarily produced in association with photons. These photons carry only a small fraction of the original proton energy, therefore a E^{-2} or steeper accelerated proton spectrum results in a number of neutrons with a given energy which is larger than that of photons with the same energy. This makes neutrons excellent cosmic messengers for the identification of their sources. The mean decay path length for relativistic neutrons with energy E is $9.2 \text{ kpc} \cdot (E/\text{EeV})$ [68]. Considering that our galaxy has a radius of about 15 kpc and that the Earth is about 8.3 kpc far from the Galactic center, neutrons with energies of a few EeV should allow to identify sources within most of our galaxy. When neutrons enter the atmosphere, they produce air showers that can not be distinguished from those produced by protons. For this reason, a flux of neutrons from a given direction can be identified only by searching for an excess of air showers from that direction within the angular resolution of the Pierre Auger Observatory. Similarly to the search for photons from point-like sources (see section 3.1.2), the search for neutrons is performed on a total of eleven target sets consisting of nine classes of possible sources of photons plus the Galactic center and the Galactic plane combined in a stacked analysis [128]. The targets considered in this search are photon sources because the production of neutrons is associated to that of photons, as mentioned above. Sources in a target set are weighted according to their electromagnetic flux, their exposure to the Pierre Auger Observatory and their flux attenuation factor, which is defined as the fraction of emitted neutrons surviving the decay from the distance of the source under the assumption of an emitted neutron energy spectrum of E^{-2} . In each target set, weights are required to sum to 1. This analysis is performed in the energy ranges $[1, 2)$ EeV, $[2, 3)$ EeV, $E \geq 3$ EeV and $E \geq 1$ EeV by using events with a zenith angle $\theta < 60^\circ$ collected with the SD in the period from 1 January 2004 to 31 October 2013 [128]. In each energy range the average angular resolution for the declination corresponding to a given target is used to optimize the solid angle size for that particular target [129]. Similarly to the photon case, the number of events expected without the neutron flux in each solid angle region is given by the average number obtained from 10^4 simulated data sets, each with a number of events equal to that of the actual data set. This average number, which allows not to have structure on small angular scales, is used as number of background events in order to identify an excess of events from a given target. For each simulated data set and energy range, the arrival directions are sampled from the measured distributions of zenith angle, azimuth angle and sidereal time [128]. Each target i is assigned with a p-value following the same procedure as the photon case (see section 3.1.2) [130].

Since no evidence of excess of a neutron flux was found from any of the target sets,

an upper limit on the neutron flux was derived for each target set [128]. The upper limit on the neutron flux is calculated as the Zech upper limit [98] at 95% confidence level on the number of neutrons divided by the directional exposure and by the fraction of total signal encompassed in the optimized target region [129]. The directional exposure is defined as the number of events expected from background in the target region divided by the solid angle of that target and by the cosmic ray intensity, which is expressed in $(\text{km}^2 \text{ sr yr})^{-1}$ and is obtained from the integration of the energy spectrum over the relevant energy range. The upper limit is calculated assuming a E^{-2} neutron spectrum above 1 EeV.

The upper limits derived in this search are below the energy fluxes detected from TeV gamma ray sources in our galaxy. Therefore, a E^{-2} Fermi-acceleration of protons up to EeV energies from the same sources is excluded, since the flux of EeV neutrons would be larger than that of TeV gamma rays because of the more efficient production of neutrons with respect to gamma rays of the same energy, as mentioned above. Furthermore, the upper limit obtained for the Galactic plane strongly constrain the models for continuous production of EeV protons in our galaxy. An estimate of the proton emission rate can be derived by considering that protons have to be emitted in the galactic disk at a rate that compensates for their escape. The associated neutron emission rate depends on the model and can be larger than that of protons if protons are magnetically confined to the sources. In this case, only neutrons escape and EeV protons are produced in their decay. The upper limit on the neutron flux from the Galactic plane can be used to constrain the ratio η between the neutron luminosity and the proton luminosity. Using an estimate of the proton emission rate, the upper limit $\eta_{\text{UL}} \simeq 0.006$ [128] was found.

3.2 The puzzle of the ANITA anomalous events

The ANITA Collaboration has recently reported two anomalous events that are consistent with the interpretation of upward-going showers. Since these events appear to be in tension with the predictions of the Standard Model (SM) of particle physics [61], the Pierre Auger Collaboration has recently started a search for upward-going showers to support or constrain this interpretation. If confirmed, it would require either new phenomena or significant modifications to the SM. The next subsections deal with the description of the ANITA experiment and the characteristics of the anomalous events detected by it.

3.2.1 The ANITA experiment

The ANITA experiment is a balloon-borne experiment which aims to detect ultra high energy neutrinos and cosmic rays in Antarctica. It consists of an array of radio antennas mounted on the payload of a helium balloon flying at an altitude of 35–37 km [131]. The radio antennas can detect the coherent radio pulses produced by both ultra high energy neutrinos interacting in the Antarctic ice via Askaryan emission [53] and UHECR air showers via geomagnetic emission [52]. The radio pulses produced by

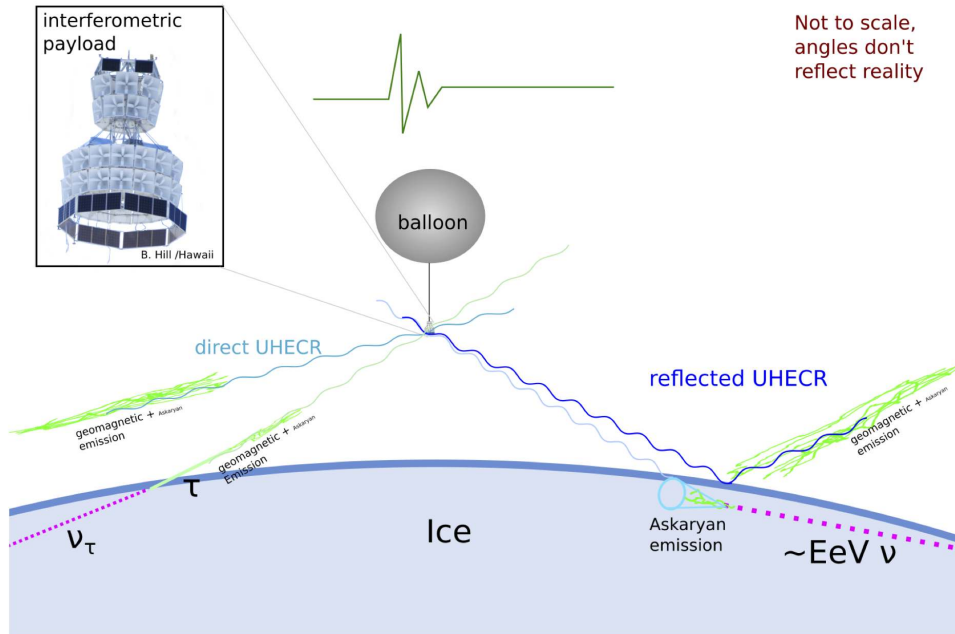


Figure 3.15: Schematic view of the different classes of events that can be detected with the ANITA experiment. Figure from <http://www.hep.ucl.ac.uk/uhen/anita/>.

downward-going air showers reflect off the ice cap resulting in an observed signal with an inverted phase. The phase inversion occurs because radio pulses travel from a less dense medium into a denser material. The ANITA experiment can detect also nearly-horizontal cosmic ray showers whose signals arrive directly at the payload without showing a phase inversion [60], but this can happen just within $\sim 6^\circ$ of the horizontal [132]. A schematic view of the different classes of events that can be detected with the ANITA experiment is shown in Figure 3.15. The ANITA experiment measure both the horizontal (Hpol) and vertical (Vpol) polarization of the radio pulses. The radio pulses produced by air showers have a polarization perpendicular to the Earth's magnetic field, which is mostly vertical in Antarctica. This results in signals that are horizontally polarized. Furthermore, the vertical polarization of reflected radio pulses from downward-going air showers is further suppressed because of the low reflectivity of the air-ice interface for s-polarized waves. Radio pulses from neutrinos interacting in the ice, on the other hand, have a suppressed horizontal polarization because of the suppression of p-polarized waves when passing from ice to air [133]. This difference is used to distinguish between neutrino and cosmic ray signals. As an example of the phase inversion of reflected cosmic ray signals, the pulse shapes of 14 reflected cosmic ray events and 2 direct cosmic ray events measured by the ANITA Collaboration are shown in Figure 3.16. The arrival direction of the radio signal is reconstructed using the arrival time difference between pairs of antennas [131], while the energy of the UHECR is reconstructed by combining the total power of the observed radio signal with the

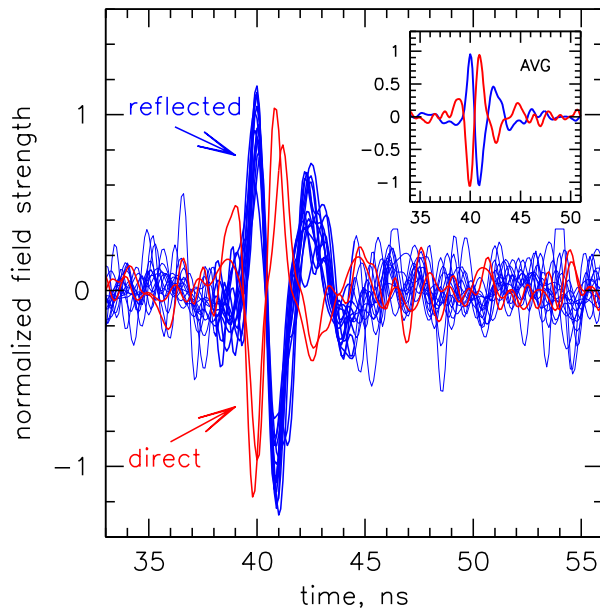


Figure 3.16: Overlay of 16 UHECR event Hpol pulse shapes. The phase of the 14 reflected events (blue) is inverted with respect to that of the 2 direct events (red). In the top right box the average pulse profiles for reflected and direct events are shown. Figure from [134].

position of the shower core with respect to the detector, obtained from the spectral analysis of the radio signal [135]. A detailed description of the event reconstruction for UHECRs can be found in [136].

3.2.2 The ANITA anomalous events

The two anomalous events measured by ANITA during its first (I) and third (III) flights were detected with an elevation angle of $27.4 \pm 0.3^\circ$ [60] and $35.0 \pm 0.3^\circ$ [61], respectively, and energies above ~ 0.2 EeV [139]. The pulse shapes of the two events, which are shown in Figure 3.17, are those expected for direct air showers, but their elevation angles show a large deviation from the horizontal. If these events are interpreted as tau lepton induced air showers resulting from a diffuse flux of cosmic tau neutrinos (see Figure 3.15), their energies and elevation angles appear challenging to reconcile with the SM. At these energies, in fact, the neutrino-nucleus cross section is large, resulting in a mean free path of few hundred km, while the cord lengths through the Earth corresponding to the observed elevation angles are 5700 km for the ANITA I event and 7200 km for the ANITA III event [137]. Therefore, a neutrino flux exceeding the current bounds on diffuse neutrino fluxes would be required [61]. A possible explanation for the ANITA anomalous events that does not involve physics beyond SM could be a strong transient neutrino flux from a point source. This hypothesis was tested by

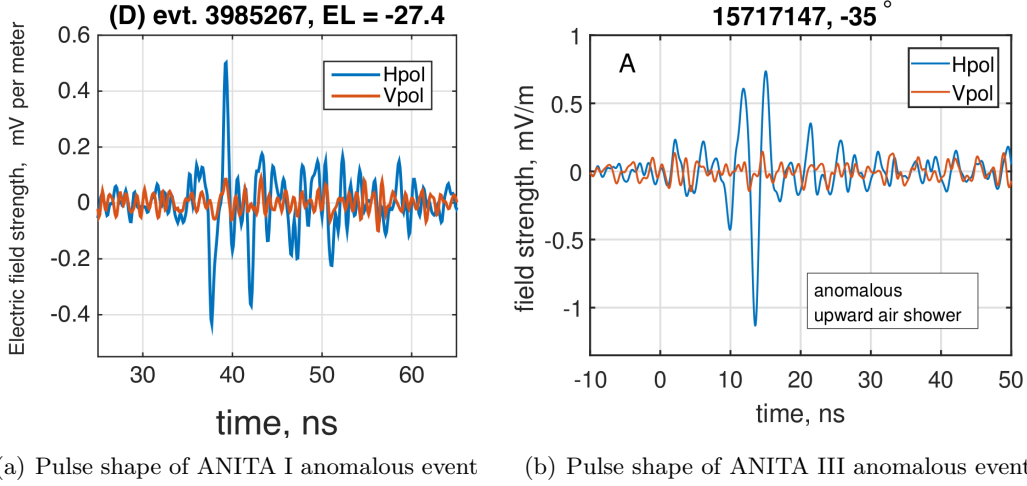


Figure 3.17: Pulse shapes of the two anomalous events detected by ANITA during its first (a) and third (b) flights. The two events have elevation angles of $27.4 \pm 0.3^\circ$ (a) and $35.0 \pm 0.3^\circ$ (b), while their energies are above ~ 0.2 EeV. The signals are characterized by a horizontal polarization and a non-inverted phase, being consistent with the interpretation of upward-going showers coming directly from the ground. Figure (a) is from [60], while Figure (b) is from [61].

the IceCube Collaboration, which performed a search for the secondary neutrino flux in the TeV-PeV range expected to be associated to any ultra high energy neutrino flux in the reconstructed direction of the ANITA anomalous events. This secondary flux is due to the tau neutrino regeneration, which consists in the production of secondary tau neutrinos in the decays of tau leptons coming from the CC interactions of tau neutrinos in the Earth. Three complementary approaches were used by the IceCube Collaboration. The first analysis consisted of a search for events in spatial coincidence with the ANITA events in short time windows centered on each ANITA event. The ANITA I anomalous event was excluded from this analysis because at the time of its detection IceCube had not yet reached the full detector configuration. As regards the ANITA III anomalous event, about 0.5 s before its detection IceCube entered in a state of run transition that lasted for about one minute, resulting in no data-taking in the corresponding time window. For this reason, the search for neutrino candidates in coincidence with this event was performed considering the two time windows 10^3 s and 10^5 s, which are large enough to make the time window of the run transition a negligible fraction of the selected intervals. For the second analysis, a temporal coincidence with the ANITA events was not required. A search for events clustered in time and space was performed. Finally, the third analysis searched for events clustered in space over the IceCube data from seven years of operation. The IceCube Collaboration did not find an evidence for a significant correlation above the expectation from background in any of the analyses [138]. For this reason, a confirmation or a constraint from a

different experiment would be of particular interest. To provide some insight into the nature of the ANITA anomalous events, the Pierre Auger Collaboration performed a generic search for upward-going showers, to which the FD is sufficiently sensitive when used in monocular mode.

3.3 Search for ANITA-like events with the FD

The Multi-Messenger searches carried on within the Pierre Auger Collaboration include also the search for upward-going showers. As seen in section 3.1.4, a search for nearly horizontal upward-going showers has already been performed within the Pierre Auger Collaboration by exploiting the SD. However, upward-going showers with elevation angles far from the horizontal i.e. with zenith angles much larger than 90° are not expected to produce signals in the SD and can be detected only with the FD. Therefore, the Pierre Auger Collaboration exploited the data collected with the FD in 14 years of operation to perform a generic search for upward-going showers in the energy and elevation angle regions of interest for ANITA-like events. Before starting this search, a Monte Carlo simulation for upward-going showers based on simple assumptions, hereinafter referred to as “Fast Monte Carlo simulation”, was developed in order to study the detectability of this class of events with the FD from a geometrical point of view. To perform a generic search for upward-going showers and allow the results to be used to test different physical scenarios, protons have been used to approximate the start of the showers in simulations. The results obtained by considering proton induced upward-going showers, in fact, can be easily scaled to fit models that predict showers initiated by different particles. The next chapter deals with the description of the Fast Monte Carlo simulation, while the details and the preliminary results of the search for upward-going showers will be discussed in Chapter 5.

CHAPTER 3. MULTI-MESSENGER ASTROPHYSICS WITH THE PIERRE
AUGER OBSERVATORY

Chapter 4

A Fast Monte Carlo simulation for upward-going showers

Before starting the Real Monte Carlo simulation for upward-going showers i.e. a Monte Carlo simulation which properly takes into account the actual status of the Auger detectors and of atmospheric conditions during data taking, a C++ Fast Monte Carlo simulation has been developed in order to give a rough estimate of the maximum distance at which events can be detected by the FD telescopes. The Real Monte Carlo simulation, needed to calculate the FD exposure to upward-going showers, is quite expensive in terms of computing time. Therefore, those events that have no chance to be detected by the FD are not simulated reducing the computing time and increasing the statistics for detectable events. The Fast Monte Carlo simulation has been performed by using simple geometrical and physical assumptions in order to optimize the Real Monte Carlo one.

4.1 Simulation of proton induced upward-going showers

Upward-going showers can be initiated by particles emerging from the Earth and interacting or decaying in the atmosphere at a certain height or within the rock just below the Earth's crust. Hereinafter, the impact point of the particle trajectory on the ground will be referred to as the “exit point”. Another quantity of relevance for establishing the energy of the ANITA events [139] is the height of the point of first interaction of the primary particle i.e. H_{fi} . The range of H_{fi} is also important to be tuned as showers that start at high altitudes are naturally less likely to be triggered because they tend to be further away. The geometry of an upward-going shower is illustrated in Figure 4.1. As mentioned in section 3.3, proton induced showers have been considered in simulations in order to perform a generic search for upward-going showers. Considering that for interaction altitudes above ~ 5 km the showers are not fully developed before reaching ANITA because of the reduced air density [139], primary protons have been injected at uniformly generated heights between 0 km and 9 km above ground at Observatory site (~ 1400 m a.s.l.). To focus on the energy

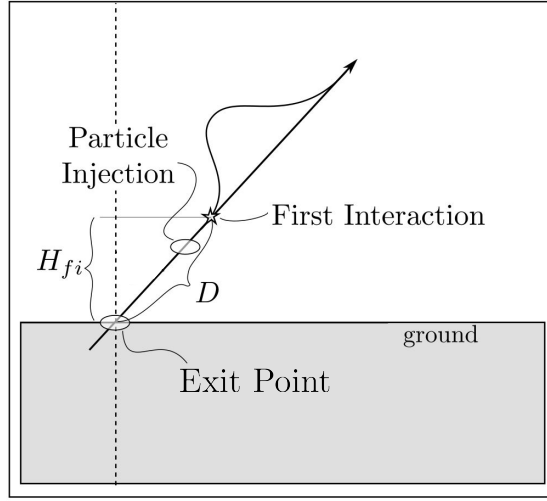


Figure 4.1: Schematic view of the generation geometry of an upward-going shower. D is the distance along the shower axis of the point of first interaction of the primary particle from the exit point, the injection point is the point at which the primary particle arises and H_{fi} is the height of the point of first interaction with respect to the ground. Figure from [140].

and angular regions of interest for ANITA-like events, primary protons have been generated in the $\log_{10}(E/\text{eV})$ region [17, 18.5] with a uniform distribution. The zenith and azimuth angles have been uniformly diced in the regions $[110, 180]^\circ$ and $[0, 360]^\circ$, respectively. The longitudinal profiles of the proton induced air showers have been approximated by considering only the injection point and the position along the shower axis of the depth of the shower maximum X_{max} . The X_{max} of each simulated shower has been extracted from a p.d.f. based on the generalized Gumbel distribution [141].

4.1.1 Parameterization of the X_{max} distributions

The generalized Gumbel distribution is used to describe the probability of having a certain X_{max} as a function of energy and primary mass. It is based on the connection between the generalized Gumbel statistics and the distribution of the sum of non-identically distributed variables in the cascade initiated by the primary particle, which is a dissipative stochastic system [142]. For each primary particle with a given energy, the stochastic fluctuations in the position of the first interaction point X_{first} and the interactions of the secondary particles produced in the cascade are responsible for the fluctuations in the position of the X_{max} .

For many systems that undergo dissipative interactions where the energy is the sum of random variables, the energy distribution can be approximated by a generalized Gumbel function [143]. A dissipative stochastic system can be treated as a one dimensional lattice with N sites whose dynamics is defined by: i) the energy injection at a boundary site with given rates, ii) the energy transfer from site i to site $i + 1$ with

a known rate and iii) the energy dissipation at site j with a given rate. Considering a specific case for the rates [144], the total energy (i.e. the sum of the energy of each site) follows the generalized Gumbel distribution [142]:

$$\mathcal{G}(z) = \frac{1}{\sigma} \frac{\lambda^\lambda}{\Gamma(\lambda)} \left(e^{-\lambda z - \lambda e^{-z}} \right), \quad z = \frac{x - \mu}{\sigma}, \quad (4.1)$$

where σ is a scale parameter related to the spread of the distribution, λ is a shape parameter, Γ is the Euler gamma function and μ is a location parameter related to the mean of the distribution. The distribution for the case of more general rates is not exactly known, but the Gumbel is expected to be still a good approximation of the true one. Given the similarities between this model and the Heitler model described in section 1.4, the latter can be considered as a dissipative stochastic system with an energy injection equal to that of the primary particle at site $n = 0$ and to zero at site $n = n_c$, an energy in each site proportional to the number of secondary particles in that site, an energy transfer given by the shower development between the site n and the site $n + 1$ and an energy dissipation at site $n = j$ given by the missing energy per site. The generalized Gumbel can be used also to describe the distribution of X_{\max} . This can be achieved by parameterizing the Gumbel density function $\mathcal{G}(X_{\max})$ as a function of primary energy E and nuclear mass A . The parameterized function can then be tested using Monte Carlo simulations of air showers for different values of E and A [142]. For the case of nuclei, the assumed parameterizations for μ , σ and λ are [142]:

$$\mu(A, E) = p_{0_\mu} + p_{1_\mu} \log_{10} \left(\frac{E}{E_0} \right) + p_{2_\mu} \left[\log_{10} \left(\frac{E}{E_0} \right) \right]^2, \quad (4.2)$$

$$\sigma(A, E) = p_{0_\sigma} + p_{1_\sigma} \log_{10} \left(\frac{E}{E_0} \right), \quad (4.3)$$

$$\lambda(A, E) = p_{0_\lambda} + p_{1_\lambda} \log_{10} \left(\frac{E}{E_0} \right), \quad (4.4)$$

where $E_0 = 10^{19}$ eV is a reference energy and the dependence of the parameters on A is empirically given by [142]:

$$p_0^{\mu, \sigma, \lambda} = a_0^{\mu, \sigma, \lambda} + a_1^{\mu, \sigma, \lambda} \ln A + a_2^{\mu, \sigma, \lambda} (\ln A)^2, \quad (4.5)$$

$$p_1^{\mu, \sigma, \lambda} = b_0^{\mu, \sigma, \lambda} + b_1^{\mu, \sigma, \lambda} \ln A + b_2^{\mu, \sigma, \lambda} (\ln A)^2, \quad (4.6)$$

$$p_2^\mu = c_0^\mu + c_1^\mu \ln A + c_2^\mu (\ln A)^2. \quad (4.7)$$

These 7 parameters are found by fitting the distributions of X_{\max} from simulations.

Since UHECRs have energies that are far beyond the energy scale of human-made accelerators, an important role in the simulations and in the interpretation of the UHECR data is played by the extrapolation at higher energies of the experimental results obtained at lower energies. To this aim, different hadronic interaction models have been developed. The most frequently used hadronic interaction models within the

UHECR community are QGSJET II-04 [145], SIBYLL 2.3c [146, 147] and EPOS-LHC [148], which are those considered and implemented in the Fast Monte Carlo simulation. The corresponding parameters used in the parameterization of the X_{\max} distributions are listed in table 4.1. More details on the hadronic interaction models can be found in Appendix B.

QGSJET II-04	a_0	a_1	a_2	b_0	b_1	b_2
μ	758.65	-12.3571	-1.24539	56.5943	-1.01244	0.228689
σ	35.4234	6.75921	-1.46182	-0.796042	0.201762	0.201762
λ	0.671545	0.373902	0.075325	0.0304335	0.0473985	-0.000564531
SIBYLL 2.3c	a_0	a_1	a_2	b_0	b_1	b_2
μ	790.028	-15.0225	-1.30553	60.8843	-0.0908545	0.0726719
σ	41.0622	-1.2319	-0.574515	-0.422316	-0.621309	0.138754
λ	0.774802	0.292617	-0.00539918	0.0449265	0.0271851	-0.00194634
EPOS-LHC	a_0	a_1	a_2	b_0	b_1	b_2
μ	775.457	-10.3991	-1.75261	58.5306	-0.827668	0.231144
σ	32.2632	3.94252	-0.864421	1.27601	-1.81337	0.231914
λ	0.641093	0.219762	0.171124	0.0726131	0.0353188	-0.0131158

QGSJET II-04	c_0	c_1	c_2
μ	-0.534683	-0.17284	-0.019159
SIBYLL 2.3c	c_0	c_1	c_2
μ	-0.895554	0.111875	-0.0634885
EPOS-LHC	c_0	c_1	c_2
μ	-1.40781	0.225624	-0.10008

Table 4.1: Parameters used in the parameterization of the X_{\max} distributions for different hadronic interaction models. Parameterizations from [149].

4.1.2 A tool for the X_{\max} distributions

A tool to calculate the X_{\max} distributions according to the Gumbel parameterization described in the previous section has been developed. The inputs are the hadronic interaction model, the nuclear mass A and the primary energy E . I originally developed this code to be included in a more general tool for fitting the mass fractions from the X_{\max} distributions [150] and then it has been used in the Fast Monte Carlo simulation for upward-going showers. Given the hadronic interaction model and the

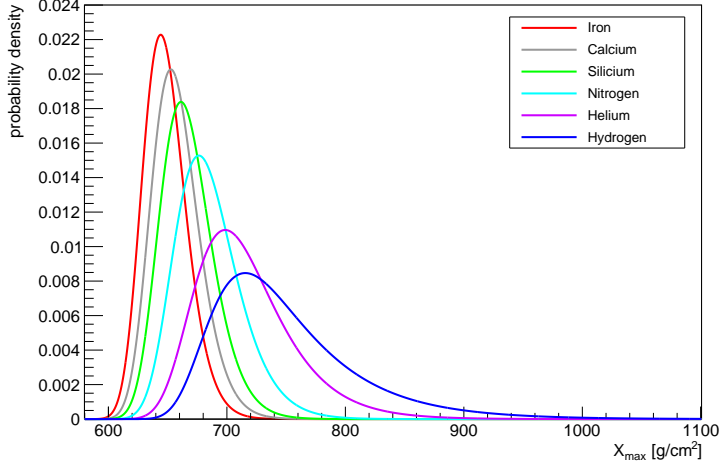


Figure 4.2: X_{\max} distributions for different primary nuclei (Iron, Calcium, Silicium, Nitrogen, Helium, Hydrogen) with energy $E = 10^{18}$ eV, obtained using the hadronic interaction model EPOS-LHC. The lower the nuclear mass A , the higher the value of X_{\max} the distribution is peaked at.

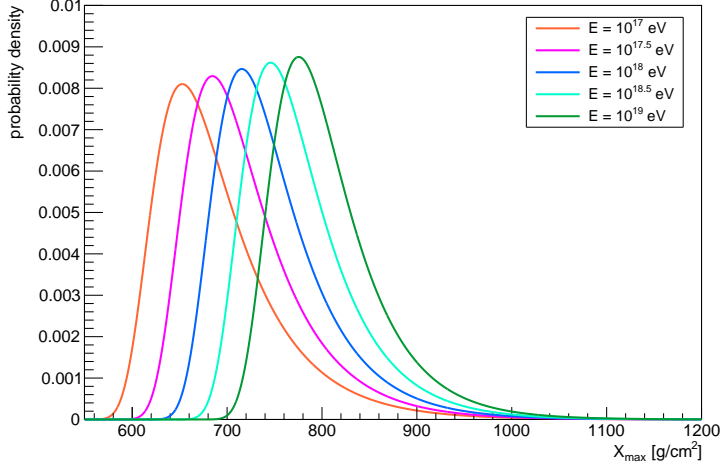


Figure 4.3: X_{\max} distributions for primary hydrogen nuclei with different energies (10^{17} eV, $10^{17.5}$ eV, 10^{18} eV, $10^{18.5}$ eV, 10^{19} eV), obtained using the hadronic interaction model EPOS-LHC. The higher the energy E , the higher the value of X_{\max} the distribution is peaked at.

primary energy E , the X_{\max} distributions shift towards higher values of X_{\max} with the decrease of the nuclear mass A . This means that lighter (heavier) elements are more likely to develop deeper (shallower) in the atmosphere. The X_{\max} distributions

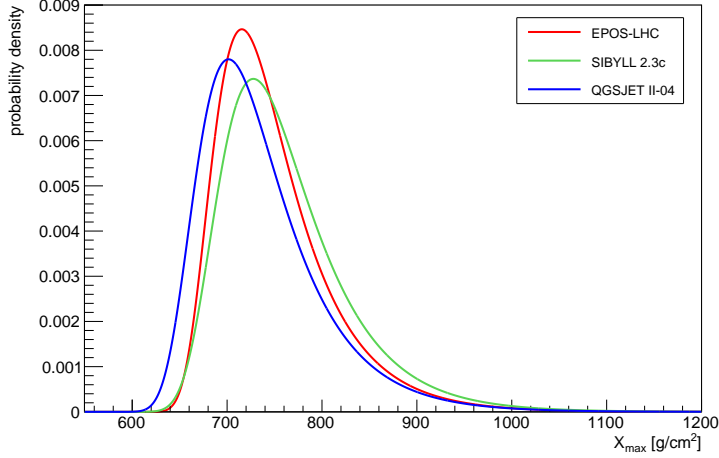


Figure 4.4: X_{\max} distributions for a primary hydrogen nucleus with energy $E = 10^{18}$ eV, obtained using different hadronic interaction models (EPOS-LHC, SIBYLL 2.3c, QGSJET II-04).

for a fixed hadronic interaction model and primary energy E and different values of the nuclear mass A are shown in Figure 4.2. Fixing the hadronic interaction model and the nuclear mass A , the value of X_{\max} corresponding to the peak of the distribution increases with the primary energy E . This behaviour is shown in figure 4.3 for the case of primary hydrogen nuclei.

The effect of the hadronic interaction model on the X_{\max} distributions can be studied by fixing the nuclear mass A and the primary energy E . The X_{\max} distributions for a primary hydrogen nucleus with energy $E = 10^{18}$ eV obtained by considering different hadronic interaction models are shown in Figure 4.4. The differences between the distributions are related to the principles the hadronic interaction models are based on (see Appendix B), showing how the interpretation of the cosmic ray data relies on the assumed model. Anyhow, given the assumptions made in the Fast Monte Carlo simulation, the conclusions that can be drawn from it are not affected by the choice of the hadronic interaction model. For this reason, only EPOS-LHC has been used in the following.

4.2 Geometric features of the simulation

Given the geometric equivalence between the four FD sites of the Pierre Auger Observatory, the Fast Monte Carlo simulation has been performed by considering only one of them. The single FD site has been assumed to have a field of view between 1.5° and 31.5° in elevation with respect to the horizontal and between 0° and 180° in azimuth. To take into account the presence of HEAT, an additional field of view of 30° in elevation between 31.5° and 61.5° above the horizontal has been also considered.

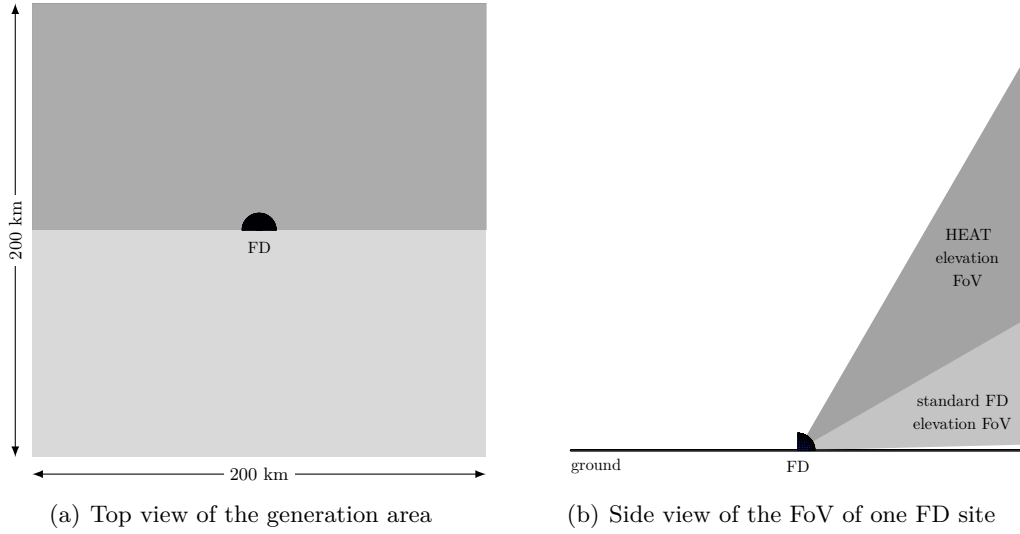


Figure 4.5: Top view of the generation area of $200 \text{ km} \times 200 \text{ km}$ centered at one FD site, with the dark gray area representing the azimuthal field of view of the FD (a), and elevation field of view (FoV) of one FD site, with the light and dark gray areas representing, respectively, the standard field of view of the FD, which is in common between the four FD sites, and the additional field of view considered in order to take into account also the presence of HEAT (b).

The exit points have been uniformly generated inside an area of $200 \text{ km} \times 200 \text{ km}$ centered at one FD. The generation area has been chosen sufficiently large to take into account also upward-going primary protons with exit points at large distances from the FD but with injection points close enough to produce a detectable shower. A schematic view of the generation area, together with a side view of the field of view of one FD site, are shown in Figure 4.5. The light gray region in Figure 4.5(a) represents the portion of the generation area extending behind the FD site. This area needs to be also considered in the simulation because upward-going protons with exit points behind the FD can produce showers that totally or partially develop inside the FD field of view, resulting in a detectable signal, as it will be shown in the next section.

4.3 Trigger conditions

Two simple trigger conditions have been implemented in the Fast Monte Carlo simulation. A simulated event is marked as detected by the FD if both the following conditions are satisfied:

1. The point corresponding to the position of the X_{max} along the shower axis is inside the field of view of the FD.
2. The distance d_{max} between the FD site and the projection of the position of

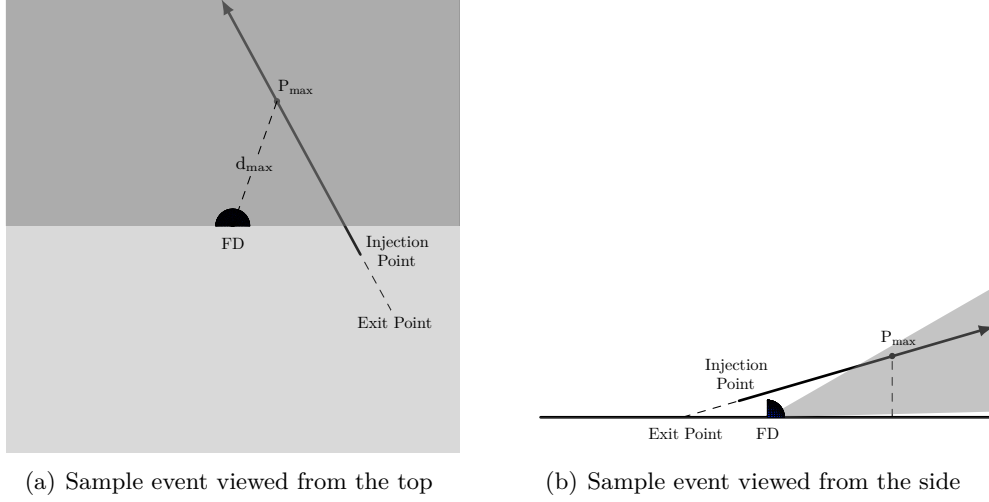


Figure 4.6: A schematic top view (a) and side view (b) of an upward-going event that can be potentially detected by the FD. The point P_{\max} corresponds to the position of the X_{\max} along the shower axis, while d_{\max} represents the distance between the FD site and the projection of P_{\max} on the generation area. For simplicity, only the standard FD field of view is shown. The event is considered detected by the FD if P_{\max} is inside the FD field of view and d_{\max} is less than $R_{\text{cut}}(E)$, where E is the energy of the primary particle.

the X_{\max} along the shower axis on the generation area is smaller than $R_{\text{cut}}(E)$. This cut value is the energy dependent distance above which the fraction of downward-going triggered events is less than 1% of the total number:

$$\frac{\int_{R_{\text{cut}}(E)}^{\infty} \varepsilon(R, E) R^2 dR}{\int_0^{\infty} \varepsilon(R, E) R^2 dR} < 0.01, \quad (4.8)$$

where $\varepsilon(R, E)$ is the trigger efficiency from [151]. The same cut values can be also used for upward-going showers by considering the projection of the position of the X_{\max} along the shower axis on the generation area.

The position of the X_{\max} along the shower axis has been calculated by using the air density at sea level, $\rho_{\text{air}} = 1.225 \cdot 10^{-3} \text{ g cm}^{-3}$. This value has been chosen as high as possible in order to provide an overestimation of the fraction of events detected by the FD and thus define a generation area for the Real Monte Carlo simulation safely larger than the effective sensitive area. A schematic view of an upward-going event that can be potentially detected by the FD is shown in Figure 4.6. The point P_{\max} corresponding to the position of the X_{\max} along the shower axis is inside the field of view of the FD. Summarizing, the event is considered detected by the FD if the distance d_{\max} between the FD site and the projection of P_{\max} on the generation area is less than $R_{\text{cut}}(E)$, where E is the energy of the primary proton. As shown in Figure

4.6, also an event with an exit point inside the portion of the generation area behind the FD site can produce a detectable shower.

4.4 Study of the detection efficiency

Given the geometric assumption and the trigger conditions described above, 10^9 events have been simulated in order to study the detection efficiency as a function of different simulation parameters and thus be able to define a generation area for the Real Monte Carlo simulation. The detection efficiency can be defined as:

$$\eta = \frac{N_{\text{trig}}}{N_{\text{sim}}}, \quad (4.9)$$

where N_{trig} is the number of events satisfying the trigger conditions and N_{sim} is the number of simulated events. In the histograms presented in the following sections, the definition of the detection efficiency has been applied bin by bin i.e. the number of triggered events in each given bin has been divided by the number of simulated events in that bin.

4.4.1 Dependence on the position of the exit point

The definition of the generation area for the Real Monte Carlo simulation is based mainly on the study of the detection efficiency as a function of the position of the exit point on the generation area performed by using the Fast Monte Carlo simulation. To identify the position of the exit point on the $200 \text{ km} \times 200 \text{ km}$ area shown in Figure 4.5(a), a 2D histogram with the positions (x, y) of the exit points, centered at the FD site, has been defined and filled with the corresponding detection efficiencies. This histogram has been operatively obtained by filling two separate 2D histograms with the number of events passing the trigger conditions and the number of simulated events, respectively, and then calculating the ratio between them. The procedure has been separately followed by considering both the case with only the standard FD field of view and the case with the addition of the HEAT telescope. The resulting histograms are shown in Figure 4.7. As expected, if also HEAT is considered, the detection efficiency increases because also upward-going events escaping the standard FD field of view can be detected. The detection efficiency can be safely considered equal to zero at more than 20 km behind the FD site and more than 50 km in front of it. Considering that each FD site is $\sim 30 \text{ km}$ far from the center of the SD array and that the sensitive area of the four FD sites overlaps because of their relative positions (see Figure 2.1), the generation area for the Fast Monte Carlo simulation has been chosen to be a square area of $100 \text{ km} \times 100 \text{ km}$ centered at the SD station closest to the center of the SD array. The choice of this generation area will be further justified by the distributions of the detection efficiency for different injection height intervals, shown in the next section as a function of the distance between the exit point and the FD site.

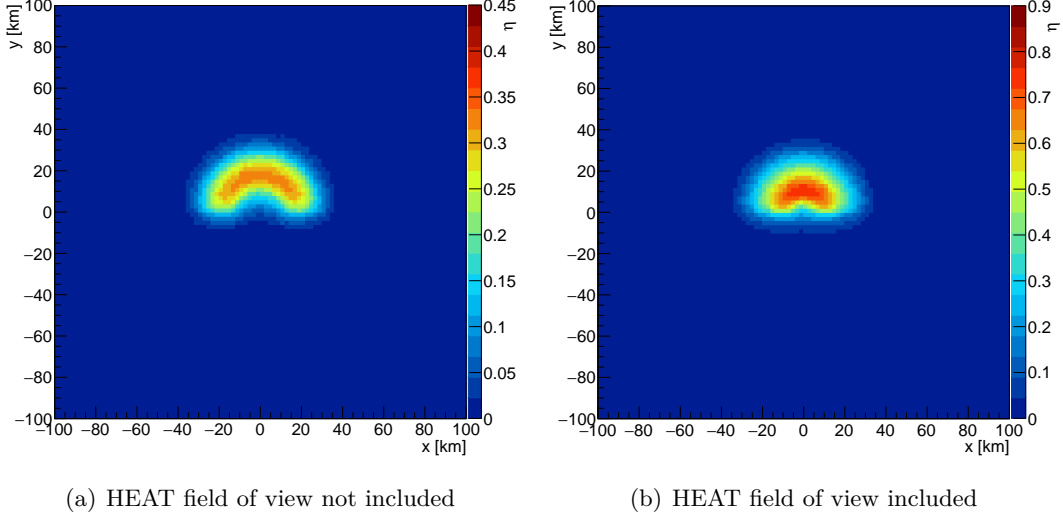


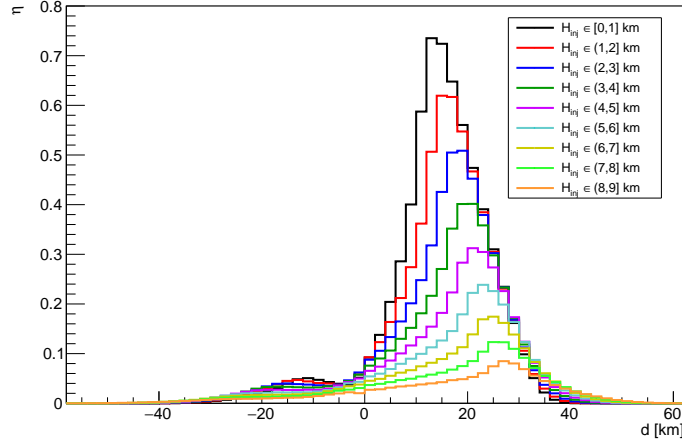
Figure 4.7: Detection efficiency as a function of the position (x, y) of the exit points on the generation area for the case with only the standard FD field of view considered (a) and the case with also the HEAT field of view considered (b). The negative values on the y -axis correspond to the portion of the generation area behind the FD site. The sensitive area extends between -20 km and 50 km on the y -axis. The detection efficiency increases if also the HEAT field of view is considered. Given the configuration of the four FD sites, a generation area of $100 \text{ km} \times 100 \text{ km}$ centered at the SD station closest to the center of the SD array has been chosen for the Real Monte Carlo simulation.

4.4.2 Dependence on the injection height

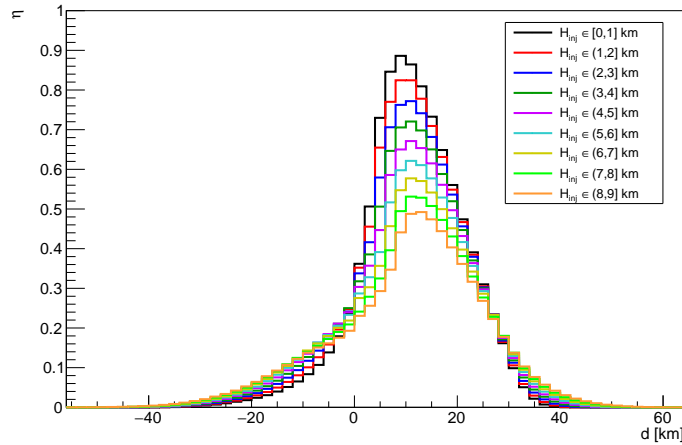
The detection efficiency as a function of the position of the exit point on the generation area depends on the height of the injection point. For a fixed value of the zenith angle, the higher the injection height, the larger the distance along the shower axis between the injection point and the exit point. Therefore, a triggering upward-going event with a high injection height is more likely to have an exit point far from the FD site. The detection efficiency as a function of the distance of the exit point from the FD site for different injection height intervals is shown in Figure 4.8. Again, the detection efficiency has been calculated by considering both the case with only the standard FD field of view and the case with the addition of the HEAT one. The distance of the exit point from the FD site has been defined as:

$$d = \frac{y}{|y|} \sqrt{x^2 + y^2}, \quad (4.10)$$

in order to have negative distances for exit points behind the FD site. The negative distances extend down to ~ -40 km because of the events exiting the ground with a



(a) HEAT field of view not included



(b) HEAT field of view included

Figure 4.8: Detection efficiency as a function of the distance between the exit point and the FD site considering only the generated and triggered events with an injection height H_{inj} in a specific interval. Both the case with only the standard FD field of view (a) and the case with the addition of the HEAT one (b) are shown. The inclusion of the HEAT field of view allows the FD site to be more sensitive to upward-going showers with higher injection heights.

negative value of y and a large value of $|x|$ (see Figure 4.7). For the case with only the standard FD field of view, the peak of the distribution shifts towards larger distances with the increase of the injection height, while the shift is less evident for the case with the addition of HEAT because of the increased field of view, which allows to detect

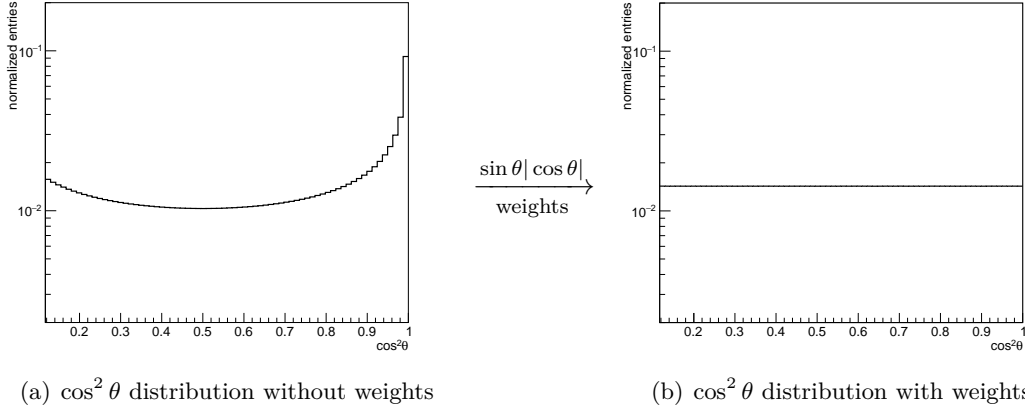
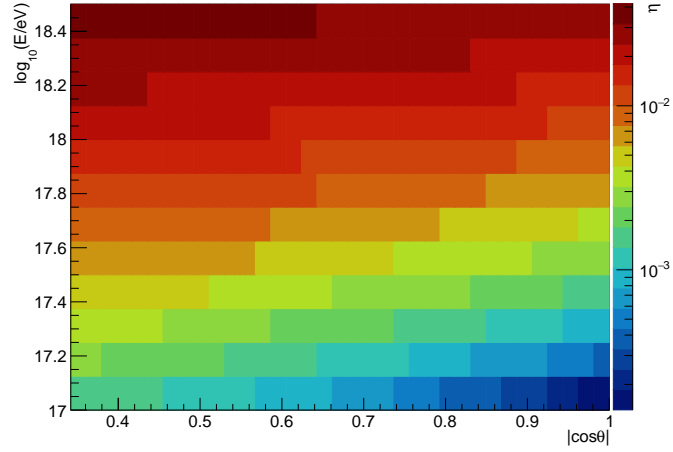


Figure 4.9: Distribution of $\cos^2 \theta$ before (a) and after (b) the weighting procedure. The distribution without weights (a) refers to the case with uniformly distributed zenith angles. The weighting procedure allows to have a flat distribution in $\cos^2 \theta$. Both distributions are normalized.

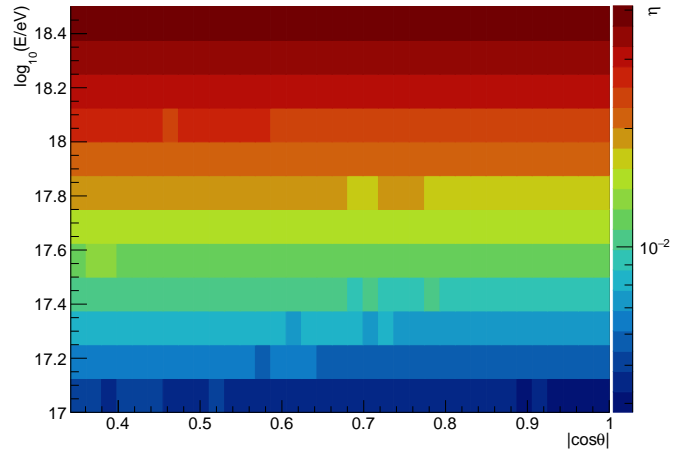
upward-going showers with higher injection heights. The distribution of the detection efficiency as a function of the distance between the exit point and the FD site further support the choice of the generation area for the Real Monte Carlo simulation as mentioned in the previous section.

4.4.3 Dependence on the primary energy and zenith angle

The distribution of the detection efficiency as a function of the primary energy and zenith angle plays a crucial role in the study of the sensitivity of the Pierre Auger Observatory to upward-going showers, since it is directly used in the calculation of the exposure, as described in the next section. Since the zenith angles have been uniformly generated in the region $[110, 180]^\circ$, the simulated events have been properly weighted in order to consider the case of an isotropic emergence i.e. azimuth angles and zenith angle generated respectively according to a uniform distribution and according to a $\cos^2 \theta$ distribution. This is accomplished by weighting each event with a factor $\sin \theta |\cos \theta|$. The distribution of $\cos^2 \theta$ before and after the weighting procedure is shown in Figure 4.9. After performing the weighting procedure, the distribution is correctly flat in $\cos^2 \theta$. Since the exposure is usually given as a function of the primary energy E , the dependence of the detection efficiency on this quantity is also important. In particular, the exposure as a function of the energy is obtained by performing an integration over θ for each value of the energy E (see section 4.5.1). To make the exposure calculation easier, the dependence on the zenith angle has been expressed in terms of $\cos \theta$. The detection efficiency as a function of $\log_{10} (E/\text{eV})$ and $|\cos \theta|$ is shown in Figure 4.10. As usual, both the case with only the standard FD field of view and the case with the addition of the HEAT telescopes have been considered. In contrast to the previous



(a) HEAT field of view not included



(b) HEAT field of view included

Figure 4.10: Detection efficiency as a function of $\log_{10}(E/\text{eV})$ and $|\cos\theta|$ for the case with only the standard FD field of view (a) and the case with the addition of the HEAT one (b). For a given primary energy, the addition of the HEAT field of view increases the sensitivity of the FD site to upward-going showers with larger zenith angles i.e. more vertical upward-going showers. It is important to notice that the range of the z-axis is different for (a) and (b).

cases, the detection efficiency for each E and $\cos\theta$ has been computed regardless of the position of the exit points on the generation area.

4.5 Exposure to upward-going showers

The exposure to upward-going showers defines the capability of the Pierre Auger Observatory to detect such a class of events and plays an important role in the comparison of our results with those from other experiments. Furthermore, it is needed in the calculation of the upper limit that can be set if no candidate events are observed. In the following sections, a general description of the exposure calculation will be presented first and then a rough estimate of the exposure to upward-going showers obtained by using the results from the Fast Monte Carlo simulation will be provided. This procedure will be also applied in Chapter 5 using the Real Monte Carlo simulation.

4.5.1 Exposure calculation

The FD exposure as a function of the energy, $\varepsilon(E)$, is calculated as:

$$\varepsilon(E) = A(E) \cdot \Delta T, \quad (4.11)$$

where A is the Monte Carlo time-averaged FD aperture, ΔT is the solar time (i.e. the 14 years of operation of the FD) and E is the primary energy. The FD aperture is defined as:

$$A(E) = \int_{\Omega} S_{\text{eff}}(E, \theta) \cos \theta d\Omega, \quad (4.12)$$

where Ω is the solid angle, θ is the zenith angle, $\cos \theta$ takes into account that the generation area is a flat surface and $S_{\text{eff}}(E)$ is the effective area, that is defined as:

$$S_{\text{eff}}(E, \theta) = \int_{S_{\text{gen}}} \eta(E, \theta) \cdot dS. \quad (4.13)$$

Here S_{gen} is the surface area on the ground plane over which exit points have been generated and $\eta(E, \theta)$ is the Monte Carlo time-averaged detection efficiency at a specific energy and zenith angle. Generalizing the definition in Eq. 4.9, the detection efficiency is calculated as the ratio of the number of events that pass the selection criteria over the total number of generated events:

$$\eta(E, \theta) = \frac{n_{\text{selected}}(E, \theta)}{n_{\text{generated}}(E, \theta)}. \quad (4.14)$$

By inserting S_{eff} from Eq. 4.13 into Eq. 4.12, the FD aperture can be rewritten as:

$$A(E) = S_{\text{gen}} \cdot \int_{\theta} \eta(E, \theta) \cos \theta d \cos \theta \cdot \int_{\phi} d\phi, \quad (4.15)$$

where the zenith angle range is $\theta \in [110, 180]^\circ$ and the azimuth angle range is $\phi \in [0, 360]^\circ$. Following the same approach as [152], the FD exposure at a specific energy is then given by:

$$\varepsilon(E) \simeq 2\pi \cdot S_{\text{gen}} \cdot \Delta T \cdot \sum_i \eta(E, \cos \theta_i) \cdot \cos \theta_i \cdot \Delta \cos \theta_i. \quad (4.16)$$

This expression can be directly used to calculate the exposure if the detection efficiency is taken from a histogram defined in the same way as those shown in Figure 4.10. This clarifies also the reason why the dependence of the detection efficiency on θ has been expressed in terms of $\cos \theta$.

4.5.2 A first estimate of the exposure

A first estimate of the exposure of the Pierre Auger Observatory to upward-going showers can be given by using the results from the Fast Monte Carlo simulation. Since the Fast Monte Carlo simulation does not include the limited FD on-time, Eq. 4.16 has to be multiplied by a factor ϵ_{DC} that is assumed to be roughly $\epsilon_{\text{DC}} = 0.14$. The first step in the estimation of the total exposure (i.e. the exposure obtained by considering the four FD sites of the Pierre Auger Observatory) with the Fast Monte Carlo simulation consists in the calculation of the exposure of a single FD site for both the case with and without HEAT. The corresponding exposures, ϵ_{st} and $\epsilon_{\text{st+HE}}$, are given by:

$$\epsilon_{\text{st}}(E) \simeq 2\pi \cdot S_{\text{gen}} \cdot \Delta T \cdot \sum_i \epsilon_{\text{DC}} \cdot \eta_{\text{st}}(E, \cos \theta_i) \cdot \cos \theta_i \cdot \Delta \cos \theta_i, \quad (4.17)$$

$$\epsilon_{\text{st+HE}}(E) \simeq 2\pi \cdot S_{\text{gen}} \cdot \Delta T \cdot \sum_i \epsilon_{\text{DC}} \cdot \eta_{\text{st+HE}}(E, \cos \theta_i) \cdot \cos \theta_i \cdot \Delta \cos \theta_i, \quad (4.18)$$

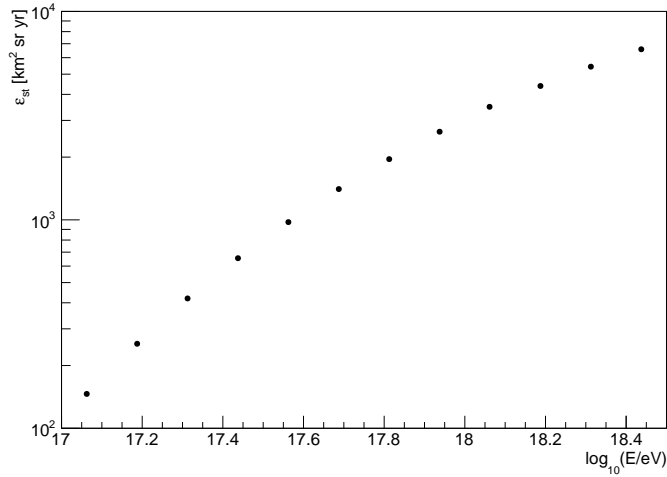
where $\eta_{\text{st}}(E, \cos \theta_i)$ and $\eta_{\text{st+HE}}(E, \cos \theta_i)$ are taken respectively from Figure 4.10(a) and Figure 4.10(b), $S_{\text{gen}} = 200 \text{ km} \times 200 \text{ km}$ and $\Delta T = 14 \text{ yr}$.

The total exposure of the Pierre Auger Observatory is then calculated by considering the FD consisting of three sites (Los Leones, Los Morados and Loma Amarilla) with the standard FD field of view and one site (Coihueco) with the additional HEAT telescopes. Therefore, the total exposure can be computed as:

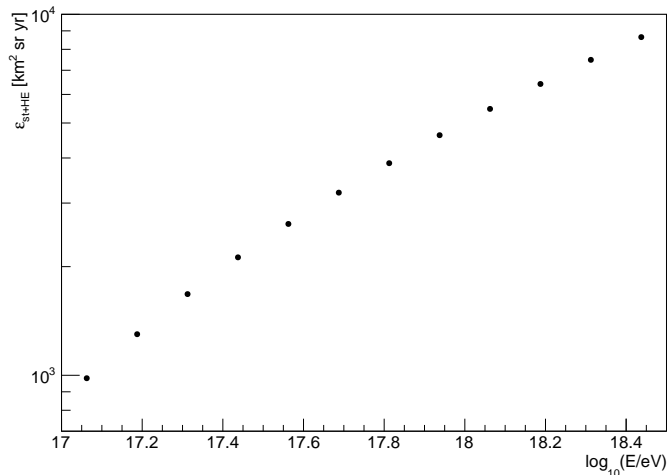
$$\epsilon_{\text{tot}}(E) = 3 \epsilon_{\text{st}}(E) + \epsilon_{\text{st+HE}}(E). \quad (4.19)$$

In this expression, the four FD sites are considered to give an independent contribution to the exposure. Considering also the assumptions used in the Fast Monte Carlo simulation, this will result in an overestimation, because the overlap between the fields of view of the the different FD sites is not taken into account. Furthermore, no quality selection criteria are defined in the Fast Monte Carlo simulation, resulting in an additional overestimation of the exposure with respect to that computed with the Real Monte Carlo simulation and all the selection criteria properly applied (see Chapter 5). It is straightforward to notice that the increase of the generation area (e.g. to $200 \text{ km} \times 200 \text{ km}$) is not effective. In fact, for very far away showers the detection efficiency rapidly decreases, giving a negligible contribution to the total exposure. For this reason, an optimal definition of the generation area is needed when a Real Monte Carlo simulation is performed.

The dependence of the exposures ϵ_{st} and $\epsilon_{\text{st+HE}}$ on the primary energy is shown in Figure 4.11, while the total exposure is shown in Figure 4.12. As already mentioned, a detailed calculation of the exposure of the Pierre Auger Observatory to upward-going



(a) HEAT field of view not included



(b) HEAT field of view included

Figure 4.11: Exposure of a single FD site as a function of the energy for the case with only the standard FD field of view (a) and the case with the addition of the HEAT one (b). The uncertainties on the values of the exposure are also included, but they are too small to be appreciated with the scale used for the y-axis. The addition of the HEAT field of view allows to significantly increase the sensitivity to upward-going showers at low energies.

showers requires a Real Monte Carlo simulation to be performed. However, the simple assumptions used in the Fast Monte Carlo simulation allowed us to simulate a large number of events in a large area and thus define an effective generation area for the

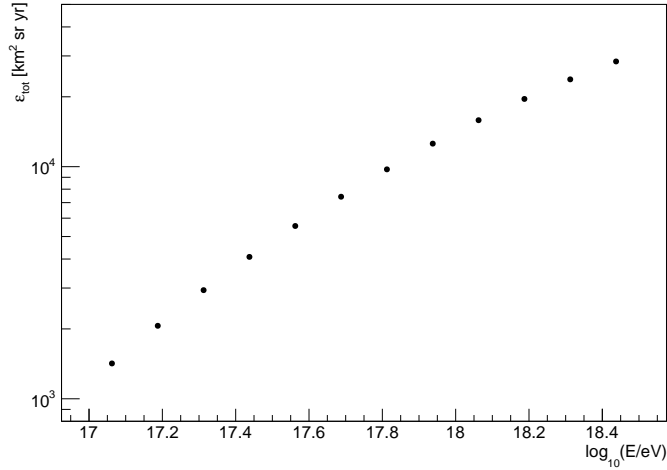


Figure 4.12: Total FD exposure obtained from those shown in Figure 4.11(a) and Figure 4.11(b), as described in the text. Also in this case, the uncertainties on the values of the exposure are included, but they can not be appreciated. Given the assumptions used in the fast Monte carlo simulation and in the exposure calculation, this estimate is an overestimation of the real exposure, as will be confirmed in Chapter 5.

Real Monte Carlo simulation. This helped both to save computing time and to increase the statistics of the events that have a higher chance to be detected by the FD. The results from the Real Monte Carlo simulation, together with those from the search for upward-going showers with the FD of the Pierre Auger Observatory, will be described in the next chapter.

CHAPTER 4. A FAST MONTE CARLO SIMULATION FOR UPWARD-GOING
SHOWERS

Chapter 5

Search for upward-going showers with the FD

Given its operation time and wide field of view, the FD of the Pierre Auger Observatory can be used in monocular mode to search for upward-going showers, which are a possible interpretation of the two anomalous events recently reported by the ANITA Collaboration (see section 3.2). As already mentioned, the energies and the elevation angles of these events appear to be in tension with the predictions of the SM. For this reason, within the Pierre Auger Collaboration we performed a generic search for cosmic-ray-like upward-going showers with the FD. I studied the sensitivity of the FD to upward-going showers with a Real Monte Carlo simulation of upward-going events distributed in the energy and zenith angle regions of interest. The potential background for this search consists of cosmic-ray induced air showers with specific geometric configurations which can be reconstructed erroneously as upward-going events in a monocular reconstruction. I simulated together with my Auger colleagues a huge library of downward-going events to which a monocular event reconstruction was applied. Moreover, a sample of 10% of the available FD data (burn data sample) has been used to develop a set of cuts to reject laser events. Applying these cuts together with those defined with simulations I have quantified the signal efficiency as well as the background expectation in the blinded data sample.

This chapter deals with the description of the generic search for upward-going showers performed with the FD of the Pierre Auger Observatory. Most of the results described in this chapter have been discussed in an oral contribution I gave to the 37th International Cosmic Ray Conference (ICRC) and included in the corresponding proceedings [140].

5.1 Signal simulation

To calculate the FD exposure with a Real Monte Carlo simulation, upward-going showers have been simulated with CONEX [153] and reconstructed within the Offline Framework [154]. CONEX is a simulation program that allows to simulate EAS in an

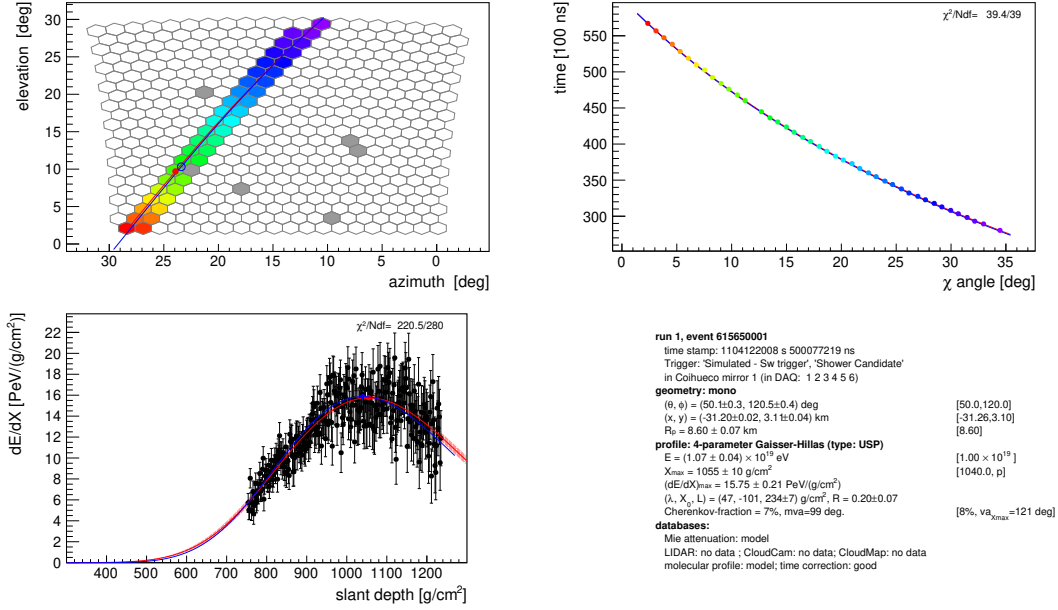


Figure 5.1: Downward-going proton induced shower simulated with CONEX and reconstructed within the Offline. The event has been detected by one of the telescopes of Coihueco and is shown as seen in the viewer of the Offline. The activated pixels on the camera of the telescope (top left panel), the arrival time of the light on the single pixels as a function of their χ (top right panel), the reconstructed longitudinal profile of the shower (bottom left panel) and the parameters from the reconstruction (bottom right panel) are shown. The colors in the top right and top left panel refer to the progression of the arrival time of the light (blue for early pixels, red for late pixels). In the bottom right panel, the values used in the simulation are displayed in square brackets.

affordable computing time, while the Offline Framework is the simulation and reconstruction software used by the Pierre Auger Collaboration. The simulation has been performed approximating the start of the shower with a single proton, and it can be adapted to fit other scenarios. SIBYLL 2.3c and UrQMD 1.3 have been used as hadronic interaction models at high and low energies, respectively (see Appendix B). Simulations indicate that the FD has negligible efficiency for shower energies below $10^{16.5}$ eV and this study has been performed considering showers in the restricted calorimetric energy interval $\log_{10}(E_{\text{cal}}/\text{eV}) \in [16.5, 18.5]$, within which the ANITA events comfortably fall. In contrast to the approach used in the Fast Monte Carlo simulation, the energy interval is expressed in terms of calorimetric energy for a more direct comparison with the results from ANITA. Showers of higher energies could of course be also potentially observed. To be able to cover that range of calorimetric energies, the primary has been sampled in the region $\log_{10}(E/\text{eV}) \in [16.5, 19]$ according to an energy distribution

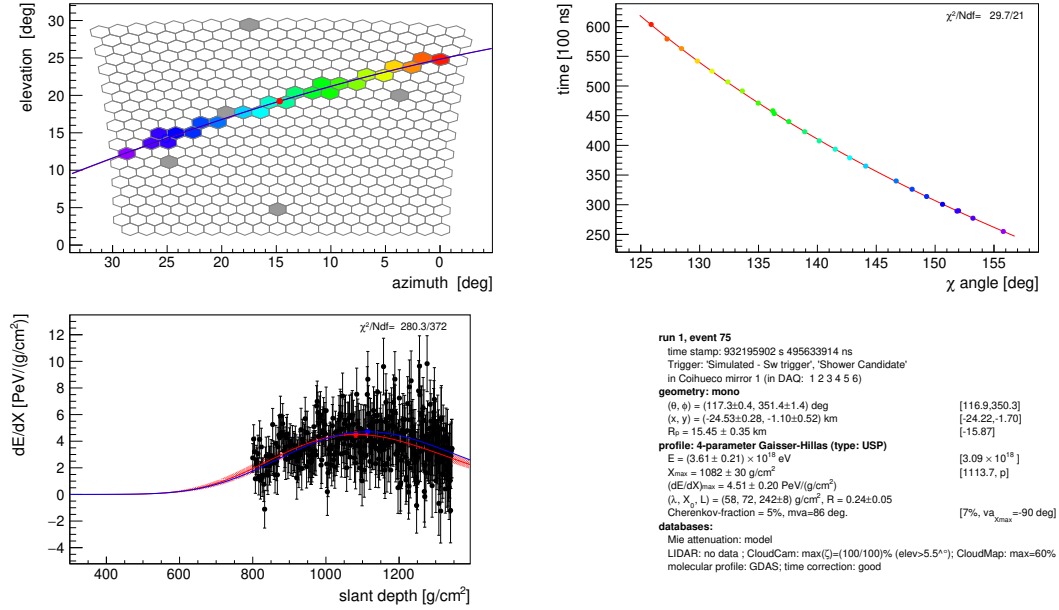


Figure 5.2: Upward-going proton induced shower simulated with CONEX and reconstructed within the Offline. Also in this case, the event has been detected by one of the telescopes of Coihueco and is shown as seen in the viewer of the Offline. The same panels as Figure 5.1 are shown. The progression of the arrival time of the light on the single pixels is inverted with respect to that of the event shown in Figure 5.1.

of E^{-1} , corresponding to an uniform distribution in $\log_{10}(E/\text{eV})$, and assuming an isotropic distribution of events. As already mentioned in Chapter 4, only zenith angles in the range $[110, 180]^\circ$ have been considered. Referring to Figure 4.1, the height of the point of first interaction of the primary particle, H_{fi} , has been generated in the region $[0, 9]$ km above the ground altitude of the Observatory according to a uniform distribution. Here, the point of first interaction has been considered in place of the injection point to make easier to apply the results of this search to other physical scenarios. However, simulations have been set in order to cover also the injection height region $[0, 9]$ km for further analyses. As discussed in Chapter 4, the results from the Fast Monte Carlo simulation have been used to define a square generation area of $100 \text{ km} \times 100 \text{ km}$ centered at the SD station closest to the center of the array. This area extends up to ~ 20 km behind each FD site, allowing to simulate also particles whose exit point is located behind the field of view of a telescope. The events have been uniformly sampled inside this area. All the FD configurations and their time variability during the 14 years of operation have been taken into account in the Real Monte Carlo simulation [152]. This allows to directly include the on-time fraction of the telescopes in the calculation of the detection efficiency and thus in the exposure calculation. The signal simulation has been organized in different productions, each one with $2.5 \cdot 10^5$ events

in each 0.25 sub-range of $\log_{10}(E/\text{eV})$. Eight productions have been performed considering the full $\log_{10}(E/\text{eV})$ range. In order to increase the statistics at low energies, wo additional productions have been done in the region $\log_{10}(E/\text{eV}) \in [16.5, 17.5]$. A total number of 2.2×10^7 events have been simulated. The reconstruction of downward-going and upward-going showers are shown in Figure 5.2 and Figure 5.1, respectively. The upward-going shower can be clearly identified from the progression of the arrival time of the light on the single pixels of the camera of the telescope, which is inverted with respect to that of the downward-going shower.

5.1.1 Detection efficiency and exposure without selection cuts

The detection efficiency from the Real Monte Carlo simulation automatically takes into account the on-time fraction evolution of the telescopes. Furthermore, CONEX showers allow for a more accurate description of the physics of upward-going showers with respect to that used in the Fast Monte Carlo simulation. These features result in a detailed estimate of the exposure, but also in the increase of the computing time required by the simulation. The total number of simulated events with the Real Monte Carlo, in fact, is much lower than that of the Fast one.

The exposure has been calculated using the expression in Eq. 4.16, where the detection efficiency $\eta(E, \cos\theta_i)$ does not need to be multiplied by the FD duty cycle, as it is already included in the detector response simulation. To allow for a comparison with the results from the Fast Monte Carlo shown (see Figure 4.12), the exposure has been studied as a function of the simulated primary energy instead of the simulated calorimetric energy in the restricted region $\log_{10}(E/\text{eV}) \in [17, 18.5]$. All the events detected by the FD have been considered as selected events, with no selection criteria applied. The exposure obtained from the Real Monte Carlo, together with the detection efficiency that has been used in its calculation, is shown in Figure 5.3. As expected, the exposure from the Real Monte Carlo simulation is much smaller than that from the Fast one. It should be noted that the presence of the FD trigger, which is not considered in the Fast Monte Carlo simulation, contributes to the overestimation of the exposure together with the all the other approximation discussed in Chapter 4. The behaviour of the detection efficiency as a function of $\log_{10}(E/\text{eV})$ and $|\cos\theta|$, shown in Figure 5.3(a), is similar to that obtained with the Fast Monte Carlo simulation for one FD site, confirming the prediction capability of this fast approach.

Hereinafter, the exposure will be expressed as a function of the simulated calorimetric energy. Following the same procedure used to obtain the plots shown in Figure 5.3, the exposure as a function of the simulated calorimetric energy for the case of not applied selection criteria has been derived. The result, together with the detection efficiency, is shown in Figure 5.4. The exposure reported in Figure 5.4(b) can be considered a benchmark, since it represents the maximum achievable exposure to upward-going showers. The introduction of selection criteria, in fact, will reduce the number of selected events with a consequent decrease in the exposure.

Another plot that can be used to make a comparison between the results from the Real Monte Carlo simulation and those from the Fast one is the detection efficiency

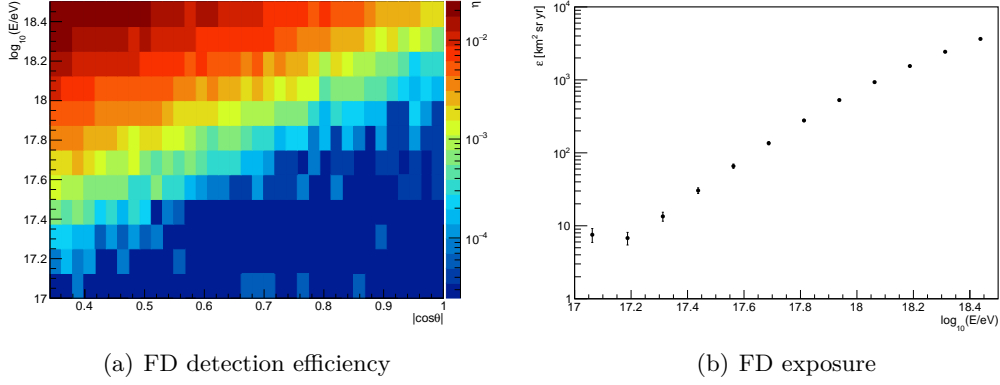


Figure 5.3: FD detection efficiency as a function of $\log_{10}(E/\text{eV})$ and $|\cos\theta|$ (a) and FD exposure as a function of the simulated primary energy (b), both obtained from the Real Monte Carlo simulation without applying any selection cut.

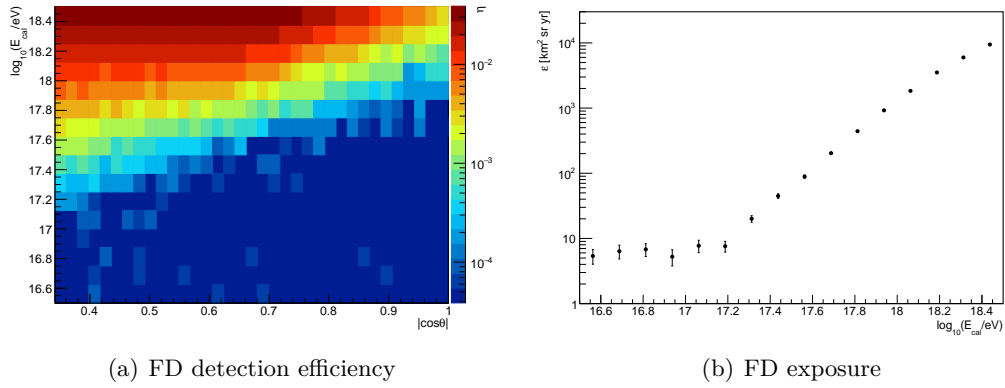


Figure 5.4: FD detection efficiency as a function of $\log_{10}(E_{\text{cal}}/\text{eV})$ and $|\cos\theta|$ (a) and FD exposure as a function of the simulated calorimetric energy (b), both obtained from the Real Monte Carlo simulation without applying any selection cut. The Pierre Auger Observatory is sensitive to upward-going showers also at low calorimetric energies, at least when no selection cuts are applied.

as a function of the position of the exit points on the generation area. This plot is shown in Figure 5.5. Also in this case, only the events with a simulated primary energy in the region $\log_{10}(E/\text{eV}) \in [17, 18.5]$ have been considered, with no selection cuts applied. By comparing this result with that obtained for one FD site with the Fast Monte Carlo simulation (see Figure 4.7), it can be noted that the geometrical behaviour of the detection efficiency in Figure 5.5 for the single FD sites is similar to that predicted by the Fast Monte Carlo simulation. The increase in the detection efficiency observed in front of the Coihueco site is due to the presence of HEAT, whose

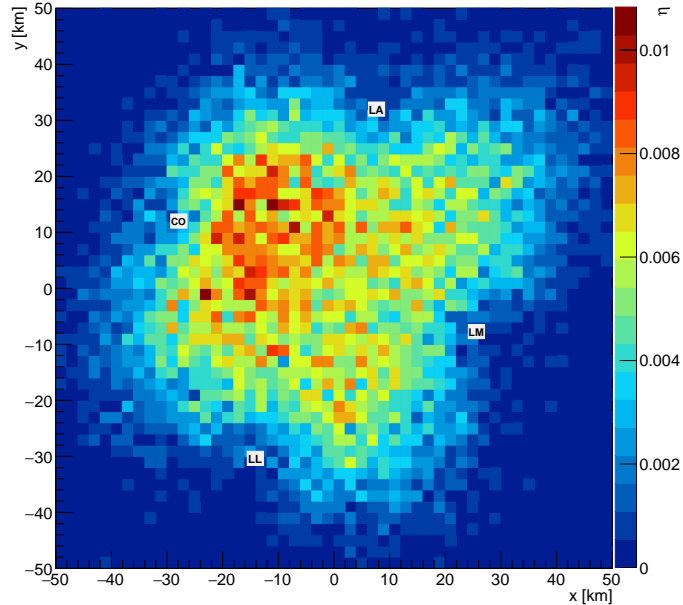


Figure 5.5: FD detection efficiency as a function of the position (x, y) of the exit points on the generation area of $100 \text{ km} \times 100 \text{ km}$ used in the Real Monte Carlo simulation. The point $(0, 0)$ corresponds to the position of the SD station closest to the center of the SD array. Also the positions of the four FD sites, Los Leones (LL), Los Morados (LM), Loma Amarilla (LA) and Coihueco (CO), are shown. The geometrical configuration of the FD reflects the one shown in Figure 2.1. The plot has been obtained considering only the events with a simulated primary energy in the region $\log_{10}(E/\text{eV}) \in [17, 18.5]$, without applying any selection cut.

geometrical configuration is shown in Figure 2.1.

5.2 Background simulation

In this analysis FD data from a single location is typically the only one used for the reconstruction (monocular reconstruction). No SD data is required as upward-going showers are unlikely to trigger the SD. Without this information downward-going events with specific geometries could be incorrectly reconstructed as upward-going events and vice-versa. An example is shown in Figure 5.6. The signal coming from point P_1 arrives before that coming from point P_2 because the impact point is behind the telescope mimicking an upward-going event. To study background events, a dedicated and extensive simulation of downward-going events has been performed. The FD is a volumetric detector, so the cores have been sampled in a sphere of radius 90 km centered at the center of the SD array rather than on a surface. This simulation geometry, which

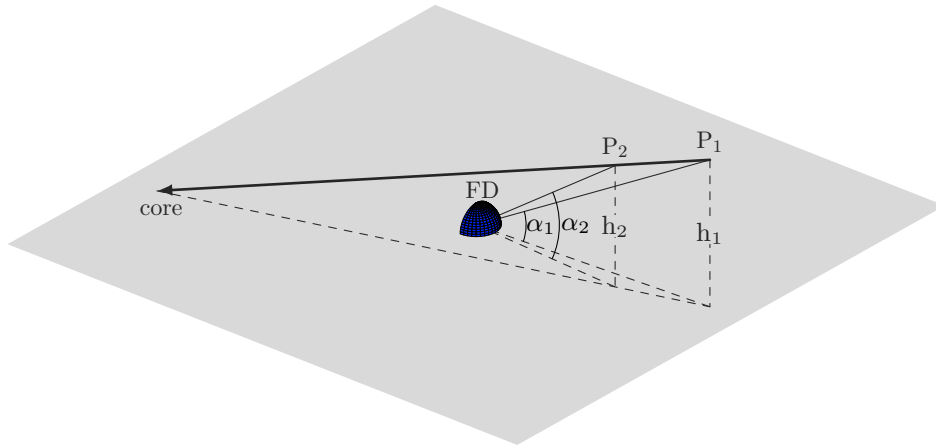


Figure 5.6: Schematic view of the geometry of a downward-going event that is reconstructed as an upward-going event. For the two points P_1 and P_2 on the shower axis $\alpha_1 < \alpha_2$ and $h_1 > h_2$. The signal from P_1 reaches the FD before the signal from P_2 and the event can be reconstructed as an upward-going event. Figure from [140].

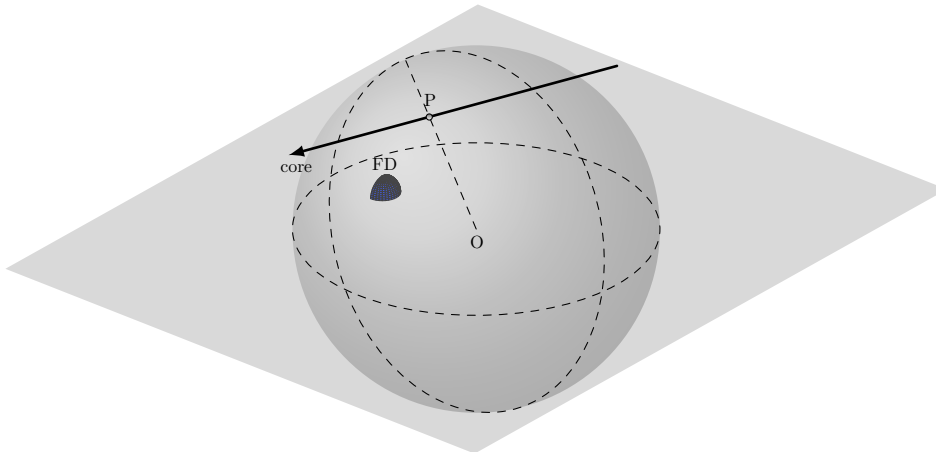


Figure 5.7: Generation geometry used for the background simulation. The cores P of the downward-going showers are simulated in a sphere of radius 90 km centered at the center of the SD array O and then projected onto the ground along the direction of the shower axis. This allows to simulate also showers with a core far away from the FD.

have been implemented in the Offline, allows to simulate also downward-going showers whose core is far away from the FD but that can potentially produce a background signal, as shown in Figure 5.7. Downward-going events have been simulated according to an energy distribution of $E^{-2.2}$ in the region $\log_{10}(E/\text{eV}) \in [17, 20]$ and then, during the analysis, properly re-weighted according to the cosmic ray energy spectrum

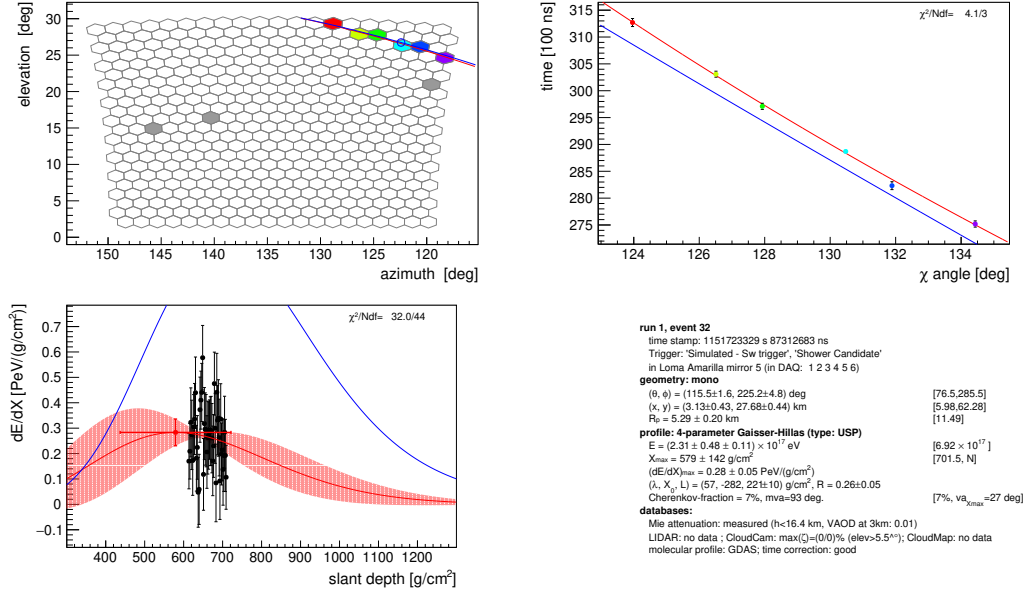


Figure 5.8: A downward-going shower simulated with a zenith angle smaller than 90° ($\theta = 76.5^\circ$) and reconstructed as an upward-going shower ($\theta = 115.5^\circ$) in the monocular reconstruction defined in section 2.2.4.

measured by the Pierre Auger Observatory (see section 1.2). An isotropic distribution of events has been assumed with a zenith angle $\theta \in [0, 90]^\circ$. Helium, nitrogen and iron nuclei, together with protons, have been considered as primary particles. The hadronic models at high and low energies used for the background simulations are the same as for the signal simulations (see section 5.1). An example of a simulated downward-going shower mis-reconstructed as an upward-going shower in the monocular reconstruction defined in section 2.2.4 is shown in Figure 5.8. The background simulations have been used to study the topology of the background events and define selection criteria to discriminate between signal events and false positives induced by a small fraction of regular cosmic ray showers ($< 0.1\%$). To achieve this target, each event of both signal simulation and background simulation has been reconstructed using, in addition to the monocular reconstruction defined in section 2.2.4, the Profile Constrained Geometry Fit reconstruction, whose details will be described in the next section.

5.3 The Profile Constrained Geometry Fit reconstruction

The monocular reconstruction described in section 2.2.4 may suffer, as already mentioned, of a degeneracy between R_p and χ_0 . This degeneracy can be removed using the reconstruction based on the so-called Profile Constrained Geometry Fit (PCGF) reconstruction [156]. It requires the profile of the energy deposit to match the approximately universal characteristics of air showers induced by most primaries, which are

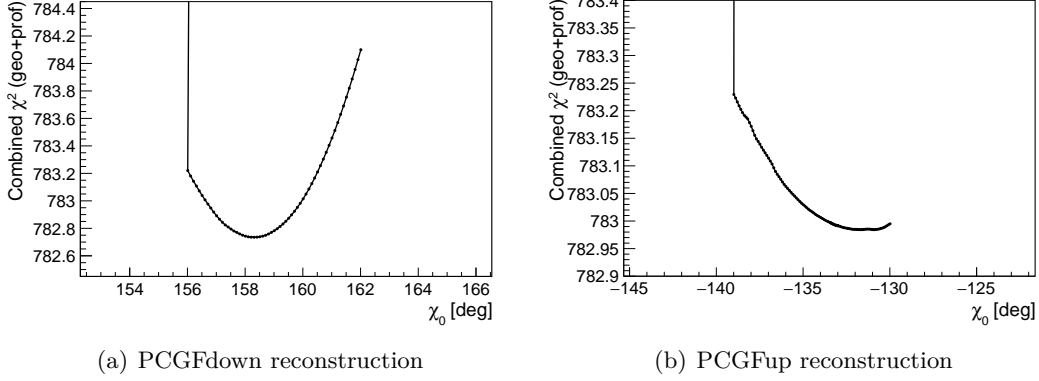


Figure 5.9: Scans in χ_0 performed using the PCGFdown reconstruction (a) and the PCGFup reconstruction (b) on the background event shown in Figure 5.8. For clarity, only the χ_0 region where the minimum χ^2 has been found is shown for both the scans. For this event, the two reconstructions result in $L_{\text{down}} > L_{\text{up}}$.

described by a Gaisser-Hillas function as reported in Eq. 2.11. The PCGF reconstruction is performed by scanning χ_0 and calculating for each of its values both R_p and t_0 from Eq. 2.8 by linear regression. For each defined geometry, the measured light flux is compared with the predicted ones obtained from each combination of $(\frac{dE}{dX})_{\text{max}}$, X_0 , X_{max} and λ . The agreement between the defined geometry and each assumption is quantified through a likelihood that consists of parts from the time fit of Eq. 2.8, constraints on the Gaiser-Hillas parameters, and the measured light flux [156]. The geometry corresponding to the maximum likelihood, or equivalently to the minimum χ^2 , is chosen and then the profile of the energy deposit is fine-tuned.

In the analysis performed within the search for upward-going showers, the PCGF reconstruction is run in two distinct modes i.e. downward and upward. The downward mode (PCGFdown reconstruction) searches for the maximum value of the likelihood in the χ_0 region corresponding to downward-going showers, while the upward one (PCGFup reconstruction) performs the same search in the χ_0 region corresponding to upward-going showers. This results in two independent values of the maximum likelihood, L_{down} and L_{up} respectively from the PCGFdown and the PCGFup reconstructions. By comparing L_{down} with L_{up} , it is possible to discriminate between events that are more likely to be downward-going and vice-versa. As an example, both the scans in χ_0 performed using the PCGFdown and the PCGFup reconstructions on the event shown in Figure 5.8 are shown in Figure 5.9. For this event, which is a background one, the minimum χ^2 from the PCGFdown reconstruction is smaller than that from the PCGFup one, resulting in $L_{\text{down}} > L_{\text{up}}$. If the two reconstructions are performed on the signal event shown in Figure 5.2, on the contrary, the result is $L_{\text{down}} \ll L_{\text{up}}$, as shown in Figure 5.10. Then, a selection criteria based on L_{down} and L_{up} can be defined and used to discriminate between signal events and background ones. This will

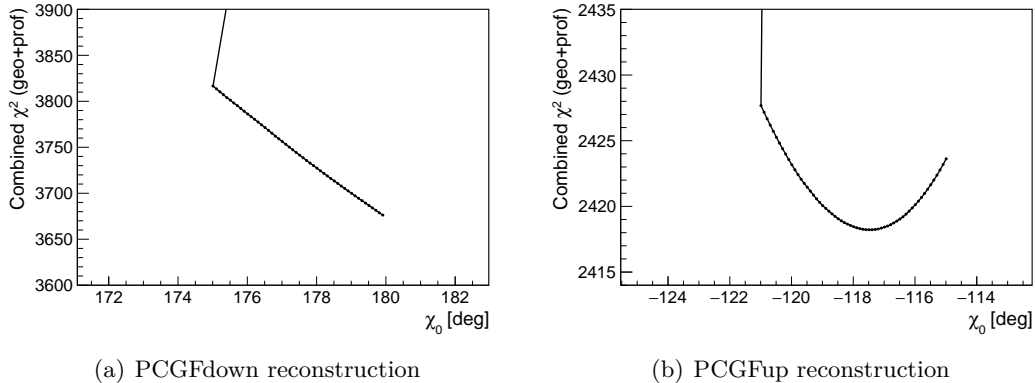


Figure 5.10: Scans in χ_0 performed using the PCGFdown reconstruction (a) and the PCGFup reconstruction (b) on the signal event shown in Figure 5.2. Also in this case, only the χ_0 region where the minimum χ^2 has been found is shown. In contrast to the background event of Figure 5.8, this event is characterized by $L_{\text{down}} \ll L_{\text{up}}$.

be described in the next sections.

5.4 Data cleaning and event selection criteria

Of particular relevance for this analysis is the identification of laser shots in the data sample. As mentioned in section 2.2.5, the FD requires continuous monitoring of the atmosphere and millions of laser shots are being fired from different positions during data acquisition for this purpose. These are upward-going events and constitute a background for this search. Laser shots are usually recorded and stored so that they can be easily removed while performing the analysis. However, in few cases they are not properly labelled, and so they can produce false positives. To study and properly identify such events, a sample made of the 10% of the available FD data (burn data sample) has been used. In particular, the laser identification has been performed by exploiting the features of the lidar shots and CLF and XLF shots. The lidar shots are fired at a repetition rate of 333 Hz, while the CLF and XLF shots are fired at a known position and thus can be identified using their SDP azimuth angle. Excesses of events have been searched for in 2D histograms of GPS microsecond modulus 3000 and SDP azimuth angle. This provided the input to define a set of selection criteria to be applied to the event time windows and exit point position at ground in which these laser events are expected. By following this procedure, the burn data sample has been cleaned from all laser events. In addition to the selection criteria defined for the laser identification, another set of selection criteria has been defined. The latter preserves the quality of both reconstruction and atmospheric conditions and thus reduce the mis-identification of downward-going and upward-going air showers. This set has been tested on both signal and background simulations.

The selection criteria defined for this analysis can be grouped in two classes depending on the reconstruction they are applied on. The first one includes all the pre-selection criteria that have been applied on the monocular reconstruction described in section 2.2.4, while the second one consists of all the criteria that have been used on the variables coming from the PCGFup reconstruction. The full set of selection cuts is listed in the next subsections.

5.4.1 Pre-selection criteria applied on the monocular reconstruction

To speed up the analysis, which requires all the FD data from 14 years of operation to be processed, data have been preliminarily analysed using the monocular reconstruction described in section 2.2.4, without performing any reconstruction of the energy deposit profile. A set of pre-selection criteria have been defined and applied on this reconstruction to select potential candidate events. The PCGF reconstruction is then performed only on these potential candidates, since it requires a larger amount of computing time. The pre-selection criteria include also those defined to reject laser events and those used to ensure the good quality of the atmospheric conditions. These criteria have been then applied also to the monocular reconstruction of the events for both the signal and background simulation. The pre-selection criteria are the following:

- **nAxisPixels > 5**: the minimum number of pixels used in the axis fit is required to be greater than 5. This is a minimum requirement to allow for a good reconstruction of the shower axis.
- **ZenithFD > 90°**: the zenith angle from the monocular reconstruction is required to be greater than 90°. This cut allows to select candidate upward-going events.
- **!SDPLaserCut**: the SDP azimuth angle of the event is required not to match those of the CLF and XLF. This cut allows to remove CLF and XLF shots from data.
- **!isLidar333Hz**: the event is required not to occur in the time and SDP azimuth angle windows identified during the data cleaning. This cut allows to remove lidar shots from data.
- **!isLidar20Hz**: this cut is similar to the previous one, but it has been introduced to reject the lidar shots fired at a repetition rate of 20 Hz in 2006 at Coihueco site.
- **!isDataBurst**: this cut has been introduced to reject the residual, non-lidar bursts of events in the burn data sample occurring at the same time, FD site and telescope.
- **hasMieDatabase**: the Mie database, which is needed in order to take into account the Mie scattering in the reconstruction (see section 2.2.5), is required to be available.

- **VAOD < 0.1:** the VAOD at a reference height of 4.5 km, which quantifies the amount of aerosols in the atmosphere, is required to be smaller than 0.1. This cut allows to have a good atmospheric transparency.
- **good10MHzCorrection:** a good correction of the 10MHz oscillator, which is used to synchronize all the detectors, is required.

5.4.2 Selection criteria applied on the PCGFup reconstruction

Once the pre-selection criteria have been applied on the monocular reconstruction, a set of quality selection criteria is defined for the PCGFup reconstruction:

- **Xmax > 0:** the reconstructed X_{\max} is required to be greater than zero. Only events with a reconstructed X_{\max} are selected.
- **lgEcalFD > 16.5:** the reconstructed calorimetric energy is required to be greater than $10^{16.5}$ eV, which is the lower bound of the calorimetric energy region of interest.
- **ZenithFD > 110°:** the reconstructed zenith angle is required to be greater than 110° . Only events with a reconstructed zenith angle in the zenith angle region of interest are selected.
- **depthTrackLength > 80 g cm⁻²:** the track length in depth is required to be greater than 80 g cm^{-2} . This cut allows to reject events whose track is too short.
- **cloudCutNoHeight hard:** the absence of clouds is required, without checking if the event occurs below the cloud height. This cut allows to reject events occurring when the sky is not clear.
- **FLToverTimeFitPix < 3:** the ratio between the number of pixels of the first level trigger and the number of pixels used in the time fit is required to be smaller than 3. This cut allows to reject events that are too noisy.
- **badFDPeriodRejection:** the event is required not to occur during periods with bad VAOD profiles, which negatively affect the shower reconstruction. This cut has been used also to reject events occurring during nights with roving lidar campaigns, which are conducted to perform absolute FD calibration and FD testing.
- **timeFitPixOut < 4:** the number of pixels used in the time fit with an arrival time outside the arrival time window of the reconstructed light flux profile at the telescope aperture is required to be lower than 4. The event is rejected if a high number of pixels outside the reconstructed light flux has been used in the time fit.

- **$-2\log(\mathbf{Lup}) < 5000$** : the minimum combined χ^2 from the PCGFup reconstruction is required to be lower than 5000. This cut allows to reject events with a bad PCGFup reconstruction.
- **$\mathbf{arcIsolatedPixels} < 6^\circ$** : the angular distance between the pointing directions of two consecutive triggered pixels is required to be smaller than 6° . This cut allows to reject events with isolated triggered pixels, which can negatively affect the reconstruction.
- **$\mathbf{!hasBadReadoutPixel}$** : each triggered pixel is required to be at least two column pixels or two row pixels far from a bad pixel. This cut has been introduced to avoid to select events with bad readout pixels.
- **$\mathbf{pixelsOnEdge} < 0.5$** : the number of pixels on the edge of the camera is required to be smaller than half the number of triggered pixels. This cut has been introduced because it was observed that downward-going events from background simulations with most of the triggered pixels on the edge of the camera had a high chance to be erroneously reconstructed as upward-going events.
- **$(\mathbf{GHchi2/ndf})_{\mathbf{up}} < 1.2 \cdot (\mathbf{GHchi2/ndf})_{\mathbf{down}}$** : the ratio between the reduced χ^2 of the Gaisser-Hillas fit from the PCGFup reconstruction and that from the PCGFdown reconstruction is required to be smaller than 1.2. This cut allows to reject events with a PCGFdown reconstruction resulting in a much better fit of the energy deposit profile with respect to the PCGFup reconstruction.

Following a conservative approach, this analysis has been performed preferring more stringent selection criteria to more relaxed ones because of the unknown origin of this class of events and in order to ensure an high quality of the potential candidates. In addition to the above criteria, a dedicated selection cut has been introduced and studied to discriminate between signal events and background events as described in the following.

5.5 Discrimination between signal events and background events

The discrimination between signal events and background events is performed by exploiting the two modes of the PCGF reconstruction. As mentioned in section 5.3, the two maximum likelihoods L_{down} and L_{up} can be compared to infer how much likely an event is downward-going or vice-versa. For this purpose, the variable $-2 \log(L_{\text{down}} / \max(L_{\text{up}}, L_{\text{down}}))$ has been used. The higher the probability for an event to be downward-going, the closer to zero it becomes. To have a quantity that is defined between 0 and 1 it is convenient to re-define it as:

$$l = \frac{\arctan(-2 \log(L_{\text{down}} / \max(L_{\text{up}}, L_{\text{down}})) / 50)}{\pi/2}. \quad (5.1)$$

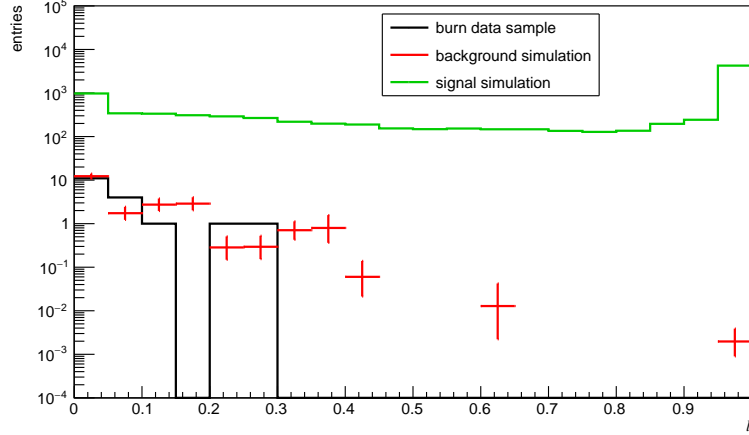


Figure 5.11: Distribution of l for the burn data sample, the background and the signal simulations with all the selection criteria defined in section 5.4 applied. The background simulation includes the events in the simulated energy range $\log_{10}(E/\text{eV}) \in [17, 20]$ and has been weighted to the cosmic ray energy spectrum measured by the Pierre Auger Observatory (see section 1.2) and normalized to the burn data sample i.e. the total number of events has been divided by 10 because the burn data sample consists of the 10% of the data. The uncertainties on the entries of the background distribution have been calculated using the Poisson statistics to properly take into account the statistics of small numbers. The signal simulation has not been weighted because the energy spectrum of this class of events is not known. It includes the events with a simulated calorimetric energy in the range $\log_{10}(E_{\text{cal}}/\text{eV}) \in [16.5, 18.5]$. Figure from [140].

According to this definition, upward-going-like events have an l close to 1, while downward-going-like events have an l close to 0.

To set a cut value on l and select events that are more likely upward-going, the distribution of this variable has been studied for signal simulations, background simulations and for the burn data sample. The corresponding distributions are shown in Figure 5.11. It can be noted that there is a good agreement between the distribution of the background simulations and the burn data sample. To allow for this comparison, the background simulations have been weighted to the cosmic ray energy spectrum and normalized to the fraction of the burn data sample. The signal distribution has not been weighted because the energy spectrum for this class of events is not known. The cut value has been chosen by making an assumption about the extrapolation of the background distribution and performing a scan on l to find the value that minimizes the integral upper limit that could be set if no candidate events are observed after unblinding the remaining 90% of data. The integral upper limit has been calculated as:

$$F^{95\%}(E_{\text{cal}} > E_0) = \frac{N^{95\%}}{\langle \varepsilon \rangle}, \quad (5.2)$$

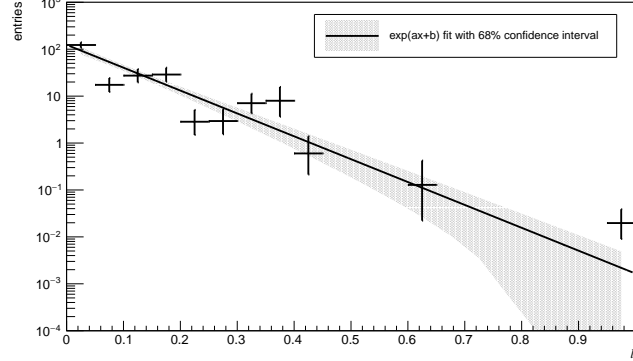
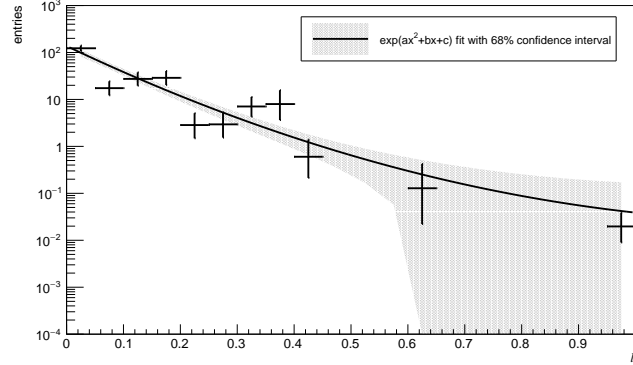

 (a) Background distribution fitted with $\exp(ax + b)$

 (b) Background distribution fitted with $\exp(ax^2 + bx + c)$

Figure 5.12: Distribution of l for the background simulation fitted with the functions $\exp(ax + b)$ (a) and $\exp(ax^2 + bx + c)$ (b) via the weighted log likelihood method. The background simulation has been weighted according to the cosmic ray energy spectrum measured by the Pierre Auger Observatory but not to the burn data sample. All the background events in the simulated energy range $\log_{10}(E/\text{eV}) \in [17, 20]$ passing the selection criteria defined in section 5.4 have been considered. These are two of the parameterization that have been used to perform the upper limit minimization described in the text. Figure (a) is from [140].

where $N^{95\%}$ is the Rolke limit [157] on the number of upward-going events under the assumption that the number of observed events is equal to the expected number of background events and $\langle \varepsilon \rangle$ is the $E_{\text{cal}}^{-\gamma}$ weighted average exposure for $E_{\text{cal}} > E_0$, which is calculated as:

$$\langle \varepsilon \rangle = \frac{\int_{E_{\text{cal}} > E_0} E_{\text{cal}}^{-\gamma} \varepsilon(E_{\text{cal}}) dE_{\text{cal}}}{\int_{E_{\text{cal}} > E_0} E_{\text{cal}}^{-\gamma} dE_{\text{cal}}}, \quad (5.3)$$

where E_{cal} is the simulated calorimetric energy and $\varepsilon(E_{\text{cal}})$ is the exposure for a flat

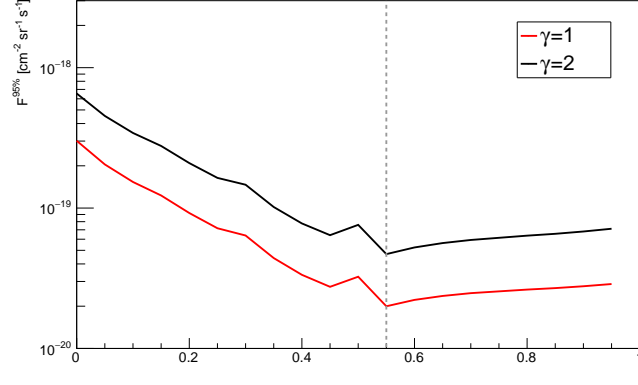
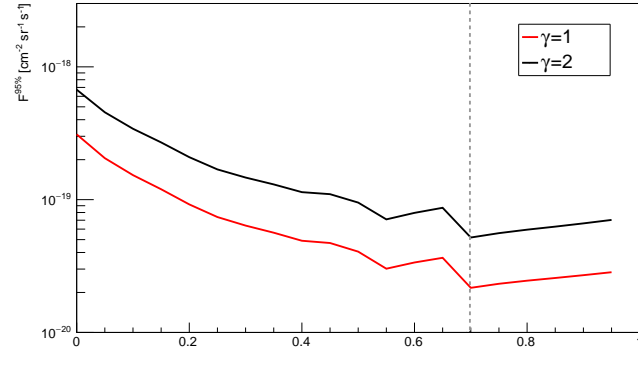

 (a) Case of background distribution fitted with $\exp(ax + b)$

 (b) Case of background distribution fitted with $\exp(ax^2 + bx + c)$

Figure 5.13: Integral upper limit as a function of l for $E_{\text{cal}} > 10^{17.5}$ eV obtained by fitting the background distribution with the functions $\exp(ax + b)$ (a) and $\exp(ax^2 + bx + c)$ (b). The power-law indices $\gamma = 1$ and $\gamma = 2$ have been used for the energy spectrum in the calculation of the average exposure, since the energy spectrum of the signal events is not known. The integral upper limit has been calculated considering the background events in the whole energy range of simulation ($\log_{10}(E/\text{eV}) \in [17, 20]$). The minimum value of the integral upper limit has been found at $l = 0.55$ for (a) and $l = 0.70$ for (b) (dashed gray lines). The bump observed before the minimum value of the integral upper limit is due to the fact that the number of observed events has to be an integer number and thus it is rounded to the integer value closest to the number of events expected from background. Figure (a) is from [140].

generation in H_{fi} and isotropic emergence. The Rolke limit has been used in place of that from the Feldman-Cousins approach because it allows to take into account the uncertainty on the expected number of background events. The latter is calculated

parameterizing the distribution of the background with different functions. For each of them, the value of l yielding the minimum of the integral upper limit has been searched for. Two of the parameterizations that have been studied (i.e. $\exp(ax + b)$ and $\exp(ax^2 + bx + c)$) are shown in Figure 5.12, while the corresponding integral upper limits as a function of l and $E_0 = 10^{17.5}$ eV are shown in Figure 5.13. The value of E_0 has been chosen in order to consider only the calorimetric energy region corresponding to a non-zero exposure. The uncertainty coming from the fit has been taken into account in the calculation of the Rolke limit.

After comparing the results obtained with the different fitting functions that have been studied, the parameterization shown in Figure 5.12(a) has been chosen. The value of l corresponding to the minimum of the integral upper limit for this parameterization, in fact, is smaller than that obtained from the others, while the resulting integral upper limits are the same within about 10 % (see Figure 5.13). Anyhow, the choice of a smaller cut value on l has the advantage of increasing the number of selected signal events (see Figure 5.11), resulting in a larger exposure.

Using the chosen parameterization, the minimum value of the integral upper limit has been found for $l = 0.55$ (see Figure 5.13(a)). This is the cut that has been chosen as discrimination value between candidate events and background ones. Given this cut value, the expected number of background events from the fit with the function $\exp(ax + b)$ is:

$$n_{\text{bkg}} = 0.45 \pm 0.18, \quad (5.4)$$

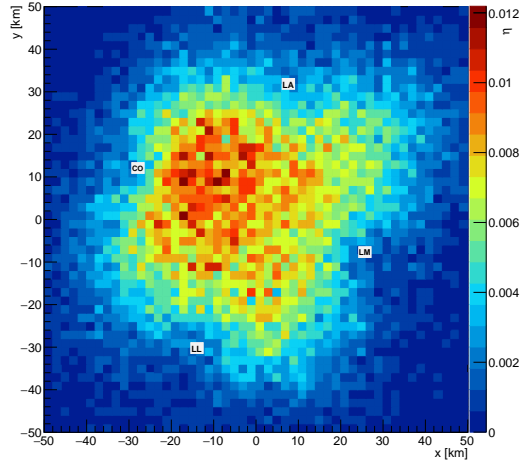
where the fact that different parameterizations yielded the same upper limits within about 10 % has been taken into account in the calculation of the uncertainty. As an example, the background event shown in Figure 5.8 passes all the selection criteria described in section 5.4, but is rejected by l cut defined in this section.

After the unblinding of the data the integral upper limit has been calculated according to Eq. 5.2 using the number of events observed in the full data sample and the number of background ones from Eq. 5.4.

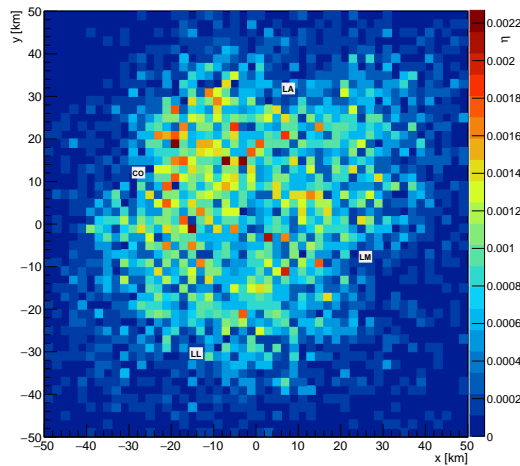
5.6 Detection efficiency and exposure with selection cuts

Once all the selection criteria have been defined, their impact on the detection efficiency and thus on the exposure can be studied. The detection efficiency as a function of the position of the exit points on the generation area before and after applying the selection cuts is shown in Figure 5.14. Events passing the selection criteria do not show any significant clustering on the map of the generation area with respect to the generated ones, confirming that most of the selected events have an exit point inside the area covered by the SD array and that the presence of HEAT allows to increase the detection efficiency in front of the Coihueco site.

The detection efficiency and the exposure, both calculated considering the events surviving the selection criteria, are shown in Figure 5.15. To allow for a better comparison with Figure 5.4), the whole calorimetric energy region of interest $\log_{10}(E_{\text{cal}}/\text{eV}) \in [16.5, 18.5]$ has been shown. No events with a calorimetric energy below about $10^{17.3}$



(a) FD detection efficiency without selection cuts



(b) FD detection efficiency with selection cuts

Figure 5.14: FD detection efficiency as a function of the position (x, y) of the exit points on the generation area of $100 \text{ km} \times 100 \text{ km}$ used in the Real Monte Carlo simulation for the case of no selection criteria applied (a) and all selection cuts applied (b). The detection efficiency in (a) is not the same as Figure 5.5 because in this case only the events with a simulated calorimetric energy in the region $\log_{10}(E_{\text{cal}}/\text{eV}) \in [16.5, 18.5]$ have been considered. The point $(0, 0)$ corresponds to the position of the SD station closest to the center of the SD array.

eV pass the selection criteria. Despite being potentially detectable with the FD, low calorimetric energy events give a zero contribution to the final exposure. This has to

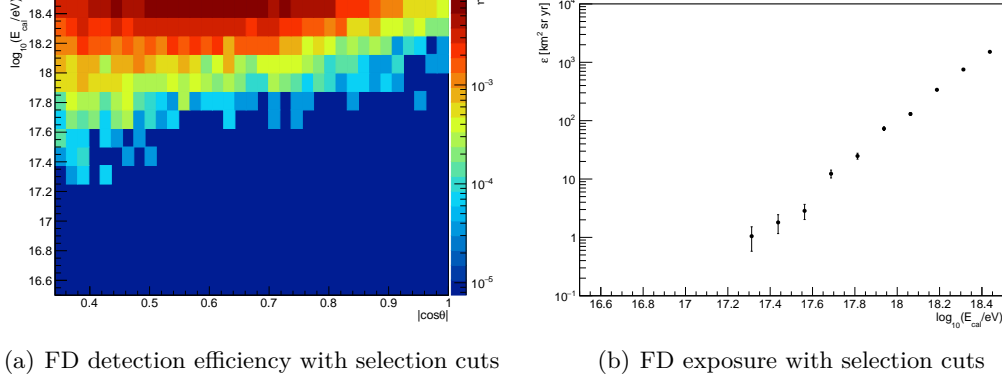


Figure 5.15: FD detection efficiency as a function of $\log_{10}(E_{\text{cal}}/\text{eV})$ and $|\cos \theta|$ (a) and FD exposure as a function of $\log_{10}(E_{\text{cal}}/\text{eV})$ (b), both obtained from the Real Monte Carlo simulation applying all the selection cuts defined in the text.

be taken into account in case of further signal simulations to increase the statistics. The final exposure will be presented in a different way in the next section.

5.7 Unblinding of the data and differential exposure

After having performed the unblinding of the data, $n_{\text{obs}} = 1$ event that has been observed to pass all the selection criteria. This number is consistent with the expected background events. The integral upper limit obtained using equation 5.2 for two different values of γ (i.e. $\gamma = 1, 2$) is:

$$\begin{aligned} F_{\gamma=1}^{95\%}(E_{\text{cal}} > 10^{17.5} \text{ eV}) &= 3.6 \cdot 10^{-20} \text{ cm}^{-2} \text{ sr}^{-1} \text{ s}^{-1}, \\ F_{\gamma=2}^{95\%}(E_{\text{cal}} > 10^{17.5} \text{ eV}) &= 8.5 \cdot 10^{-20} \text{ cm}^{-2} \text{ sr}^{-1} \text{ s}^{-1}. \end{aligned} \quad (5.5)$$

These integral upper limits have been calculated by using the exposure shown in Figure 5.15(b). It should be noted that they do not refer to the flux of hypothetical particles producing a secondary flux of protons, but to the flux of protons itself under the assumption of different energy spectra. Therefore, these integral upper limits should be intended as benchmark values. Equation 4.16 can be used to calculate a differential exposure as a function of the point of first interaction, H_{fi} . It is simply given by:

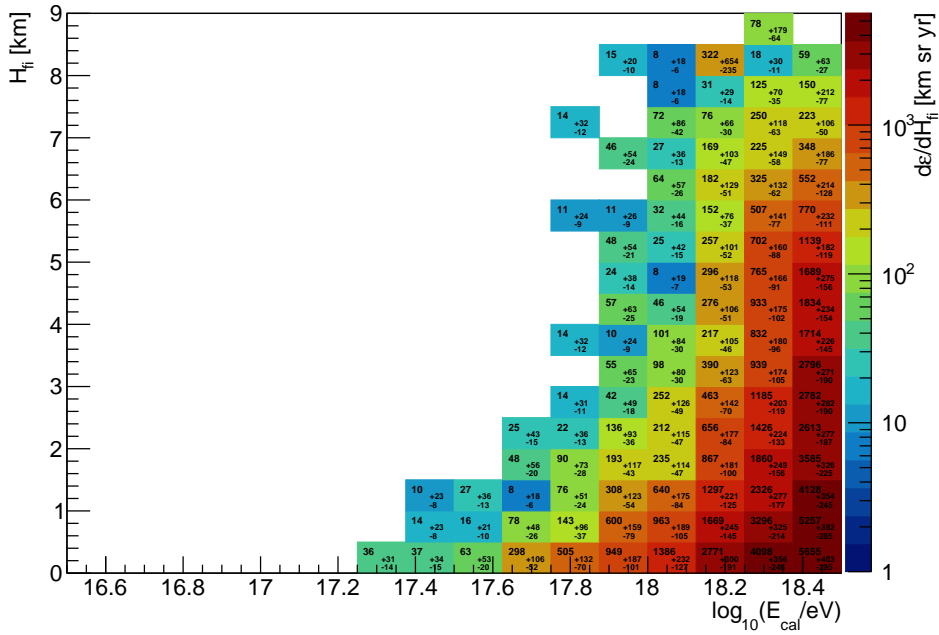
$$\frac{d\varepsilon}{dH_{fi}}(E_{\text{cal}}, H_{fi}) \simeq 2\pi \cdot S_{\text{gen}} \cdot \Delta T \cdot \sum_i \eta(E_{\text{cal}}, \cos \theta_i, H_{fi}) \cdot \frac{1}{\Delta H_{fi}} \cdot \cos \theta_i \cdot \Delta \cos \theta_i. \quad (5.6)$$

This has been done to allow our results to be applied to different scenarios.

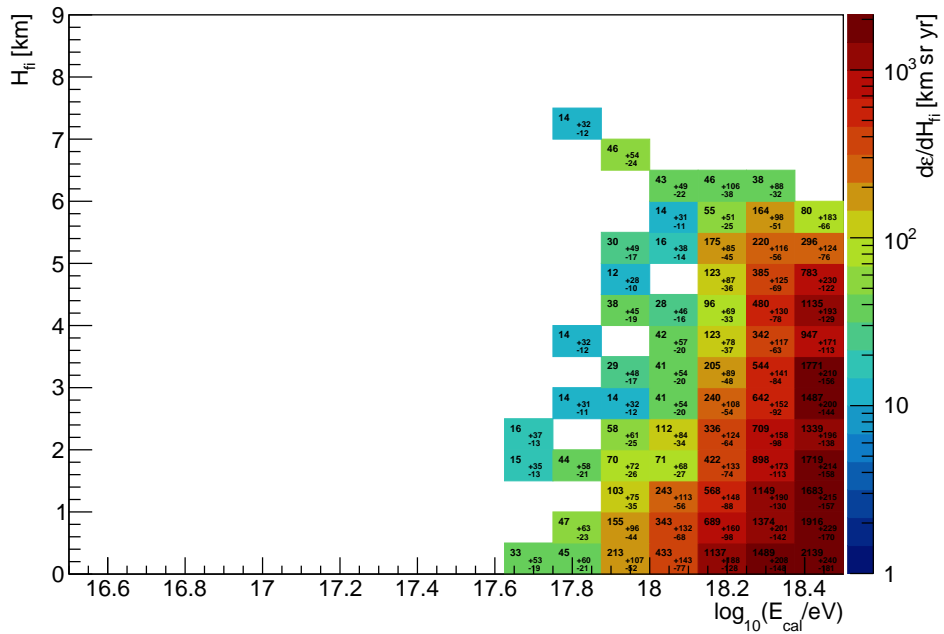
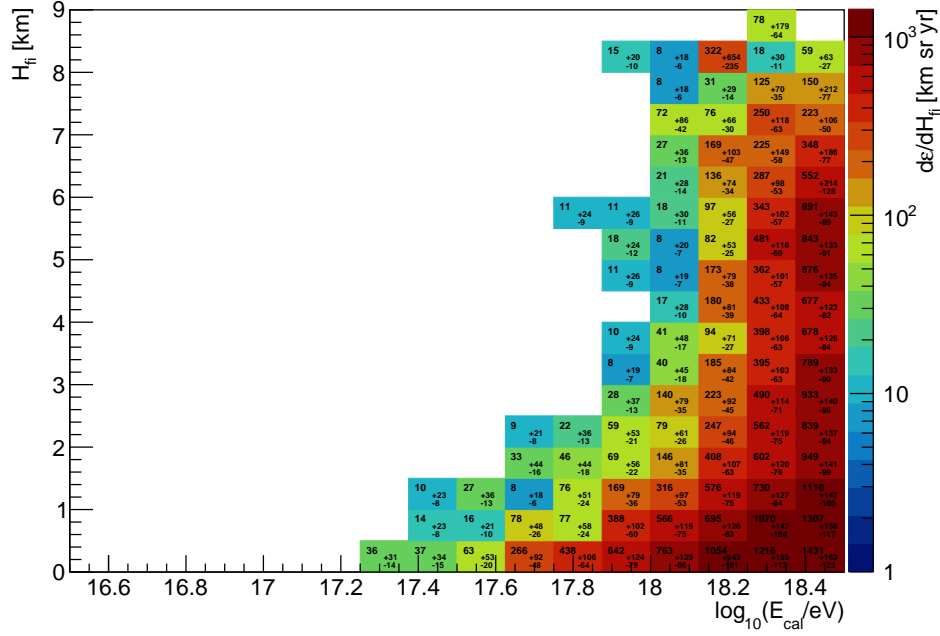
The differential exposure obtained according to Eq. 5.6 for a flat generation in height of first interaction and an isotropic emergence are shown in Figure 5.16. These tables can be used to set limits for different physical scenarios, such as the one that

predicts upward-going showers initiated by tau leptons that are produced in the interaction of tau neutrinos with the Earth. This can be done by simulating the propagation and decay of tau leptons with dedicated softwares and then binning the distribution of tau lepton decay induced showers in height of first interaction and energy of the shower. The exposure of the Pierre Auger Observatory to tau leptons can be obtained by folding the resulting distribution with the differential tables provided in this section. The exposure can be then used to calculate the upper limits on the flux of tau leptons. A detailed description of this application can be found in [158].

To compare these results with the ANITA observations, a similar estimation of its exposure to upward-going showers as a function of energy and altitude would be needed. Such a comparison is currently on-going within the Pierre Auger Collaboration and will be included in a future full collaboration paper.



(a) $\theta \in [110, 180]^\circ$



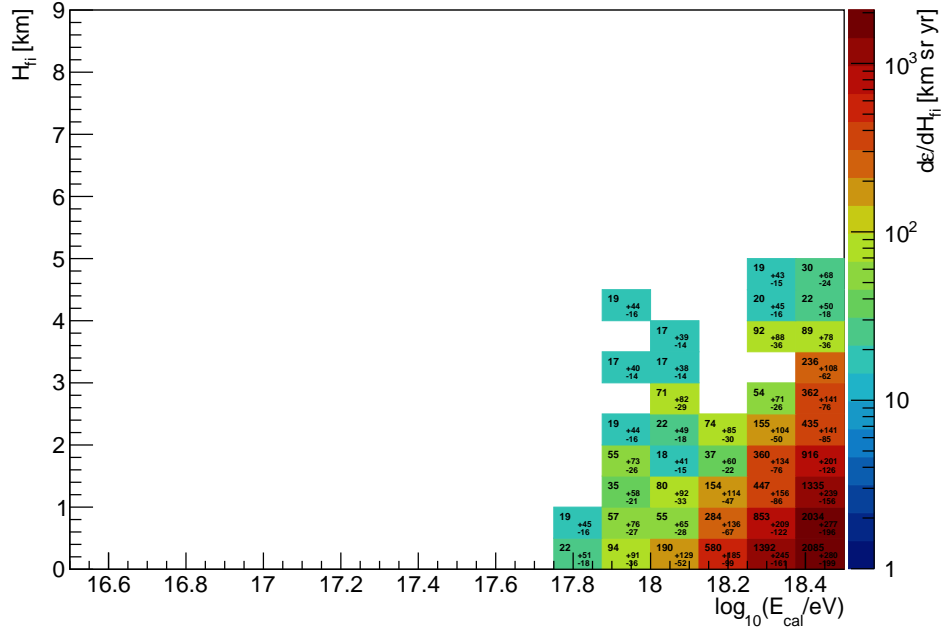

 (d) $\theta \in [141.3, 180]^\circ$

Figure 5.16: Double differential exposure obtained according to Eq. 5.6 as a function of H_{fi} and $\log_{10}(E_{cal}/eV)$ and for different ranges of zenith angles ($\theta \in [110, 180]^\circ$ (a), $\theta \in [110, 124.2]^\circ$ (b), $\theta \in [124.2, 141.3]^\circ$ (c), $\theta \in [141.3, 180]^\circ$ (d)). The exposure calculation refers to a flat generation in H_{fi} and an isotropic emergence. The uncertainties on the values of the exposure has been calculated using the Poisson statistics. Figures from [140].

Conclusions

My thesis work has been focused on the search for upward-going showers with the Fluorescence Detector of the Pierre Auger Observatory. To study the sensitivity of the Pierre Auger Observatory to upward-going showers, I performed a Real Monte Carlo simulation of proton induced upward-going showers, which can be scaled to fit other physical scenarios. Before setting up this simulation, which is quite expensive in terms of computing time, I developed a Fast Monte Carlo simulation based on simple geometrical and physical assumptions to define an effective generation area for the events of the Real Monte Carlo simulation. This area has been chosen to be a square area of $100 \text{ km} \times 100 \text{ km}$ centered at the water Cherenkov station closest to the center of the Surface Detector array. The potential background for this search consists of downward-going showers with specific geometric configurations that can be mis-reconstructed as upward-going events in a monocular reconstruction. In order to estimate the number of events expected from background, I performed, together with my Auger colleagues, an extensive simulation of downward-going events using a spherical generation geometry. Also laser shots, which are used to monitor the quality of the atmosphere and are upward-going events, can potentially produce background if they are not properly labelled. To clean the data from laser events, a sample made of 10% of the available Fluorescence Detector data from 14 years of operation (burn data sample) has been used. Moreover, a set of quality selection criteria has been defined and applied on background simulation, signal simulation and burn data sample in order to preserve the quality of the reconstruction and thus reduce the confusion between downward-going and upward-going events. A dedicated variable to discriminate between background and signal events has been then defined. I studied the distribution of this variable for background simulation, signal simulation and burn data sample. To set a cut value on this variable, I parameterized the distribution for background simulations using different functions and then I performed a minimization of the integral upper limit that could be set if no candidate events were observed. The minimum cut value corresponding to the minimum integral upper limit between the different parameterizations has been chosen as discrimination value. The number of events expected from background with all the defined selection criteria has been estimated to be $n_{\text{bkg}} = 0.45 \pm 0.18$, while the unblinding of the data resulted in $n_{\text{obs}} = 1$ event. Since the number of observed events is consistent with the number of expected background events, I derived an integral upper limit on the flux of upward-going proton induced showers using different assumptions on the energy spectrum in the calculation of the average exposure. The resulting inte-

CONCLUSIONS

gral upper limits are $F_{\gamma=1}^{95\%}(E_{\text{cal}} > 10^{17.5} \text{ eV}) = 3.6 \cdot 10^{-20} \text{ cm}^{-2}\text{sr}^{-1}\text{s}^{-1}$ for the case of a E_{cal}^{-1} weighted average exposure and $F_{\gamma=2}^{95\%}(E_{\text{cal}} > 10^{17.5} \text{ eV}) = 8.5 \cdot 10^{-20} \text{ cm}^{-2}\text{sr}^{-1}\text{s}^{-1}$ for the case of a E_{cal}^{-2} weighted average exposure. Since they refer to proton induced showers, these integral upper limits can be considered as benchmark values. I finally produced a set of differential tables of exposure, which can be used for example to derive the exposure of the Pierre Auger Observatory to upward-going tau lepton decay induced showers.

An estimation of the ANITA exposure to upward-going showers is required in order to compare the results from this analysis with those from the ANITA experiment. This comparison is currently underway within the Pierre Auger Collaboration and will be published soon in a full collaboration paper. If the Auger exposure will be found to be greater than the ANITA one, the result of this search will represent a strong constraint on the interpretation of the ANITA anomalous events as upward-going showers. Considering also the results obtained by the IceCube Collaboration, this will lead to the need for a different interpretation of these events. Anyhow, the differential tables of exposure can be used to constrain theoretical models that could predict the production of upward-going showers at elevation angles far beyond of the horizontal.

This search can be improved by defining an analysis based on anomaly detection techniques. These techniques allow to search for events that deviate from the behaviour of the majority of the data and thus can be used to search for upward-going showers in a dataset dominated by downward-going events. This can be done just by using the signals on the single PMTs of the Auger telescopes, without applying any reconstruction on the events. The method is expected to enhance the identification power of candidate events, allowing to relax the selection criteria applied in the standard analysis. This will result in an increase in the exposure and thus in the constraint power of the Pierre Auger Observatory. The anomaly detection analysis strategy has already been defined and is presently on-going at the University of L'Aquila.

Appendix A

Measurement of the linearity of two Hamamatsu R9420 PMTs

The measurement of the linearity of two Hamamatsu R9420 PMTs used to test the new SSD modules has been performed during an SSD assembling shift at the University of Salento, Lecce (Italy). The dependence of the anode current at which the non-linearity of each PMT becomes of 5% on the gain has been also studied.

A.1 The experimental setup

A schematic view of the experimental setup, which is the same as described in [159], is shown in Figure A.1. The dark box has a size of 70 cm \times 70 cm \times 70 cm and hosts one PMT at a time. The PMT looks towards a LED Pulser placed at the roof of the box. The LED Pulser is controlled through a board connected to the data acquisition computer. Two blue LEDs with 470 nm wavelength and 45° viewing angle are used. A LED driver [159] ensures a fast turn-on turn-off response. The two LEDs are placed in the center of a small box housing the driver. The signals from both the anode and the dynode are sent to a digital oscilloscope connected to the computer through General Purpose Interface Bus (GPIB). The data acquisition user interface is written in LabVIEW¹. A dedicated tab of the front panel allows to tune the system parameters, such as the LED voltage and the oscilloscope acquiring conditions. Furthermore, an online data analysis (peak finding, charge calculation and spectra) is provided to monitor the measurements during data taking. Data files are also produced allowing to perform offline analyses [160].

A.2 Non-linearity measurements

Since the PMTs are required to have a linear response over a large dynamic range, the non-linearity (NL) of the PMTs as a function of the anode current has been

¹<https://www.ni.com/labview/>

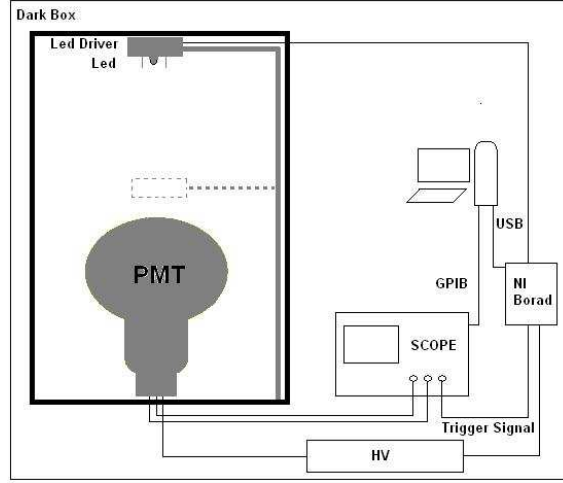


Figure A.1: Schematic view of the experimental setup used to measure the linearity of the two Hamamatsu R9420 PMTs. Figure from [159].

studied using the double LED method. The anode current in the PMT is changed by modifying the LED voltage. The system can pulse two blue LEDs independently (LED_1 and LED_2) and simultaneously (LED_{12}). For each configuration (LED_1 , LED_2 and LED_{12}) the measurement is repeated 200 times. The measurement of the NL of the PMT as a function of the anode current is obtained by varying the light intensity of the two LEDs and computing the quantity:

$$NL = \frac{LED_{12} - (LED_1 + LED_2)}{LED_1 + LED_2}, \quad (A.1)$$

where LED_1 , LED_2 and LED_{12} are the signals from the corresponding configurations. The percentage NL of two Hamamatsu R9420 PMTs (referred as PMT 3851 and PMT 4151) as a function of the anode current has been studied for different values of the supply voltage. The corresponding plots are shown in Figure A.2 and Figure A.3. From these plots, the anode current at which the percentage NL becomes $\pm 5\%$ has been found by interpolating the two points before and after that value with a linear function. Afterwards, the dependence of the anode current at which the percentage NL is $\pm 5\%$ on the gain, which depends on the supply voltage, has been studied. The gain is measured following the same procedure as described in [159]. The gain as a function of the supply voltage for the two PMTs is shown in Figure A.4. The gain G for each supply voltage V can be obtained by performing a fit on these plots with the function $G = aV^b$ [159]. The anode current at which the percentage NL is $\pm 5\%$ changes in a non-linear way according to the gain, at least at low gains (see Figure A.5). A function that well describes its behaviour is:

$$f(x) = p_0 + p_1 \cdot \sqrt{x}, \quad (A.2)$$

APPENDIX A. MEASUREMENT OF THE LINEARITY OF TWO HAMAMATSU R9420 PMTS

as shown in Figure A.6. Given a certain gain, the anode current up to which the behaviour of the PMTs is linear within 5% can be inferred from the result of the fit performed using this function.

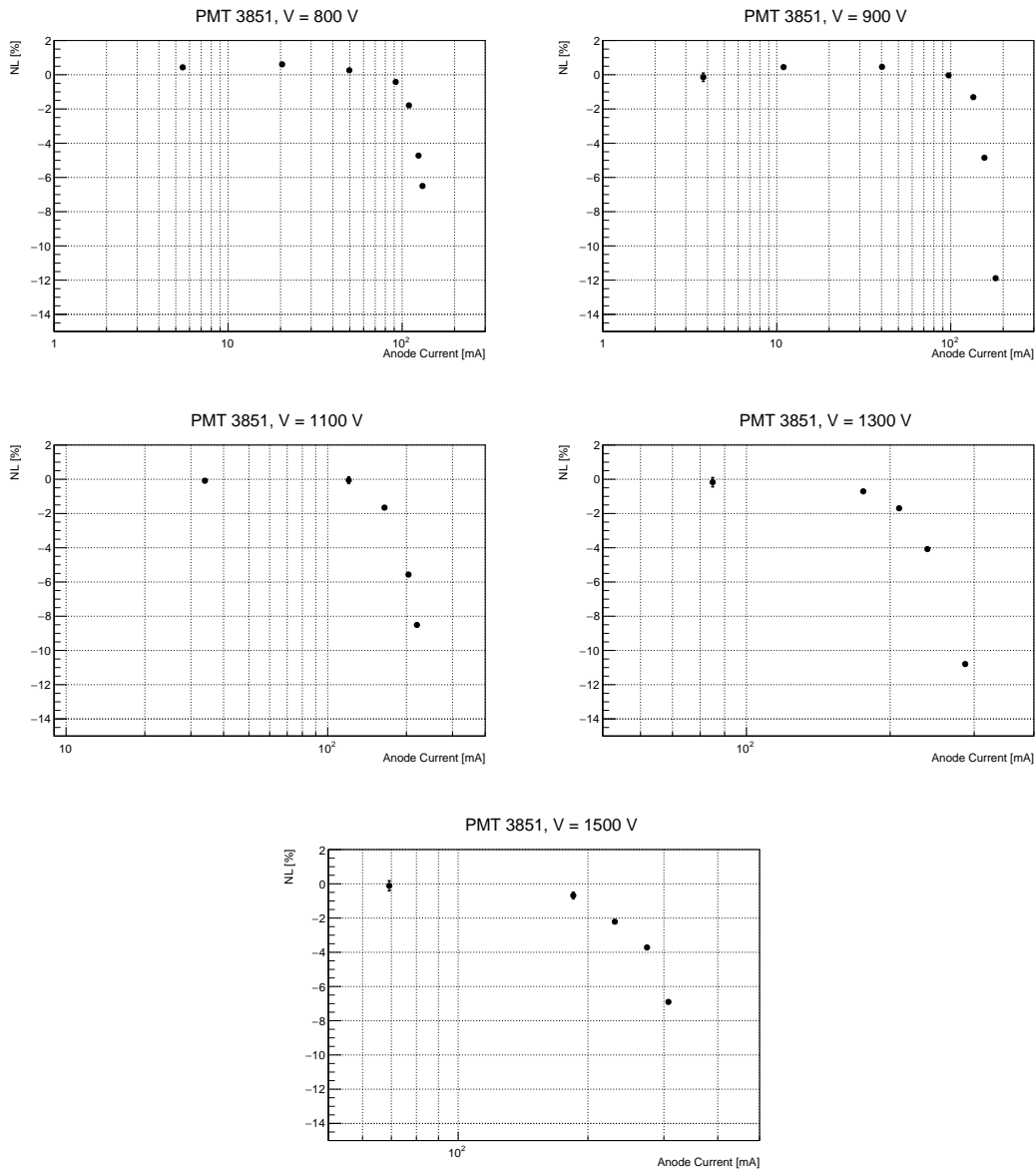


Figure A.2: Percentage non-linearity of the PMT 3851 as a function of the anode current for different values of the supply voltage V ($V = 800$ V, $V = 900$ V, $V = 1100$ V, $V = 1300$ V, $V = 1500$ V).

APPENDIX A. MEASUREMENT OF THE LINEARITY OF TWO HAMAMATSU R9420 PMTS

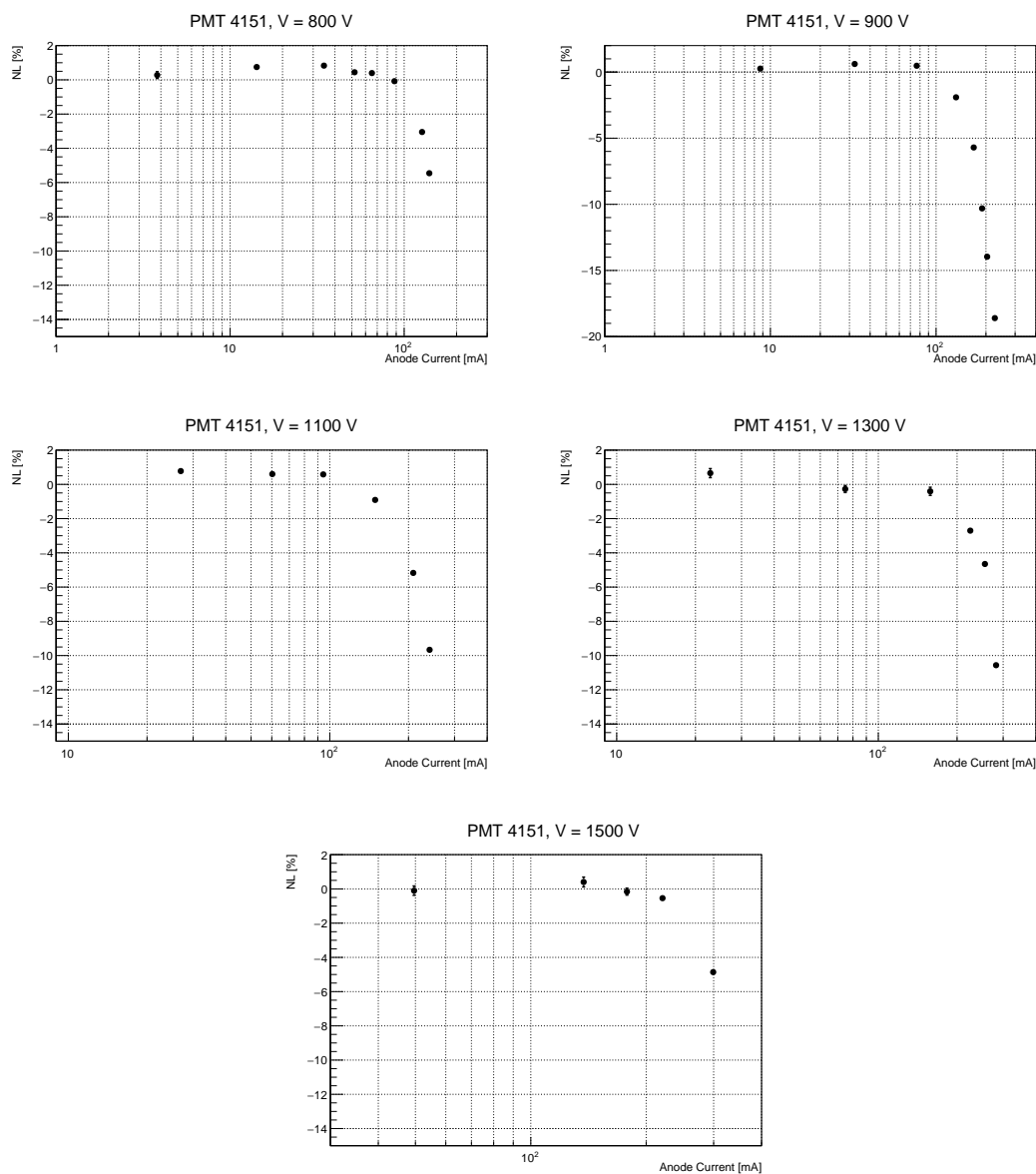


Figure A.3: Percentage non-linearity of the PMT 4151 as a function of the anode current for different values of the supply voltage V ($V = 800$ V, $V = 900$ V, $V = 1100$ V, $V = 1300$ V, $V = 1500$ V).

APPENDIX A. MEASUREMENT OF THE LINEARITY OF TWO HAMAMATSU R9420 PMTS

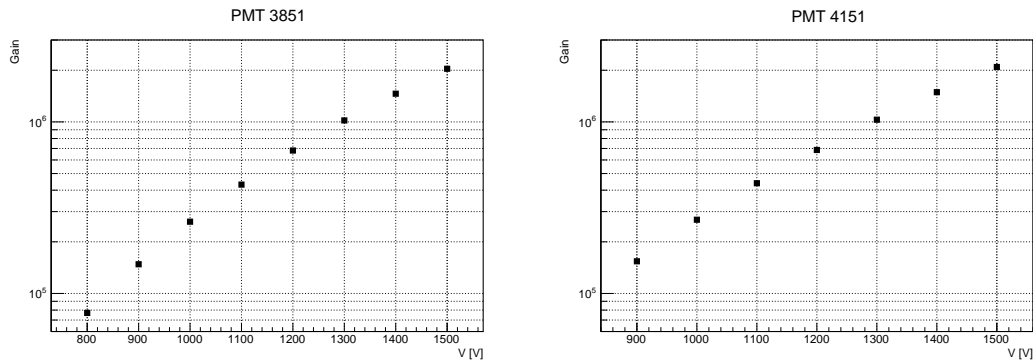


Figure A.4: Gain as a function of the supply voltage for the PMT 3851 (left) and the PMT 4151 (right).

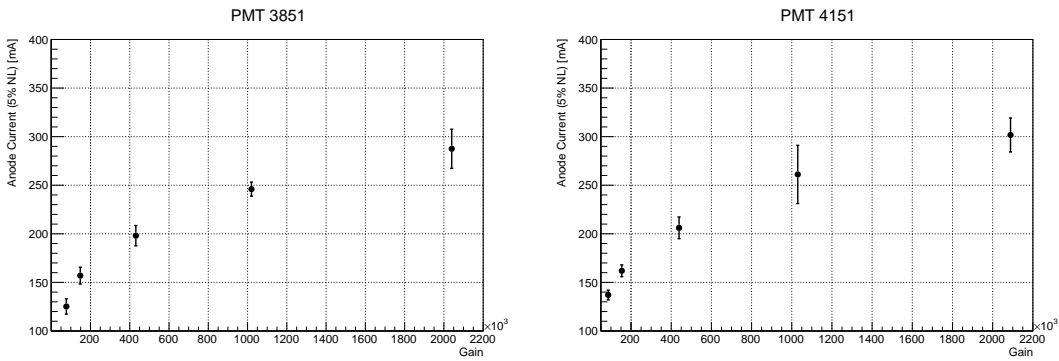


Figure A.5: Anode current at which the percentage non-linearity is $\pm 5\%$ as a function of the gain for the PMT 3851 (left) and the PMT 4151 (right).

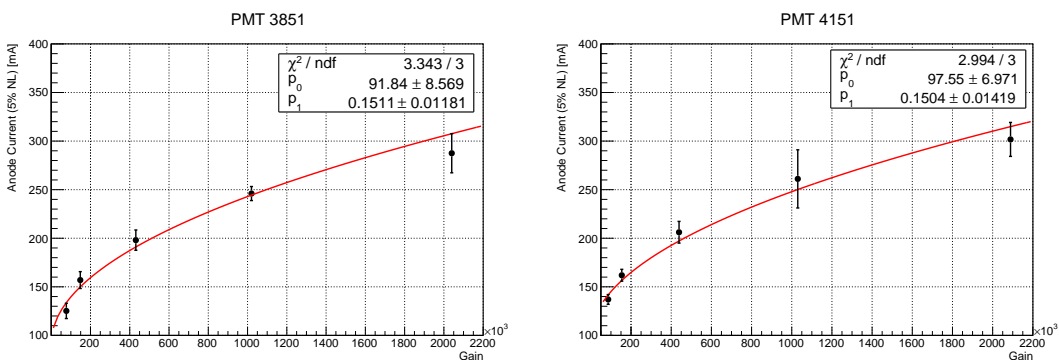


Figure A.6: Result of the fit performed using the function in Eq. A.2 on the anode current at which the percentage non-linearity is $\pm 5\%$ as a function of the gain for the PMT 3851 (left) and the PMT 4151 (right). The fitting function well reproduces the behaviour of the data.

APPENDIX A. MEASUREMENT OF THE LINEARITY OF TWO HAMAMATSU
R9420 PMTS

Appendix B

Hadronic interaction models used in air shower simulations

The flux of the cosmic rays decreases with the energy, therefore UHCRs can be detected only by measuring the secondary particles generated by their interaction with the atmosphere. To determine the energy and the chemical composition of the UHE-CRs, the experimental data need to be compared with the results from the air shower simulations. For this reason, hadronic interactions need to be properly modeled in order to perform the analysis of the data. In contrast to the electroweak interactions that occur during the shower development, the hadronic interactions are not simple to model and present large theoretical uncertainties. In the case of hard processes i.e. processes characterized by a large momentum transfer, accurate results for high energy interactions can be obtained from the quantum chromodynamics (QCD) by using perturbative methods. However, since most of the processes occurring during high energy collisions are soft processes i.e. processes with a small momentum transfer, also non perturbative effects have to be considered [161]. Hadronic interaction models are separated between high and low energy models. High energy models can be extrapolated to the highest energies and are assumed to be valid above a transition energy that is not univocally determined and can be set up to a few hundred GeV [162]. Low energy models, on the contrary, are assumed to be valid in the energy range between the energy threshold for particle production and the transition energy [25]. In the following sections, the main differences between some of the most frequently used hadronic interaction models at high energies (QGSJET II [145], SIBYLL [146, 147] and EPOS [148]) and low energies (GHEISHA [163], FLUKA [164] and UrQMD [155]) will be highlighted.

B.1 High energy hadronic interaction models

QGSJET II and EPOS are based on the Gribov-Regge field theory (GRT) [165], which allows to describe soft interactions at high energies. Hadronic collisions are treated as multiple scattering processes where each elementary re-scattering corre-

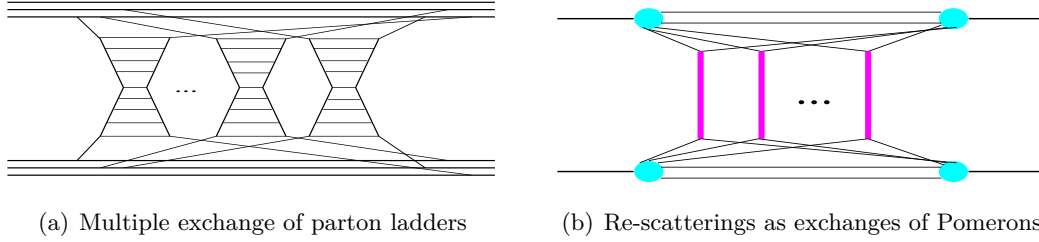


Figure B.1: A hadron-hadron scattering as multiple exchange of parton ladders (a) and a typical contribution to hadron-hadron scattering amplitude with elementary re-scatterings treated as exchanges of Pomerons (b). Figures from [166].

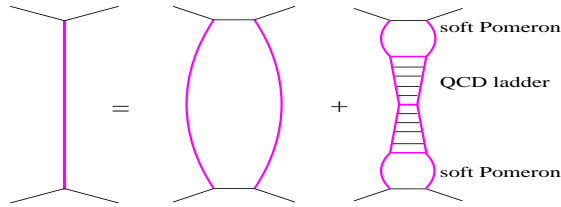


Figure B.2: A general Pomeron as the sum of a soft and a semi-hard Pomeron. The semi-hard Pomeron is represented as a QCD ladder between two soft Pomerons. Figure from [166].

sponds to the exchange of a microscopic parton cascade, as shown in Figure B.1(a). Since most of the exchanged partons have a small transverse momentum, the perturbative QCD approach can not be used and each elementary re-scattering process is treated as an exchange of a quasi-particle, called Pomeron. The scattering amplitude is then given by the sum of the diagrams shown in Figure B.1(b). With the increase of the energy, also the contribution from semi-hard processes i.e. processes with a momentum transfer larger than that of soft processes needs to be considered. Since these processes can be treated by using a perturbative QCD approach and thus both perturbative and non-perturbative processes contribute to the microscopic parton cascades, a general Pomeron can be considered as the sum of a soft and a semi-hard Pomeron. The semi-hard part can be represented as a QCD ladder between two soft Pomerons, as shown in Figure B.2. In contrast to QGSJET II and EPOS, the minijet model [167, 168, 169, 170] combined with the eikonal approach [170, 171, 172] is used in SIBYLL, which is the high energy model that has been used in the Real Monte Carlo simulation described in Chapter 5. In this hadronic interaction model, the hard part is treated by considering only the QCD ladder contributions of the semihard Pomerons, under the assumption that the soft interactions can be neglected in the secondary particle production. The eikonal approach relies on the presence of minijets, where high energy partonic interactions are described using the production of jets with low trans-

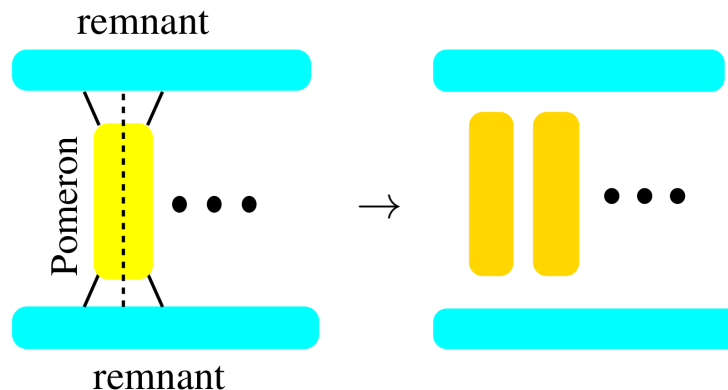


Figure B.3: A pomeron as a two layer parton ladder attached to projectile and target remnants through two color singlets (left) and a cut Pomeron seen as two strings (right). Figures from [175].

verse momentum [161]. Originally, only one soft interaction was allowed in SIBYLL, but in the more recent version SIBYLL 2.3c a larger phase space is considered for soft interactions, while multiple soft interactions are described as Pomeron exchanges according to the GRT.

As regards the particle production, the Lund model [173, 174] is adopted in SIBYLL. The final state is obtained via a massless relativistic string, which represents the QCD color force field, where the string endpoint excitations and the internal excitations of the color field are represented by quarks (antiquarks) and gluons, respectively. These strings break because of quantum tunneling, producing quark-antiquark pairs which result in the hadronic remnant with excitation energy and momentum described by a phenomenological function [161]. In EPOS, the particle production considers both the decay of the hadronic remnant mentioned before and the hadronization of a cut Pomeron. As shown in Figure B.3, a pomeron can be considered as a two layer parton ladder attached to projectile and target remnants through two color singlets of type $q\bar{q}$, qqq or $\bar{q}\bar{q}\bar{q}$ (taken from the sea because an undefined number of Pomerons can be involved in the process) [175]. The hadronization of a cut Pomeron occurs because it can be seen as two strings with q (\bar{q}) or qq ($\bar{q}\bar{q}$) at the string ends. In QGSJET II, the particle production is treated by considering Pomeron-Pomeron interactions, which lead to complex multi-ladder diagrams.

The availability of experimental data from particle accelerators like LHC plays an important role in the high energy hadronic interaction models. Parameters like the total $p-p$ cross section need to be extrapolated from the experimental data obtained at lower energies, but this extrapolation is strongly dependent on the model. Furthermore, the total p -air cross section needs to be derived from the $p-p$ one. This derivation is performed by using the Glauber model [176]. The most recent results available from LHC were used to update the old versions of the high energy models to the more recent

versions QGSJET II-04, SIBYLL 2.3c and EPOS-LHC.

The differences between the high energy hadronic interaction models result in differences in the air shower observables and thus in the interpretation of the cosmic ray data. As an example, the differences in the X_{\max} distributions obtained by using different high energy hadronic interaction models are shown in section 4.1.2.

B.2 Low energy hadronic interaction models

Three of the most frequently used low energy hadronic interaction models, used for interaction energies below the transition energy, are GHEISHA, FLUKA and UrQMD. In the low energy model GHEISHA, based on the parameterization of the experimental data from particle accelerators, the energy and momentum are conserved in average but not event by event. The most updated version of this low energy model has an improved conservation of energy and momentum because its older version was kinematically corrected after comparing its results with the experimental data [177].

In the low energy model FLUKA, hadron-nucleon interactions are described by using the resonance superposition model at energies up to ~ 5 GeV and the Dual Parton Model [178] at higher energies. Hadron-nucleus interactions are treated by exploiting the PreEquilibrium Approach to NUClear Thermalization (PEANUT) model, with the inclusion of the Glauber-Gribov multiple collision mechanism followed by a preequilibrium stage and an evaporation/fragmentation/fission and final deexcitation stage [179]. In contrast to GHEISHA, the energy and momentum are conserved event by event a priori.

The low energy model UrQMD is based on the same principles as the Quantum Molecular Dynamic model and its extension to relativistic energies [155]. The properties of the single hadrons together with the interaction cross sections are used as the main inputs of this low energy model. The cross sections are fitted to experimental data, calculated from effective models or parameterized according to the additive quark model. The particle production is treated by using the excitation and fragmentation of color strings according to the Lund model, the excitation and decay of hadronic resonances and the particle-antiparticle annihilation [180]. The UrQMD model is the low energy model that has been used in the Real Monte Carlo simulation for upward-going showers, whose details are reported in Chapter 5.

List of Abbreviations

AB	Analog Board
AERA	Auger Engineering Radio Array
AGN	Active Galactic Nuclei
AMIGA	Auger Muon and Infilled Ground Array
AoP	Area-over-Peak
BDT	Boosted Decision Tree
BLF	Balloon Launching Facility
CC	Charged Current
CDAS	Central Data Acquisition System
CIC	Constant Intensity Cut
CLF	Central Laser Facility
CMB	Cosmic Microwave Background
CO	Coihueco
EAS	Extensive Air Shower
EBL	Extragalactic Background Light
EE	Extended Emission
EM	Electromagnetic
FADC	Fast Analog to Digital Converter
FD	Fluorescence Detector
FLT	First Level Trigger
FoV	Field of View
FPGA	Field Programmable Gate Array
GDAS	Global Data Assimilation System
GPIB	General Purpose Interface Bus
GRB	Gamma Ray Burst
GRT	Gribov-Regge field theory
GST	Greenwich Sidereal Time
GW	Gravitational Wave
GZK	Greisen-Zatsepin-Kuzmin
HE	Head Electronics

LIST OF ABBREVIATIONS

HEAT	High Elevation Fluorescence Telescopes
Hpol	Horizontal polarization
IR-UV	Infrared, optical and ultra-violet
LA	Loma Amarilla
LDF	Lateral Distribution Function
LL	Los Leones
LM	Los Morados
LPM	Landau-Pomeranchuk-Migdal
MC	Monte Carlo
NC	Neutral Current
NL	Non-Linearity
PCA	Principal Component Analysis
PCGF	Profile Constrained Geometry Fit
PCGF _{down}	Profile Constrained Geometry Fit in downward mode
PCGF _{up}	Profile Constrained Geometry Fit in upward mode
PEANUT	PreEquilibrium Approach to NUClear Thermalization
PMT	Photomultiplier tube
QCD	Quantum chromodynamics
SD	Surface Detector
SDP	Shower-Detector Plane
SHDM	Super Heavy Dark Matter
SLT	Second Level Trigger
SM	Standard Model
SPMT	Small Photomultiplier tube
SSD	Surface Scintillator Detector
TD	Topological Defects
TLT	Third Level Trigger
UHECR	Ultra High Energy Cosmic Ray
VAOD	Vertical Aerosol Optical Depth
VCT	Vertical Centered Through-going
VEM	Vertical Equivalent Muon
Vpol	Vertical polarization
XLF	eXtreme Laser Facility

List of Figures

1.1	The cosmic ray energy spectra measured by different experiments. Figure from http://www.physics.utah.edu/~whanlon/spectrum.html	5
1.2	The cosmic ray energy spectra scaled by $E^{2.6}$ measured by different experiments. Figure from [4].	6
1.3	The cosmic ray energy spectrum scaled by E^3 measured by the Pierre Auger Observatory. In each energy region identified by a number the spectrum can be described by a power law with a different spectral index. The shaded band represents the statistical uncertainty of the fit. The upper limits shown in the plot are at the 90% confidence level. Figure from [6].	6
1.4	Collision between a charged particle with velocity v and energy E_1 with a moving magnetic cloud with velocity V . The particle undergoes several collisions inside the cloud and then exits with an energy E_2 . An head-to-head collision (a) and a head-to-tail collision (b) are shown.	8
1.5	A charged particle crossing a plane shock front. The shock front is moving from left to right. Every time the particle crosses the shock front it undergoes an head-to-head collision.	9
1.6	The Hillas plot. The size of the source is plotted on the x-axis, the magnetic field of the source is plotted on the y-axis. The plot shows the regions that correspond to different astrophysical objects. For each particle charge and maximum energy, Eq. 1.22 establishes a linear relationship between R and B , so each primary particle is represented by a line once a maximum energy is fixed. Given a certain particle and a certain maximum energy, it is possible to identify the sources that are able to accelerate that particle up to that energy by comparing the corresponding line with the regions that identify the astrophysical objects. The blue and the red line, corresponding respectively to protons and iron nuclei with the same energy $E = 10^{20}$ eV, show that the acceleration of nuclei is less demanding than the one of protons because of the larger Ze . Figure from [10].	12

LIST OF FIGURES

1.7	Projected view of 20 trajectories of proton primaries emanating from a point source for several energies. Trajectories are plotted until they reach a physical distance from the source of 40 Mpc. Propagation energy losses are not considered. Figure from [12].	13
1.8	Mean energy of protons as a function of propagation distance through the CMB for different energies at the source (10^{22} eV, 10^{21} eV, and 10^{20} eV). Figure from [12].	15
1.9	Panorama of the interactions of possible cosmic primaries with the CMB. Curves marked by " $p + \gamma_{\text{CMB}} \rightarrow e^+ e^- + p$ " and " $Fe + \gamma_{\text{CMB}} \rightarrow e^+ e^- + p$ " are energy loss lengths (the distance for which the proton or Fe nucleus loses 1/e of its energy due to pair production). The curve marked by " $p + \gamma_{\text{CMB}} \rightarrow \pi^+ n$ or $\pi^0 p$ " is the mean free path for photo-pion production of a proton on the CMB. The curve marked " $Fe + \gamma_{\text{CMB}} \rightarrow \text{nucleus} + n$ or $2n$ " is the mean free path for a photo-nuclear reaction where one or two nucleons are chipped off the nucleus. The curve marked " $\gamma + \gamma_{\text{CMB}} + \gamma_{\text{CMB}} \rightarrow e^+ e^-$ " is the mean free path for the interaction of a high energy photon with the CMB. Added for reference is the mean decay length for a neutron indicated by " $n \rightarrow p e \nu$ ". Figure from [12].	16
1.10	Schematic views of an electromagnetic shower (a) and an hadronic shower (b). Figures from [19].	17
1.11	Schematic view of the Heitler model for the development of an electromagnetic shower. Figure from [22].	18
1.12	Schematic view of the generalization of the Heitler model for the development of an hadronic shower. Solid lines represent charged pions, while dashed lines stand for neutral pions that do not interact but decay producing electromagnetic sub-showers. Not all the pions are shown after the level n=2. Figure from [22].	19
2.1	The layout of the Pierre Auger Observatory. Each black dot stands for a water Cherenkov station, while the blue lines represent the azimuthal field of views of the 24 fluorescence telescopes. The four fluorescence detector sites (Los Leones, Los Morados, Loma Amarilla, Coihueco), each of which with six telescopes, are shown. The Coihueco site hosts three extra high elevation (HEAT) telescopes, whose field of views are shown with red lines. The laser facilities (CLF and XLF) that monitor the aerosol content in the atmosphere and the weather balloon launching facility (BLF) are shown with red dots. A denser region of water Cherenkov detectors, named infill array, is located near the Coihueco site. The light-blue circle represents the area equipped with radio antennas (AERA). Figure from https://pc.auger.unam.mx/	24
2.2	A schematic view of a tank with its component from [29] (a) and a personal photo of a tank placed in the Pampa Amarilla (b).	25

2.3	Charge (a) and pulse height (b) histograms from a tank triggered on coincidence of its three PMTs at a trigger level of five channels above baseline. In both histograms the signal from the three PMTs is summed. The black solid histograms refer to a tank simply triggered on a three-fold coincidence, while the red dashed histograms to a tank triggered on central vertically aligned plastic scintillators. The bin containing the peak of the red dashed charge histogram is defined as a vertical equivalent muon. The peak on the left in the black solid histograms is due to low energy and corner-clipping muons convolved with the low threshold coincidence of the three PMTs. The muon peak of the black solid histograms is at a higher value compared to the one of the red dashed histograms because non-vertical muons produce more Cherenkov light. Figures from [32].	26
2.4	Schematic view of the evolution of a shower front (a) and start time relative to the timing of a plane shower front as a function of the perpendicular distance to the shower axis (b). The shaded line in Figure (b) represents the fit according to the shower front evolution model and its uncertainty. Figures from [26].	28
2.5	Signal induced by a shower on the 1500 m spaced stations of the SD (a) and the corresponding LDF (a). The different colors in Figure (a) refer to the time arrival of the shower front (signal arriving first are marked with yellow, signals arriving last with red), while the size of the markers is proportional to the logarithm of the signal. Figures from [26].	29
2.6	Schematic view of a FD telescope with its components. Figure from [26].	30
2.7	A camera reflected on the segmented mirror (a) and a camera with the aperture system behind it (b) at the Coihueco site. Personal photos. . .	31
2.8	Fundamental patterns of the SLT. They are used together with their rotation and reflection. Figure from [39].	32
2.9	Schematic views of a drum mounted in a telescope aperture (a) and positions of light sources for three different relative calibrations (b). Figures from [39].	33
2.10	An event corresponding to a cosmic ray shower as seen on an event display of the camera is shown in Figure (a). The activated pixels are shown in the left panel, while the response of the selected pixels (marked by black dots) as a function of time is shown in the right panel. The bin size is 100 ns. A background event most likely due to cosmic ray muon interacting with the glass of the PMT is shown in Figure (b). The event is not compatible with a cosmic ray shower because all the activated pixels give a signal in the same time. Figures from [39].	34
2.11	Geometrical reconstruction of an event with a fluorescence telescope. Figure from [40].	35

LIST OF FIGURES

2.12	Light measured at the aperture as a function of time with the reconstructed light contributions (a) and the the energy deposit as a function of the slant depth (b) obtained from the light at the aperture shown in (a). Figures from [39].	37
2.13	View from the top of the Coihueco building as seen in two different periods, showing the importance of a continuous monitoring of the atmosphere. The presence of diffuse smoke is visible in picture (a), which was taken on 18th January 2020. As a reference, the same view as seen in a clean day is shown in picture (b), which was taken on 7th March 2019. On the left side of both pictures the lidar station of the Coihueco site is also visible. Personal photos.	38
2.14	HEAT as seen from the top of the Coihueco building overlooking the SD array (a) and close view of the HEAT telescopes in tilted orientation (b). Personal photos.	39
2.15	Schematic view of a HEAT telescope in horizontal mode, which is used for service and cross calibration, (a) and tilted mode, which is used for data taking (b). Figures from [26].	40
2.16	Map of the AMIGA infill with the Unitary Cell (shaded area). Figure from [26].	41
2.17	An AERA station with a logarithmic periodic dipole antenna (left) and an AERA station with a butterfly antenna (right). Figure from [54]. . .	42
2.18	The layout of the SSD. The enclosing box, the scintillator bars, the fibers and the PMT are visible. Figure from [59].	43
3.1	Distribution of the PCA variable for the data (blue) and the MC photons (orange). The cut at 50% efficiency on the MC photon distribution is indicated by the the black line. 11 data events are above the cut value. Figure from [79].	47
3.2	BDT output variable distribution for the simulated photon signal (blue), the simulated proton background (red), and the data-set (black). Both the training and the test samples are shown for simulations. The dashed line represents the cut at 50% efficiency on the photon distribution. Figure from [79].	48
3.3	Upper limits on the photon flux at 95% confidence level obtained with the Pierre Auger Observatory. Predictions from models [87, 88, 89] and other experimental results at 95% (TA [90]) or 90% (KASCADE-Grande [91], EAS-MSU [92]) confidence level are also shown. Figure from [79]. .	49

3.4	Photon energy spectrum from the region of the Galactic center as measured by the H.E.S.S. Collaboration [96] (red points) together with the extrapolations in the EeV range (dashed lines) and the Auger upper limit (green line). The green and blue bands are obtained by varying the spectral index by ± 0.11 according to the systematics of the H.E.S.S. measurement. The dashed black line represents the extrapolation obtained by assuming an exponential cutoff with $E_{\text{cut}} = 2.0$ EeV, which is the upper limit of the cutoff energy derived from the upper limit on the flux. Figure from [95].	51
3.5	Preliminary upper limits at 90% confidence level on the spectral fluence for the four gravitational wave sources reported in the text. The uncertainties due to the limited sky localization of the sources (blue bars) and the variation of the spectral index α in the range $[-2.3, -1.7]$ (red bars) are also shown. The central value of the upper limit for GW170818 is not shown because its sky localization is close to the edge of the field of view. Figure from [99].	53
3.6	A footprint of an inclined shower on SD stations (a) and the FADC trace in a SD station for a dominant electromagnetic signal with its electromagnetic and muonic components (b). Following the same convention as Figure 2.5(a), the different colors in Figure (a) refer to the time arrival of the shower front (signal arriving first are marked with yellow, signals arriving last with red), while the size of the markers is proportional to the logarithm of the signal. The AoP ratio of a dominant muonic signal is larger than that of a dominant electromagnetic signal, as clearly visible in Figure (b). Figures from [105].	54
3.7	Distribution of $\langle \text{AoP} \rangle$ for the data in the whole period considered in the analysis (black histogram) and the simulated Earth-skimming tau neutrinos events (red shaded histogram). The $\langle \text{AoP} \rangle$ optimized cut value is represented by the black line. Figure from [106].	55
3.8	Distribution of the Fisher variable for the data in the period from 1 January 2004 to 31 August 2018 (black histograms) and the simulated downward-going neutrino events (blue shaded histogram in Figure (a) and green shaded histogram in Figure (b)). The optimized cut value on the Fisher variable is represented by the black line. Figure (a) refers to the sub-sample of nearly horizontal upward-going showers with a number of triggered stations between 7 and 11, while Figure (b) refers to the sub-sample of inclined downward-going showers with a reconstructed zenith angle θ_{rec} in the range $(58.5, 76.5]^\circ$. Figures from [106].	57

LIST OF FIGURES

3.9 Exposure of the SD to ultra high energy neutrinos as a function of the neutrino energy in the period from 1 January 2004 to 31 August 2018. The total exposure is represented by the black solid line. Exposures for Earth-skimming tau neutrinos only (red dashed line), all flavors downward-going neutrinos (blue dashed line), downward-going electron neutrinos (green dashed line), downward-going muon neutrinos (purple dashed line) and Earth-skimming and downward-going tau neutrinos (pink dashed line) are also shown. The exposures are obtained assuming a flavor ratio of 1:1:1. Figure from [106]. 58

3.10 Upper limits on k at 90% confidence level from the Pierre Auger Observatory. The integrated upper limit is represented by the solid straight red line, while the differential upper limits for all channels and flavors and for Earth-skimming tau neutrinos are represented by the solid red line and the dashed red line, respectively. The differential limits from IceCube [109] (solid green line) and ANITA I+II+III [110] (solid dark magenta line) are also shown. The expected neutrino fluxes from different cosmogenic and astrophysical models of neutrino production [111, 112, 113, 114], as well as the Waxman-Bahcall bound [115], which is derived from the observed cosmic ray flux, have also been added to the plot. All limits and fluxes are converted to single flavor. Figure from [106]. 59

3.11 Instantaneous field of view (FoV) of the Pierre Auger Observatory for Earth-skimming neutrinos (red band), inclined downward-going neutrinos with a zenith angle in the range $[75, 90]^\circ$ (blue band) and inclined downward-going neutrinos with a zenith angle in the range $[60, 75]^\circ$ (green band) as a function of the hour angle $\alpha - t_{\text{GS}}$. The declination range for a given location in right ascension α at a given GST converted to angle t_{GS} can be directly read at the corresponding hour angle $\alpha - t_{\text{GS}}$. As an example, the positions of two sources are shown: GW170817 visible in Auger in the Earth-skimming channel at the time of emission [65], and GRB 190114C [118] not visible in the different channels of Auger at the time of the burst. Figure from [119]. 60

3.12 Upper limits at 90% confidence level on k_{PS} for a single flavor point-like neutrino flux as a function of the source declination δ obtained with the Pierre Auger Observatory for all channels and flavors (solid black line) and for Earth-skimming neutrinos (dashed red line), inclined downward-going neutrinos with a zenith angle in the range $[75, 90]^\circ$ (dashed blue line) and inclined downward-going neutrinos with a zenith angle in the range $[60, 75]^\circ$ (dashed green line). The upper limits obtained by IceCube (2008-2015) [120] and ANTARES (2007-2015) [121] in different energy ranges are also shown. Figure from [119]. 61

3.13	Upper limits at 90% confidence level on the ultra high energy neutrino spectral fluence per flavor from GW150914 as a function of the declination δ . The declination values corresponding to the 90% confidence level region of the source localization in the sky for GW150914 are represented by the blue bands. Figure from [123].	62
3.14	Upper limits at 90% confidence level on the neutrino spectral fluence from GW170817 during the time window of 500 s before and after the merger (upper plot), and the 14-day period after the merger (lower plot). Assuming a spectral fluence $F = F_{up} \cdot (E_\nu/\text{GeV})^{-2}$, upper limits on F_{up} are calculated separately for each energy bin. Predictions from neutrino emission models are also shown. The upper limits in the upper plot are compared with the predictions from models of prompt emission and extended emission (EE) [126] for the case of line of sight aligned with the rotation axis and for different off-axis viewing angles. The upper limits in the lower plot, on the other hand, are compared with the predictions from models for longer lived emission [127]. The models shown in both the plots are scaled to 40 Mpc, which is the distance of the galaxy NGC 4993 where the merger is localized. Assuming that all flavors have the same fluence, as expected from the standard neutrino oscillation, all fluences are shown as the per flavor sum of neutrino and anti-neutrino fluence. Figure from [65].	63
3.15	Schematic view of the different classes of events that can be detected with the ANITA experiment. Figure from http://www.hep.ucl.ac.uk/uhen/anita/	66
3.16	Overlay of 16 UHECR event Hpol pulse shapes. The phase of the 14 reflected events (blue) is inverted with respect to that of the 2 direct events (red). In the top right box the average pulse profiles for reflected and direct events are shown. Figure from [134].	67
3.17	Pulse shapes of the two anomalous events detected by ANITA during its first (a) and third (b) flights. The two events have elevation angles of $27.4 \pm 0.3^\circ$ (a) and $35.0 \pm 0.3^\circ$ (b), while their energies are above ~ 0.2 EeV. The signals are characterized by a horizontal polarization and a non-inverted phase, being consistent with the interpretation of upward-going showers coming directly from the ground. Figure (a) is from [60], while Figure (b) is from [61].	68
4.1	Schematic view of the generation geometry of an upward-going shower. D is the distance along the shower axis of the point of first interaction of the primary particle from the exit point, the injection point is the point at which the primary particle arises and H_{fi} is the height of the point of first interaction with respect to the ground. Figure from [140].	72

LIST OF FIGURES

4.2	X_{\max} distributions for different primary nuclei (Iron, Calcium, Silicium, Nitrogen, Helium, Hydrogen) with energy $E = 10^{18}$ eV, obtained using the hadronic interaction model EPOS-LHC. The lower the nuclear mass A , the higher the value of X_{\max} the distribution is peaked at.	75
4.3	X_{\max} distributions for primary hydrogen nuclei with different energies (10^{17} eV, $10^{17.5}$ eV, 10^{18} eV, $10^{18.5}$ eV, 10^{19} eV), obtained using the hadronic interaction model EPOS-LHC. The higher the energy E , the higher the value of X_{\max} the distribution is peaked at.	75
4.4	X_{\max} distributions for a primary hydrogen nucleus with energy $E = 10^{18}$ eV, obtained using different hadronic interaction models (EPOS-LHC, SIBYLL 2.3c, QGSJET II-04).	76
4.5	Top view of the generation area of $200 \text{ km} \times 200 \text{ km}$ centered at one FD site, with the dark gray area representing the azimuthal field of view of the FD (a), and elevation field of view (FoV) of one FD site, with the light and dark gray areas representing, respectively, the standard field of view of the FD, which is in common between the four FD sites, and the additional field of view considered in order to take into account also the presence of HEAT (b).	77
4.6	A schematic top view (a) and side view (b) of an upward-going event that can be potentially detected by the FD. The point P_{\max} corresponds to the position of the X_{\max} along the shower axis, while d_{\max} represents the distance between the FD site and the projection of P_{\max} on the generation area. For simplicity, only the standard FD field of view is shown. The event is considered detected by the FD if P_{\max} is inside the FD field of view and d_{\max} is less than $R_{\text{cut}}(E)$, where E is the energy of the primary particle.	78
4.7	Detection efficiency as a function of the position (x, y) of the exit points on the generation area for the case with only the standard FD field of view considered (a) and the case with also the HEAT field of view considered (b). The negative values on the y -axis correspond to the portion of the generation area behind the FD site. The sensitive area extends between -20 km and 50 km on the y -axis. The detection efficiency increases if also the HEAT field of view is considered. Given the configuration of the four FD sites, a generation area of $100 \text{ km} \times 100 \text{ km}$ centered at the SD station closest to the center of the SD array has been chosen for the Real Monte Carlo simulation.	80
4.8	Detection efficiency as a function of the distance between the exit point and the FD site considering only the generated and triggered events with an injection height H_{inj} in a specific interval. Both the case with only the standard FD field of view (a) and the case with the addition of the HEAT one (b) are shown. The inclusion of the HEAT field of view allows the FD site to be more sensitive to upward-going showers with higher injection heights.	81

4.9	Distribution of $\cos^2 \theta$ before (a) and after (b) the weighting procedure. The distribution without weights (a) refers to the case with uniformly distributed zenith angles. The weighting procedure allows to have a flat distribution in $\cos^2 \theta$. Both distributions are normalized.	82
4.10	Detection efficiency as a function of $\log_{10}(E/\text{eV})$ and $ \cos \theta $ for the case with only the standard FD field of view (a) and the case with the addition of the HEAT one (b). For a given primary energy, the addition of the HEAT field of view increases the sensitivity of the FD site to upward-going showers with larger zenith angles i.e. more vertical upward-going showers. It is important to notice that the range of the z-axis is different for (a) and (b).	83
4.11	Exposure of a single FD site as a function of the energy for the case with only the standard FD field of view (a) and the case with the addition of the HEAT one (b). The uncertainties on the values of the exposure are also included, but they are too small to be appreciated with the scale used for the y-axis. The addition of the HEAT field of view allows to significantly increase the sensitivity to upward-going showers at low energies.	86
4.12	Total FD exposure obtained from those shown in Figure 4.11(a) and Figure 4.11(b), as described in the text. Also in this case, the uncertainties on the values of the exposure are included, but they can not be appreciated. Given the assumptions used in the fast Monte carlo simulation and in the exposure calculation, this estimate is an overestimation of the real exposure, as will be confirmed in Chapter 5.	87
5.1	Downward-going proton induced shower simulated with CONEX and reconstructed within the Offline. The event has been detected by one of the telescopes of Coihueco and is shown as seen in the viewer of the Offline. The activated pixels on the camera of the telescope (top left panel), the arrival time of the light on the single pixels as a function of their χ (top right panel), the reconstructed longitudinal profile of the shower (bottom left panel) and the parameters from the reconstruction (bottom right panel) are shown. The colors in the top right and top left panel refer to the progression of the arrival time of the light (blue for early pixels, red for late pixels). In the bottom right panel, the values used in the simulation are displayed in square brackets.	90
5.2	Upward-going proton induced shower simulated with CONEX and reconstructed within the Offline. Also in this case, the event has been detected by one of the telescopes of Coihueco and is shown as seen in the viewer of the Offline. The same panels as Figure 5.1 are shown. The progression of the arrival time of the light on the single pixels is inverted with respect to that of the event shown in Figure 5.1.	91

LIST OF FIGURES

5.3	FD detection efficiency as a function of $\log_{10}(E/\text{eV})$ and $ \cos\theta $ (a) and FD exposure as a function of the simulated primary energy (b), both obtained from the Real Monte Carlo simulation without applying any selection cut.	93
5.4	FD detection efficiency as a function of $\log_{10}(E_{\text{cal}}/\text{eV})$ and $ \cos\theta $ (a) and FD exposure as a function of the simulated calorimetric energy (b), both obtained from the Real Monte Carlo simulation without applying any selection cut. The Pierre Auger Observatory is sensitive to upward-going showers also at low calorimetric energies, at least when no selection cuts are applied.	93
5.5	FD detection efficiency as a function of the position (x, y) of the exit points on the generation area of $100 \text{ km} \times 100 \text{ km}$ used in the Real Monte Carlo simulation. The point $(0, 0)$ corresponds to the position of the SD station closest to the center of the SD array. Also the positions of the four FD sites, Los Leones (LL), Los Morados (LM), Loma Amarilla (LA) and Coihueco (CO), are shown. The geometrical configuration of the FD reflects the one shown in Figure 2.1. The plot has been obtained considering only the events with a simulated primary energy in the region $\log_{10}(E/\text{eV}) \in [17, 18.5]$, without applying any selection cut.	94
5.6	Schematic view of the geometry of a downward-going event that is reconstructed as an upward-going event. For the two points P_1 and P_2 on the shower axis $\alpha_1 < \alpha_2$ and $h_1 > h_2$. The signal from P_1 reaches the FD before the signal from P_2 and the event can be reconstructed as an upward-going event. Figure from [140].	95
5.7	Generation geometry used for the background simulation. The cores P of the downward-going showers are simulated in a sphere of radius 90 km centered at the center of the SD array O and then projected onto the ground along the direction of the shower axis. This allows to simulate also showers with a core far away from the FD.	95
5.8	A downward-going shower simulated with a zenith angle smaller than 90° ($\theta = 76.5^\circ$) and reconstructed as an upward-going shower ($\theta = 115.5^\circ$) in the monocular reconstruction defined in section 2.2.4.	96
5.9	Scans in χ_0 performed using the PCGFdown reconstruction (a) and the PCGFup reconstruction (b) on the background event shown in Figure 5.8. For clarity, only the χ_0 region where the minimum χ^2 has been found is shown for both the scans. For this event, the two reconstructions result in $L_{\text{down}} > L_{\text{up}}$	97
5.10	Scans in χ_0 performed using the PCGFdown reconstruction (a) and the PCGFup reconstruction (b) on the signal event shown in Figure 5.2. Also in this case, only the χ_0 region where the minimum χ^2 has been found is shown. In contrast to the background event of Figure 5.8, this event is characterized by $L_{\text{down}} \ll L_{\text{up}}$	98

5.11 Distribution of l for the burn data sample, the background and the signal simulations with all the selection criteria defined in section 5.4 applied. The background simulation includes the events in the simulated energy range $\log_{10}(E/\text{eV}) \in [17, 20]$ and has been weighted to the cosmic ray energy spectrum measured by the Pierre Auger Observatory (see section 1.2) and normalized to the burn data sample i.e. the total number of events has been divided by 10 because the burn data sample consists of the 10% of the data. The uncertainties on the entries of the background distribution have been calculated using the Poisson statistics to properly take into account the statistics of small numbers. The signal simulation has not been weighted because the energy spectrum of this class of events is not known. It includes the events with a simulated calorimetric energy in the range $\log_{10}(E_{\text{cal}}/\text{eV}) \in [16.5, 18.5]$. Figure from [140]. 102

5.12 Distribution of l for the background simulation fitted with the functions $\exp(ax + b)$ (a) and $\exp(ax^2 + bx + c)$ (b) via the weighted log likelihood method. The background simulation has been weighted according to the cosmic ray energy spectrum measured by the Pierre Auger Observatory but not to the burn data sample. All the background events in the simulated energy range $\log_{10}(E/\text{eV}) \in [17, 20]$ passing the selection criteria defined in section 5.4 have been considered. These are two of the parameterization that have been used to perform the upper limit minimization described in the text. Figure (a) is from [140]. 103

5.13 Integral upper limit as a function of l for $E_{\text{cal}} > 10^{17.5}$ eV obtained by fitting the background distribution with the functions $\exp(ax + b)$ (a) and $\exp(ax^2 + bx + c)$ (b). The power-law indices $\gamma = 1$ and $\gamma = 2$ have been used for the energy spectrum in the calculation of the average exposure, since the energy spectrum of the signal events is not known. The integral upper limit has been calculated considering the background events in the whole energy range of simulation ($\log_{10}(E/\text{eV}) \in [17, 20]$). The minimum value of the integral upper limit has been found at $l = 0.55$ for (a) and $l = 0.70$ for (b) (dashed gray lines). The bump observed before the minimum value of the integral upper limit is due to the fact that the number of observed events has to be an integer number and thus it is rounded to the integer value closest to the number of events expected from background. Figure (a) is from [140]. 104

5.14 FD detection efficiency as a function of the position (x, y) of the exit points on the generation area of $100 \text{ km} \times 100 \text{ km}$ used in the Real Monte Carlo simulation for the case of no selection criteria applied (a) and all selection cuts applied (b). The detection efficiency in (a) is not the same as Figure 5.5 because in this case only the events with a simulated calorimetric energy in the region $\log_{10}(E_{\text{cal}}/\text{eV}) \in [16.5, 18.5]$ have been considered. The point $(0, 0)$ corresponds to the position of the SD station closest to the center of the SD array. 106

LIST OF FIGURES

5.15	FD detection efficiency as a function of $\log_{10}(E_{\text{cal}}/\text{eV})$ and $ \cos\theta $ (a) and FD exposure as a function of $\log_{10}(E_{\text{cal}}/\text{eV})$ (b), both obtained from the Real Monte Carlo simulation applying all the selection cuts defined in the text.	107
5.16	Double differential exposure obtained according to Eq. 5.6 as a function of H_{fi} and $\log_{10}(E_{\text{cal}}/\text{eV})$ and for different ranges of zenith angles ($\theta \in [110, 180]^\circ$ (a), $\theta \in [110, 124.2]^\circ$ (b), $\theta \in [124.2, 141.3]^\circ$ (c), $\theta \in [141.3, 180]^\circ$ (d)). The exposure calculation refers to a flat generation in H_{fi} and an isotropic emergence. The uncertainties on the values of the exposure has been calculated using the Poisson statistics. Figures from [140].	110
A.1	Schematic view of the experimental setup used to measure the linearity of the two Hamamatsu R9420 PMTs. Figure from [159].	114
A.2	Percentage non-linearity of the PMT 3851 as a function of the anode current for different values of the supply voltage V ($V = 800 \text{ V}$, $V = 900 \text{ V}$, $V = 1100 \text{ V}$, $V = 1300 \text{ V}$, $V = 1500 \text{ V}$).	115
A.3	Percentage non-linearity of the PMT 4151 as a function of the anode current for different values of the supply voltage V ($V = 800 \text{ V}$, $V = 900 \text{ V}$, $V = 1100 \text{ V}$, $V = 1300 \text{ V}$, $V = 1500 \text{ V}$).	116
A.4	Gain as a function of the supply voltage for the PMT 3851 (left) and the PMT 4151 (right).	117
A.5	Anode current at which the percentage non-linearity is $\pm 5\%$ as a function of the gain for the PMT 3851 (left) and the PMT 4151 (right).	117
A.6	Result of the fit performed using the function in Eq. A.2 on the anode current at which the percentage non-linearity is $\pm 5\%$ as a function of the gain for the PMT 3851 (left) and the PMT 4151 (right). The fitting function well reproduces the behaviour of the data.	117
B.1	A hadron-hadron scattering as multiple exchange of parton ladders (a) and a typical contribution to hadron-hadron scattering amplitude with elementary re-scatterings treated as exchanges of Pomerons (b). Figures from [166].	120
B.2	A general Pomeron as the sum of a soft and a semi-hard Pomeron. The semi-hard Pomeron is represented as a QCD ladder between two soft Pomerons. Figure from [166].	120
B.3	A pomeron as a two layer parton ladder attached to projectile and target remnants through two color singlets (left) and a cut Pomeron seen as two strings (right). Figures from [175].	121

List of Tables

- 4.1 Parameters used in the parameterization of the X_{\max} distributions for different hadronic interaction models. Parameterizations from [149]. . . 74

LIST OF TABLES

Bibliography

- [1] D. Pacini. La radiazione penetrante alla superficie ed in seno alle acque. *Il Nuovo Cimento (1911-1923)*, 3:93–100, 1912.
- [2] Victor F. Hess. Über Beobachtungen der durchdringenden Strahlung bei sieben Freiballonfahrten. *Phys. Z.*, 13:1084–1091, 1912.
- [3] R. A. Millikan. High frequency rays of cosmic origin. *Proceedings of the National Academy of Sciences*, 12(1):48–55, 1926.
- [4] P.A. Zyla et al. Review of Particle Physics. *PTEP*, 2020(8):083C01, 2020.
- [5] A. Aab et al. Measurement of the cosmic-ray energy spectrum above 2.5×10^{18} eV using the pierre auger observatory. *Phys. Rev. D*, 102:062005, Sep 2020.
- [6] A. Aab et al. Features of the energy spectrum of cosmic rays above 2.5×10^{18} eV using the pierre auger observatory. *Phys. Rev. Lett.*, 125:121106, Sep 2020.
- [7] Enrico Fermi. On the origin of the cosmic radiation. *Phys. Rev.*, 75:1169–1174, Apr 1949.
- [8] A. R. Bell. The acceleration of cosmic rays in shock fronts – I. *Monthly Notices of the Royal Astronomical Society*, 182(2):147–156, 02 1978.
- [9] A. M. Hillas. The origin of ultra-high-energy cosmic rays. *Annual Review of Astronomy and Astrophysics*, 22(1):425–444, 1984.
- [10] Kumiko Kotera and Angela V. Olinto. The astrophysics of ultrahigh-energy cosmic rays. *Annual Review of Astronomy and Astrophysics*, 49(1):119–153, 2011.
- [11] Mikhail V. Medvedev and Viktor V. Medvedev. Asymmetric diffusion of cosmic rays. *Physics of Plasmas*, 22(9):091504, 2015.
- [12] James W. Cronin. The highest-energy cosmic rays. *Nuclear Physics B - Proceedings Supplements*, 138:465–491, 2005.
- [13] Kenneth Greisen. End to the cosmic-ray spectrum? *Phys. Rev. Lett.*, 16:748–750, Apr 1966.

BIBLIOGRAPHY

- [14] G. T. Zatsepin and V. A. Kuzmin. Upper limit of the spectrum of cosmic rays. *JETP Lett.*, 4:78–80, 1966.
- [15] Malcolm S. Longair. *High Energy Astrophysics*. Cambridge University Press, 2011.
- [16] V. Berezhinsky, A. Z. Gazizov, and S. I. Grigorieva. On astrophysical solution to ultrahigh-energy cosmic rays. *Phys. Rev. D*, 74:043005, 2006.
- [17] R. Aloisio, V. Berezhinsky, and A. Gazizov. Ultra High Energy Cosmic Rays: The disappointing model. *Astropart. Phys.*, 34:620–626, 2011.
- [18] Daniele Fargion and B. Mele. Scattering of ultrahigh-energy (UHE) extragalactic neutrinos onto light relic neutrinos in galactic HDM halo overcoming the GZK cutoff. In *2nd International Workshop on the Identification of Dark Matter*, 9 1998.
- [19] A. De Angelis and M.J.M. Pimenta. *Introduction to Particle and Astroparticle Physics: Questions to Universe*. Undergraduate Lecture Notes in Physics. Springer Milan, 2015.
- [20] Giuseppe Di Sciascio. Detection of Cosmic Rays from ground: an Introduction. *J. Phys. Conf. Ser.*, 1263(1):012002, 2019.
- [21] W. Heitler. *The quantum theory of radiation*, volume 5 of *International Series of Monographs on Physics*. Oxford University Press, Oxford, 1936.
- [22] J. Matthews. A Heitler model of extensive air showers. *Astropart. Phys.*, 22:387–397, 2005.
- [23] L. G. Dedenko. A new method of solving the nuclear cascade equation. In *International Cosmic Ray Conference*, volume 1 of *International Cosmic Ray Conference*, page 662, January 1965.
- [24] G. Bossard, H. J. Drescher, N. N. Kalmykov, S. Ostapchenko, A. I. Pavlov, T. Pierog, E. A. Vishnevskaya, and K. Werner. Cosmic ray air shower characteristics in the framework of the parton based Gribov-Regge model NEXUS. *Phys. Rev. D*, 63:054030, 2001.
- [25] Ralph Engel, Dieter Heck, and Tanguy Pierog. Extensive air showers and hadronic interactions at high energy. *Annual Review of Nuclear and Particle Science*, 61(1):467–489, 2011.
- [26] Alexander Aab et al. The Pierre Auger Cosmic Ray Observatory. *Nucl. Instrum. Meth. A*, 798:172–213, 2015.
- [27] I. Allekotte et al. The Surface Detector System of the Pierre Auger Observatory. *Nucl. Instrum. Meth. A*, 586:409–420, 2008.

- [28] D. Allard et al. Aperture calculation of the Pierre Auger Observatory surface detector. In *29th International Cosmic Ray Conference*, 8 2005.
- [29] Jakub Víchá and J. Chudoba. Data Processing at the Pierre Auger Observatory. *J. Phys. Conf. Ser.*, 608(1):012077, 2015.
- [30] J. Abraham et al. Properties and performance of the prototype instrument for the Pierre Auger Observatory. *Nucl. Instrum. Meth. A*, 523:50–95, 2004.
- [31] A. K. Tripathi et al. Simulation of Pierre Auger surface detector response to muons. In *28th International Cosmic Ray Conference*, 7 2003.
- [32] X. Bertou et al. Calibration of the surface array of the Pierre Auger Observatory. *Nucl. Instrum. Meth. A*, 568:839–846, 2006.
- [33] J. Abraham et al. Trigger and Aperture of the Surface Detector Array of the Pierre Auger Observatory. *Nucl. Instrum. Meth. A*, 613:29–39, 2010.
- [34] David Newton, J. Knapp, and A. A. Watson. The Optimum Distance at which to Determine the Size of a Giant Air Shower. *Astropart. Phys.*, 26:414–419, 2007.
- [35] C. Bonifazi. The angular resolution of the pierre auger observatory. *Nuclear Physics B - Proceedings Supplements*, 190:20–25, 2009. Proceedings of the Cosmic Ray International Seminars.
- [36] J. Hersil, I. Escobar, D. Scott, G. Clark, and S. Olbert. Observations of Extensive Air Showers near the Maximum of Their Longitudinal Development. *Phys. Rev. Lett.*, 6:22–23, 1961.
- [37] Alexander Aab et al. Measurement of the cosmic-ray energy spectrum above 2.5×10^{18} eV using the Pierre Auger Observatory. *Phys. Rev. D*, 102(6):062005, 2020.
- [38] Alexander Aab et al. Reconstruction of Inclined Air Showers Detected with the Pierre Auger Observatory. *JCAP*, 08:019, 2014.
- [39] J. Abraham et al. The Fluorescence Detector of the Pierre Auger Observatory. *Nucl. Instrum. Meth. A*, 620:227–251, 2010.
- [40] D. Kuempel, K. H. Kampert, and M. Risse. Geometry reconstruction of fluorescence detectors revisited. *Astropart. Phys.*, 30:167–174, 2008.
- [41] P. Privitera. The angular reconstruction and angular resolution of air showers detected at the Auger Observatory. In *28th International Cosmic Ray Conference*, pages 357–360, 7 2003.
- [42] S. J. Sciutto. AIRES: A system for air shower simulations. 11 1999.

BIBLIOGRAPHY

- [43] T. K. Gaisser and A. M. Hillas. Reliability of the Method of Constant Intensity Cuts for Reconstructing the Average Development of Vertical Showers. In *International Cosmic Ray Conference*, volume 8 of *International Cosmic Ray Conference*, page 353, January 1977.
- [44] Bianca Keilhauer and Martin Will. Atmospheric monitoring and model applications at the Pierre Auger Observatory. *EPJ Web Conf.*, 89:02001, 2015.
- [45] J. Abraham et al. A Study of the Effect of Molecular and Aerosol Conditions in the Atmosphere on Air Fluorescence Measurements at the Pierre Auger Observatory. *Astropart. Phys.*, 33:108–129, 2010.
- [46] Johana Chirinos. Cloud Monitoring at the Pierre Auger Observatory. In *33rd International Cosmic Ray Conference*, page 0994, 2013.
- [47] Bianca Keilhauer, J. Blumer, R. Engel, H. O. Klages, and M. Risse. Impact of varying atmospheric profiles on extensive air shower observation: - Atmospheric density and primary mass reconstruction. *Astropart. Phys.*, 22:249–261, 2004.
- [48] P. Abreu et al. Description of Atmospheric Conditions at the Pierre Auger Observatory using the Global Data Assimilation System (GDAS). *Astropart. Phys.*, 35:591–607, 2012.
- [49] Pedro Abreu et al. Techniques for Measuring Aerosol Attenuation using the Central Laser Facility at the Pierre Auger Observatory. *JINST*, 8:P04009, 2013.
- [50] P. Abreu et al. The Pierre Auger Observatory V: Enhancements. In *32nd International Cosmic Ray Conference*, 7 2011.
- [51] Alexander Aab et al. Design, upgrade and characterization of the silicon photo-multiplier front-end for the AMIGA detector at the Pierre Auger Observatory. *JINST*, 16(01):P01026, 2021.
- [52] Franz Daniel Kahn, I. Lerche, and Alfred Charles Bernard Lovell. Radiation from cosmic ray air showers. *Proceedings of the Royal Society of London. Series A. Mathematical and Physical Sciences*, 289(1417):206–213, 1966.
- [53] G. A. Askar’yan. Excess negative charge of an electron-photon shower and its coherent radio emission. *Zh. Eksp. Teor. Fiz.*, 41:616–618, 1961.
- [54] Christian Glaser. Results and Perspectives of the Auger Engineering Radio Array. *EPJ Web Conf.*, 135:01006, 2017.
- [55] Ewa M. Holt. Recent Results of the Auger Engineering Radio Array (AERA). *PoS, ICRC2017:492*, 2018.
- [56] Alexander Aab et al. Energy Estimation of Cosmic Rays with the Engineering Radio Array of the Pierre Auger Observatory. *Phys. Rev. D*, 93(12):122005, 2016.

-
- [57] Ewa M. Holt. The Auger Engineering Radio Array and multi-hybrid cosmic ray detection. *J. Phys. Conf. Ser.*, 718(5):052019, 2016.
- [58] Alexander Aab et al. The Pierre Auger Observatory Upgrade - Preliminary Design Report. 4 2016.
- [59] Daniele Martello. The Pierre Auger Observatory Upgrade. pages 147–154, 2017.
- [60] P. W. Gorham et al. Characteristics of Four Upward-pointing Cosmic-ray-like Events Observed with ANITA. *Phys. Rev. Lett.*, 117(7):071101, 2016.
- [61] P. W. Gorham et al. Observation of an Unusual Upward-going Cosmic-ray-like Event in the Third Flight of ANITA. *Phys. Rev. Lett.*, 121(16):161102, 2018.
- [62] B. P. Abbott et al. Observation of Gravitational Waves from a Binary Black Hole Merger. *Phys. Rev. Lett.*, 116(6):061102, 2016.
- [63] B. P. Abbott et al. GW170817: Observation of Gravitational Waves from a Binary Neutron Star Inspiral. *Phys. Rev. Lett.*, 119(16):161101, 2017.
- [64] B. P. Abbott et al. Multi-messenger Observations of a Binary Neutron Star Merger. *Astrophys. J. Lett.*, 848(2):L12, 2017.
- [65] A. Albert et al. Search for High-energy Neutrinos from Binary Neutron Star Merger GW170817 with ANTARES, IceCube, and the Pierre Auger Observatory. *Astrophys. J. Lett.*, 850(2):L35, 2017.
- [66] M. G. Aartsen et al. Multimessenger observations of a flaring blazar coincident with high-energy neutrino IceCube-170922A. *Science*, 361(6398):eaat1378, 2018.
- [67] M. G. Aartsen et al. Neutrino emission from the direction of the blazar TXS 0506+056 prior to the IceCube-170922A alert. *Science*, 361(6398):147–151, 2018.
- [68] Alexander Aab et al. Multi-Messenger Physics with the Pierre Auger Observatory. *Front. Astron. Space Sci.*, 6:24, 2019.
- [69] Pijushpani Bhattacharjee and Gunter Sigl. Origin and propagation of extremely high-energy cosmic rays. *Phys. Rept.*, 327:109–247, 2000.
- [70] R. Aloisio, S. Matarrese, and A. V. Olinto. Super Heavy Dark Matter in light of BICEP2, Planck and Ultra High Energy Cosmic Rays Observations. *JCAP*, 08:024, 2015.
- [71] Z. Fodor, S. D. Katz, and A. Ringwald. Z burst scenario for the highest energy cosmic rays. In *Conference on Physics Beyond the Standard Model: Beyond the Desert 02*, pages 567–587, 10 2002.
- [72] Alessandro De Angelis, Giorgio Galanti, and Marco Roncadelli. Transparency of the Universe to gamma rays. *Mon. Not. Roy. Astron. Soc.*, 432:3245–3249, 2013.

BIBLIOGRAPHY

- [73] L. D. Landau and I. Pomeranchuk. Limits of applicability of the theory of bremsstrahlung electrons and pair production at high-energies. *Dokl. Akad. Nauk Ser. Fiz.*, 92:535–536, 1953.
- [74] A. B. Migdal. Bremsstrahlung and pair production in condensed media at high-energies. *Phys. Rev.*, 103:1811–1820, 1956.
- [75] Thomas Erber. High-energy electromagnetic conversion processes in intense magnetic fields. *Rev. Mod. Phys.*, 38:626–659, 1966.
- [76] B. Mcbreen and C. J. Lambert. Interactions of High-energy ($E > 5 \times 10^{19}$ -eV) Photons in the Earth’s Magnetic Field. *Phys. Rev. D*, 24:2536–2538, 1981.
- [77] P. Homola, Markus Risse, R. Engel, D. Gora, J. Pekala, B. Wilczynska, and H. Wilczynski. Characteristics of geomagnetic cascading of ultrahigh energy photons at the southern and northern sites of the Pierre Auger Observatory. *Astropart. Phys.*, 27:174–184, 2007.
- [78] P. Abreu et al. The Lateral Trigger Probability function for the ultra-high energy cosmic ray showers detected by the Pierre Auger Observatory. *Astropart. Phys.*, 35:266–276, 2011. [Erratum: *Astropart. Phys.* 35, 681–684 (2012)].
- [79] Julian Rautenberg. Limits on ultra-high energy photons with the Pierre Auger Observatory. *PoS, ICRC2019:398*, 2021.
- [80] J. Abraham et al. Upper limit on the cosmic-ray photon flux above 10^{19} eV using the surface detector of the Pierre Auger Observatory. *Astropart. Phys.*, 29:243–256, 2008.
- [81] G. Ros, A. D. Supanitsky, G. A. Medina-Tanco, L. del Peral, J. C. D’Olivo, and M. D. Rodríguez Frías. A new composition-sensitive parameter for ultra-high energy cosmic rays. *Astroparticle Physics*, 35(3):140–151, October 2011.
- [82] A. Aab et al. Depth of maximum of air-shower profiles at the Pierre Auger Observatory. II. Composition implications. *Phys. Rev. D*, 90(12):122006, 2014.
- [83] Alexander Aab et al. Muons in Air Showers at the Pierre Auger Observatory: Mean Number in Highly Inclined Events. *Phys. Rev. D*, 91(3):032003, 2015. [Erratum: *Phys.Rev.D* 91, 059901 (2015)].
- [84] Alexander Aab et al. Testing Hadronic Interactions at Ultrahigh Energies with Air Showers Measured by the Pierre Auger Observatory. *Phys. Rev. Lett.*, 117(19):192001, 2016.
- [85] Alexander Aab et al. Search for photons with energies above 10^{18} eV using the hybrid detector of the Pierre Auger Observatory. *JCAP*, 04:009, 2017. [Erratum: *JCAP* 09, E02 (2020)].

-
- [86] Gary J. Feldman and Robert D. Cousins. A Unified approach to the classical statistical analysis of small signals. *Phys. Rev. D*, 57:3873–3889, 1998.
- [87] Graciela Gelmini, Oleg E. Kalashev, and Dmitry V. Semikoz. GZK photons as ultra high energy cosmic rays. *J. Exp. Theor. Phys.*, 106:1061–1082, 2008.
- [88] John R. Ellis, V. E. Mayes, and Dimitri V. Nanopoulos. Uhecr particle spectra from crypton decays. *Phys. Rev. D*, 74:115003, 2006.
- [89] Biswajit Sarkar, Karl-Heinz Kampert, and Joerg Kulbartz. Ultra-High Energy Photon and Neutrino Fluxes in Realistic Astrophysical Scenarios. In *32nd International Cosmic Ray Conference*, volume 2, page 198, 2011.
- [90] R. U. Abbasi et al. Constraints on the diffuse photon flux with energies above 10^{18} eV using the surface detector of the Telescope Array experiment. *Astropart. Phys.*, 110:8–14, 2019.
- [91] W. D. Apel et al. KASCADE-Grande Limits on the Isotropic Diffuse Gamma-Ray Flux between 100 TeV and 1 EeV. *Astrophys. J.*, 848(1):1, 2017.
- [92] Yu. A. Fomin, N. N. Kalmykov, I. S. Karpikov, G. V. Kulikov, M. Yu Kuznetsov, G. I. Rubtsov, V. P. Sulakov, and S. V. Troitsky. Constraints on the flux of $\sim (10^{16} - 10^{17.5})$ eV cosmic photons from the EAS-MSU muon data. *Phys. Rev. D*, 95(12):123011, 2017.
- [93] J. A. Hinton and W. Hofmann. Teraelectronvolt astronomy. *Ann. Rev. Astron. Astrophys.*, 47:523–565, 2009.
- [94] A. Abramowski et al. Detection of very-high-energy gamma-ray emission from the vicinity of PSR B1706-44 and G343.1-2.3 with H.E.S.S. *Astron. Astrophys.*, 528:A143, 2011.
- [95] Alexander Aab et al. A targeted search for point sources of EeV photons with the Pierre Auger Observatory. *Astrophys. J. Lett.*, 837(2):L25, 2017.
- [96] A. Abramowski et al. Acceleration of petaelectronvolt protons in the Galactic Centre. *Nature*, 531:476, 2016.
- [97] Alexander Aab et al. A search for point sources of EeV photons. *Astrophys. J.*, 789(2):160, 2014.
- [98] Gunter Zech. Upper Limits in Experiments with Background Or Measurement Errors. *Nucl. Instrum. Meth. A*, 277:608, 1989.
- [99] Pedro Abreu et al. Follow-up Search for UHE Photons from Gravitational Wave Sources with the Pierre Auger Observatory. *PoS, ICRC2021:973*, 2021.
- [100] B. P. Abbott et al. GWTC-1: A Gravitational-Wave Transient Catalog of Compact Binary Mergers Observed by LIGO and Virgo during the First and Second Observing Runs. *Phys. Rev. X*, 9(3):031040, 2019.

BIBLIOGRAPHY

- [101] R. Abbott et al. GWTC-2: Compact Binary Coalescences Observed by LIGO and Virgo During the First Half of the Third Observing Run. *Phys. Rev. X*, 11:021053, 2021.
- [102] R. Abbott et al. GW190814: Gravitational Waves from the Coalescence of a 23 Solar Mass Black Hole with a 2.6 Solar Mass Compact Object. *Astrophys. J. Lett.*, 896(2):L44, 2020.
- [103] Enrique Zas. Neutrino detection with inclined air showers. *New J. Phys.*, 7:130, 2005.
- [104] Alexander Aab et al. Improved limit to the diffuse flux of ultrahigh energy neutrinos from the Pierre Auger Observatory. *Phys. Rev. D*, 91(9):092008, 2015.
- [105] Carla Bleve. Updates on the neutrino and photon limits from the Pierre Auger Observatory. *PoS, ICRC2015:1103*, 2016.
- [106] Alexander Aab et al. Probing the origin of ultra-high-energy cosmic rays with neutrinos in the EeV energy range using the Pierre Auger Observatory. *JCAP*, 10:022, 2019.
- [107] R. A. FISHER. The use of multiple measurements in taxonomic problems. *Annals of Eugenics*, 7(2):179–188, 1936.
- [108] P. Abreu et al. A Search for Ultra-High Energy Neutrinos in Highly Inclined Events at the Pierre Auger Observatory. *Phys. Rev. D*, 84:122005, 2011. [Erratum: *Phys.Rev.D* 84, 029902 (2011)].
- [109] M. G. Aartsen et al. Differential limit on the extremely-high-energy cosmic neutrino flux in the presence of astrophysical background from nine years of IceCube data. *Phys. Rev. D*, 98(6):062003, 2018.
- [110] P. W. Gorham et al. Constraints on the diffuse high-energy neutrino flux from the third flight of ANITA. *Phys. Rev. D*, 98(2):022001, 2018.
- [111] K Kotera, D Allard, and A.V Olinto. Cosmogenic neutrinos: parameter space and detectability from peV to zeV. *Journal of Cosmology and Astroparticle Physics*, 2010(10):013–013, Oct 2010.
- [112] M. Ahlers, L. A. Anchordoqui, M. C. Gonzalez-Garcia, F. Halzen, and S. Sarkar. GZK Neutrinos after the Fermi-LAT Diffuse Photon Flux Measurement. *Astropart. Phys.*, 34:106–115, 2010.
- [113] Karl-Heinz Kampert and Michael Unger. Measurements of the cosmic ray composition with air shower experiments. *Astroparticle Physics*, 35(10):660–678, May 2012.

-
- [114] R. Aloisio, D. Boncioli, A di Matteo, A. F. Grillo, S. Petrera, and F. Salamida. Cosmogenic neutrinos and ultra-high energy cosmic ray models. *JCAP*, 10:006, 2015.
- [115] Eli Waxman and John N. Bahcall. High-energy neutrinos from astrophysical sources: An Upper bound. *Phys. Rev. D*, 59:023002, 1999.
- [116] P. Abreu et al. Search for point-like sources of ultra-high energy neutrinos at the Pierre Auger Observatory and improved limit on the diffuse flux of tau neutrinos. *Astrophys. J. Lett.*, 755:L4, 2012.
- [117] Alexander Aab et al. Observation of a Large-scale Anisotropy in the Arrival Directions of Cosmic Rays above 8×10^{18} eV. *Science*, 357(6537):1266–1270, 2017.
- [118] V. A. Acciari et al. Teraelectronvolt emission from the γ -ray burst GRB 190114C. *Nature*, 575(7783):455–458, 2019.
- [119] Alexander Aab et al. Limits on point-like sources of ultra-high-energy neutrinos with the Pierre Auger Observatory. *JCAP*, 11:004, 2019.
- [120] M. G. Aartsen et al. All-sky Search for Time-integrated Neutrino Emission from Astrophysical Sources with 7 yr of IceCube Data. *Astrophys. J.*, 835(2):151, 2017.
- [121] A. Albert et al. First all-flavor neutrino pointlike source search with the ANTARES neutrino telescope. *Phys. Rev. D*, 96(8):082001, 2017.
- [122] Michael Schimp. Multi-messenger Astrophysics with the Pierre Auger Observatory. In *10th International Workshop on Very High Energy Particle Astronomy: New prospects for PeV and EeV astroparticle physics in the multiple messenger era*, 1 2021.
- [123] Alexander Aab et al. Ultrahigh-Energy Neutrino Follow-Up of Gravitational Wave Events GW150914 and GW151226 with the Pierre Auger Observatory. *Phys. Rev. D*, 94(12):122007, 2016.
- [124] Bruny Baret et al. Bounding the Time Delay between High-energy Neutrinos and Gravitational-wave Transients from Gamma-ray Bursts. *Astropart. Phys.*, 35:1–7, 2011.
- [125] Peter Meszaros. Gamma-Ray Bursts. *Rept. Prog. Phys.*, 69:2259–2322, 2006.
- [126] Shigeo S. Kimura, Kohta Murase, Peter Mészáros, and Kenta Kiuchi. High-Energy Neutrino Emission from Short Gamma-Ray Bursts: Prospects for Coincident Detection with Gravitational Waves. *Astrophys. J. Lett.*, 848(1):L4, 2017.

BIBLIOGRAPHY

- [127] Ke Fang and Brian D. Metzger. High-Energy Neutrinos from Millisecond Magnetars formed from the Merger of Binary Neutron Stars. *Astrophys. J.*, 849(2):153, 2017.
- [128] Alexander Aab et al. A Targeted Search for Point Sources of EeV Neutrons. *Astrophys. J. Lett.*, 789:L34, 2014.
- [129] P. Abreu et al. A Search for Point Sources of EeV Neutrons. *Astrophys. J.*, 760:148, 2012.
- [130] Francisco Salesa Greus. Searches for galactic neutron sources with the Pierre Auger Observatory. In *33rd International Cosmic Ray Conference*, page 1125, 2013.
- [131] P. W. Gorham et al. The Antarctic Impulsive Transient Antenna Ultra-high Energy Neutrino Detector Design, Performance, and Sensitivity for 2006-2007 Balloon Flight. *Astropart. Phys.*, 32:10–41, 2009.
- [132] Derek B. Fox, Steinn Sigurdsson, Sarah Shandera, Peter Mészáros, Kohta Murase, Miguel Mostafá, and Stephane Coutu. The ANITA Anomalous Events as Signatures of a Beyond Standard Model Particle, and Supporting Observations from IceCube. 9 2018.
- [133] Jiwoo Nam. Overview of the Fourth Flight of the ANITA Experiment. *PoS, ICRC2017:952*, 2018.
- [134] S. Hoover et al. Observation of Ultra-high-energy Cosmic Rays with the ANITA Balloon-borne Radio Interferometer. *Phys. Rev. Lett.*, 105:151101, 2010.
- [135] Konstantin Belov. Towards Determining the energy of the UHECRs observed by the ANITA detector. *AIP Conf. Proc.*, 1535(1):209, 2013.
- [136] H. Schoorlemmer et al. Energy and Flux Measurements of Ultra-High Energy Cosmic Rays Observed During the First ANITA Flight. *Astropart. Phys.*, 77:32–43, 2016.
- [137] James M. Cline, Christian Gross, and Wei Xue. Can the ANITA anomalous events be due to new physics? *Phys. Rev. D*, 100(1):015031, 2019.
- [138] M. G. Aartsen et al. A search for IceCube events in the direction of ANITA neutrino candidates. 1 2020.
- [139] A. Romero-Wolf et al. Comprehensive analysis of anomalous ANITA events disfavors a diffuse tau-neutrino flux origin. *Phys. Rev. D*, 99(6):063011, 2019.
- [140] Pedro Abreu et al. Search for upward-going showers with the Fluorescence Detector of the Pierre Auger Observatory. *PoS, ICRC2021:1140*, 2021.

- [141] E.J. Gumbel. *Statistics of Extremes*. Dover books on mathematics. Dover Publications, 2004.
- [142] Manlio De Domenico, Mariangela Settimo, Simone Riggi, and Eric Bertin. Reinterpreting the development of extensive air showers initiated by nuclei and photons. *JCAP*, 07:050, 2013.
- [143] Eric Bertin and Peter C. W. Holdsworth. Dissipation-induced non-Gaussian energy fluctuations. *EPL (Europhysics Letters)*, 102(5):50004, June 2013.
- [144] Eric Bertin. Global fluctuations and gumbel statistics. *Phys. Rev. Lett.*, 95:170601, Oct 2005.
- [145] Sergey Ostapchenko. Monte Carlo treatment of hadronic interactions in enhanced Pomeron scheme: I. QGSJET-II model. *Phys. Rev. D*, 83:014018, 2011.
- [146] Felix Riehn, Hans P. Dembinski, Ralph Engel, Anatoli Fedynitch, Thomas K. Gaisser, and Todor Stanev. The hadronic interaction model SIBYLL 2.3c and Feynman scaling. *PoS, ICRC2017*:301, 2018.
- [147] Eun-Joo Ahn, Ralph Engel, Thomas K. Gaisser, Paolo Lipari, and Todor Stanev. Cosmic ray interaction event generator SIBYLL 2.1. *Phys. Rev. D*, 80:094003, 2009.
- [148] T. Pierog, Iu. Karpenko, J. M. Katzy, E. Yatsenko, and K. Werner. EPOS LHC: Test of collective hadronization with data measured at the CERN Large Hadron Collider. *Phys. Rev. C*, 92(3):034906, 2015.
- [149] S. Petrera and F. Salamida. Update of the X_{\max} parameterizations for post-LHC hadronic models. GAP-2018-21.
- [150] D. Boncioli, A. Condorelli, M. Mastrodicasa, S. Petrera, F. Salamida, and C. Triarelli. A tool for fitting mass group fractions from X_{\max} distributions. GAP-2020-25.
- [151] S. Petrera. Towards a full simulation of the FD aperture. GAP-2004-15.
- [152] P. Abreu et al. The Exposure of the Hybrid Detector of the Pierre Auger Observatory. *Astropart. Phys.*, 34:368–381, 2011.
- [153] Till Bergmann, R. Engel, D. Heck, N. N. Kalmykov, Sergey Ostapchenko, T. Pierog, T. Thouw, and K. Werner. One-dimensional Hybrid Approach to Extensive Air Shower Simulation. *Astropart. Phys.*, 26:420–432, 2007.
- [154] S. Argiro, S. L. C. Barroso, J. Gonzalez, L. Nellen, Thomas Cantzon Paul, T. A. Porter, L. Prado, Jr., M. Roth, R. Ulrich, and D. Veberic. The Offline Software Framework of the Pierre Auger Observatory. *Nucl. Instrum. Meth. A*, 580:1485–1496, 2007.

BIBLIOGRAPHY

- [155] S. A. Bass et al. Microscopic models for ultrarelativistic heavy ion collisions. *Prog. Part. Nucl. Phys.*, 41:255–369, 1998.
- [156] Vladimir Novotny. Measurement of the spectrum of cosmic rays above $10^{16.5}$ eV with Cherenkov-dominated events at the Pierre Auger Observatory. *PoS, ICRC2019:374*, 2021.
- [157] Wolfgang A. Rolke, Angel M. Lopez, and Jan Conrad. Limits and confidence intervals in the presence of nuisance parameters. *Nucl. Instrum. Meth. A*, 551:493–503, 2005.
- [158] Ioana Alexandra Caracas et al. A tau scenario application to a search for upward-going showers with the Fluorescence Detector of the Pierre Auger Observatory. *PoS, ICRC2021:1145*, 2021.
- [159] G. Cataldi, M.R. Coluccia, A. Corvaglia, P. Creti, I. De Mitri, U. Giaccari, G. Marsella, D. Martello, M. Panareo, L. Perrone, C. Pinto, and M. Settimo. The PMT Test Facility in Lecce: Measurement Results of the First Phase Program. GAP-2011-109.
- [160] G. Cataldi and M.R. Coluccia. PMT R6095 Test Results. GAP-2015-004.
- [161] L. Calcagni, C. A. García Canal, S. J. Sciutto, and T. Tarutina. LHC updated hadronic interaction packages analyzed up to cosmic-ray energies. *Phys. Rev. D*, 98(8):083003, 2018.
- [162] Á. Pastor-Gutiérrez, H. Schoorlemmer, R. D. Parsons, and M. Schmelling. Sub-TeV hadronic interaction model differences and their impact on air showers. *Eur. Phys. J. C*, 81(4):369, 2021.
- [163] H. Fesefeldt. The Simulation of Hadronic Showers: Physics and Applications. 12 1985.
- [164] A. Fasso, A. Ferrari, P. R. Sala, and J. Ranft. FLUKA: Status and prospects for hadronic applications. In *International Conference on Advanced Monte Carlo for Radiation Physics, Particle Transport Simulation and Applications (MC 2000)*, pages 955–960, 10 2000.
- [165] V. N. Gribov. A REGGEON DIAGRAM TECHNIQUE. *Zh. Eksp. Teor. Fiz.*, 53:654–672, 1967.
- [166] S. Ostapchenko. Models for cosmic ray interactions. *Czech. J. Phys.*, 56:A149–A159, 2006.
- [167] T. K. Gaisser and F. Halzen. "Soft" Hard Scattering in the Teraelectronvolt Range. *Phys. Rev. Lett.*, 54:1754–1756, Apr 1985.
- [168] G. Pancheri and Y. Srivastava. Jets in minimum bias physics. *Phys. Lett. B*, 159(1):69–75, 1985.

- [169] G. Pancheri and Y.N. Srivastava. Low-pt jets and the rise with energy of the inelastic cross section. *Phys. Lett. B*, 182(2):199–207, 1986.
- [170] Loyal Durand and Pi Hong. QCD and Rising Total Cross-Sections. *Phys. Rev. Lett.*, 58:303–306, 1987.
- [171] M. M. Block and R. N. Cahn. High-Energy $p\bar{p}$ and pp Forward Elastic Scattering and Total Cross-Sections. *Rev. Mod. Phys.*, 57:563, 1985.
- [172] Martin M. Block. Hadronic forward scattering: Predictions for the Large Hadron Collider and cosmic rays. *Phys. Rept.*, 436:71–215, 2006.
- [173] Hans-Uno Bengtsson and Torbjorn Sjostrand. The Lund Monte Carlo for Hadronic Processes: Pythia Version 4.8. *Comput. Phys. Commun.*, 46:43, 1987.
- [174] Torbjorn Sjostrand. Status of Fragmentation Models. *Int. J. Mod. Phys. A*, 3:751, 1988.
- [175] T. Pierog, Iu. Karpenko, S. Porteboeuf, and K. Werner. New Developments of EPOS 2. 11 2010.
- [176] R. J. Glauber and G. Matthiae. High-energy scattering of protons by nuclei. *Nucl. Phys. B*, 21:135–157, 1970.
- [177] Arunava Bhadra, Sanjay K. Ghosh, Partha S. Joarder, Arindam Mukherjee, and Sibaji Raha. Study of low energy hadronic interaction models based on BESS observed cosmic ray proton and antiproton spectra at medium high altitude. *Phys. Rev. D*, 79:114027, 2009.
- [178] A. Capella, U. Sukhatme, C-I Tan, and J. Tran Thanh Van. Dual parton model. *Phys. Rept.*, 236:225–329, 1994.
- [179] Alfredo Ferrari, G Battistoni, Francesco Cerutti, R Engel, A Fassò, E Gadioli, M V Garzelli, J Ranft, S Roesler, and P R Sala. Recent Developments in the FLUKA nuclear reaction models. *Ric. Sci. Educ. Perm., Suppl.*, 126:483–495, 2006.
- [180] G. Baur, G. Graf, H. Petersen, and M. Bleicher. Multi-particle interactions within the UrQMD approach. *EPJ Web Conf.*, 13:06002, 2011.
- [181] G. A. Anastasi. Reconstruction of events from the surface detector of the Pierre Auger Observatory using air shower Universality. GAP-2019-035. PhD thesis. 2019.

BIBLIOGRAPHY

Acknowledgements/ Ringraziamenti

Here we are. More than three years have passed since I started my PhD, and now it's time to take stock of these years. Too many feelings intertwines in my heart and push to find some space between the keys of this keyboard. Disentangling them is anything but easy, and the more I try in a language other than that of my own soul, the harder it becomes. This is the reason why in this section I will ask my beloved mother tongue to help me thank all the people that shared these years with me, switching to English when needed to thank all those with whom a different native language did not prevent to find deeper connections.

Il mio primo grazie è rivolto al mio relatore, Francesco Salamida, per la sua costante disponibilità e il suo instancabile incoraggiamento. Grazie per avermi accompagnato in questi anni, per aver messo la sua esperienza e la sua competenza a mia disposizione, per avermi fatto trovare un ambiente colloquiale e privo di barriere che ho sempre apprezzato e mai dato per scontato.

Un grazie al gruppo di Auger dell'Università dell'Aquila. Grazie a Denise Boncioli per i proficui scambi di idee e suggerimenti, e a Vincenzo Rizi per avermi fatto trovare un pezzo del mio paese natò fuori da esso.

Un grande grazie ai membri del gruppo di Lecce del task Multi-Messenger di Auger, Lorenzo Perrone ed Emanuele De Vito. Grazie per il continuo confronto e le stimolanti osservazioni. Lavorare con loro è stato per me motivo di grande crescita personale.

Grazie a tutti i dottorandi di Auger che hanno incrociato il loro cammino con il mio. Grazie ad Antonio Condorelli, per il lavoro svolto insieme nella prima parte di questo percorso e per essere stato mio compagno di viaggio in Argentina. Non ho dimenticato affatto che gli devo ancora una cena. Grazie a Giocchino Alex Anastasi, per avermi fornito l'occasione di muovere i primi passi all'interno della Collaborazione con la sovrapposizione tra la fine del suo percorso di dottorato e l'inizio del mio. Grazie a Pierpaolo Savina, per essere stato mio mentore sull'Offline e, soprattutto, per avermi accompagnato fino alla fine del mondo. Aspetto ancora la sua epica entrata in scena sulle note dei Metallica. Una menzione a parte va a Caterina Trimarelli, amica prima che collega, per aver quotidianamente diviso nello stesso ufficio gioie e momenti di sconforto. Grazie per il suo costante supporto e sopportazione, anche durante i tempi bui di reclusione domestica a cui questo infelice tempo ci ha costretti. Sarebbero mille

ACKNOWLEDGEMENTS/RINGRAZIAMENTI

altre le cose da dire, ma mi sono ripromesso di non essere troppo retorico. Grazie grazie grazie.

Un grazie alle mie due migliori amiche, Ambretta e Vale. Grazie per essere state la mia famiglia aquilana. Grazie per le cene nell'atmosfera perennemente natalizia della loro casa. Grazie per la loro pazienza, per avermi capito ed essersi adattate al mio modo di essere. Grazie per avermi fatto scoprire che nella mia vita precedente sono stato un alpaca, e per la passione condivisa per questo mitologico essere. Non riesco ad immaginare come sarebbero potuti trascorrere questi anni senza di loro. Grazie ad Ambretta, per l'amicizia longeva e controcorrente, sempre fortificata dallo scorrere del tempo. Grazie per le consulenze, i consigli, gli strattoni atti a riportarmi sulla retta via. Grazie per le serate infinite, le chiacchierate estive, i gin lemon senza cannuccia. Grazie per esserci stata in ogni occasione. Le prometto solennemente che non dimenticherò mai più di andare a ritirare gli arrostitini. Grazie a Vale, per essere amica e consigliera. Grazie per il suo senso pratico e la sua visione lucida, in grado di portare luce quando le incertezze offuscano la strada da intraprendere. Grazie per aver sempre trovato il tempo di prestarmi orecchio quando ne avevo bisogno. Grazie per la sua innata capacità di attrarre il surreale, per le risate a crepelle, per le teste di bue. Grazie per avermi fatto trovare chi cercava (ritengo che quella serata sia stata un passo fondamentale per la conclusione di questo percorso). Grazie anche ad Albano il tulipano, che considero parte di questa famiglia. Voglio che sappia che il suo sacrificio non è stato vano.

Grazie a Matteo, per la vicinanza oltre la distanza. Grazie per aver sempre creduto in me, a volte più di quanto non abbia fatto io stesso. Grazie per le passioni in comune, le lunghe chiacchierate al telefono, le battute sempre pronte. Grazie per aver fatto in modo che il suo percorso procedesse parallelamente al mio. Sono certo che arriverà presto il momento in cui nel buio un riverbero viola accompagnerà il suono di una spada laser.

Grazie a Paolo, per la sua amicizia in grado di trascendere tempo e spazio. Grazie per tutte le avventure e i momenti vissuti insieme dai tempi delle scuole superiori. Per quanto tempo possa passare tra un nostro incontro e l'altro, ogni volta ritrovo la sensazione di non esserci visti dal giorno prima. Vorrei ricordargli che il Messico ci sta aspettando.

Grazie a Giuseppe, per aver continuato ad essere il mio compagno di banco anche fuori dalle mura scolastiche. Grazie per tutti i film visti insieme al cinema. Grazie per le chiacchierate infinite sempre oscillanti tra massimi sistemi e facezie. Ora che ci penso, è da un po' che non controllo la situazione asteroidi.

Grazie a Giacomino, per avermi sempre spronato a migliorare. Grazie per i pomeriggi di studio passati insieme e per aver fatto in modo che gli anni universitari passassero con più leggerezza. Non esagero nel dire che il raggiungimento di questo traguardo è in parte anche merito suo.

Un grazie a tutti i frequentatori abituali e non della stanza dottorandi. Grazie a Valerio, Riccardo e Benedetta per la quotidiana compagnia durante i primi anni di questa avventura, per le serate ad All Beers, per le escursioni. Grazie ai superstiti, Daniele, Giusy, Ilaria e, di nuovo, Caterina, per aver donato colore all'incerto grigiore

ACKNOWLEDGEMENTS/RINGRAZIAMENTI

del periodo conclusivo di questo cammino. Grazie per le pause caffè, i momenti di svago, il sostegno.

Thanks to Odysse for his friendship and all the moments shared in L'Aquila. Thanks for the soccer games and for the nights at the Irish pub. I will really miss them.

Thanks to Irakli for having uncovered the Georgian part of my soul. Thanks for the fun times, the paper ball games and the arm wrestling matches. I am looking forward to make another toast with him.

Infine, i ringraziamenti più difficili da esprimere, quelli su cui l'ineffabilità della parola incombe più minacciosa, perché rivolti a coloro che mi sono stati accanto in ogni momento della mia vita. Un grazie enorme alla mia famiglia, senza di cui non sarei qui a scrivere queste righe. Grazie ai miei genitori, per aver sempre sostenuto le mie scelte e non aver mancato mai di supportarmi. Grazie per tutta la dedizione e il sacrificio con cui hanno sempre creato le condizioni affinché mi sentissi libero di poter prendere le mie decisioni. Ad oggi non saprei dare una definizione migliore di amore. Grazie a mia sorella, per ricordarmi costantemente che per quanto forte possa essere la corrente dello sconforto che si oppone al nostro remare, c'è sempre qualcosa che è possibile fare. Grazie per continuare a trovare il tempo di condividere esperienze e di farmi sentire che su di lei potrò sempre contare. Grazie a nonno Sante, e a tutti i miei altri nonni il cui nome è scolpito indelebilmente sul mio cuore, per avermi trasmesso valori di altri tempi. Dio solo sa quanto questo mondo ne abbia bisogno.

Un grazie anche a L'Aquila, città che in questi anni ho imparato ad amare. Grazie per i tramonti sul Gran Sasso, per le boccate d'aria a pieni polmoni, per aver mitigato le mie affezioni. Grazie per essere stata la cornice perfetta di questi anni stupendi.

ACKNOWLEDGEMENTS/RINGRAZIAMENTI
